Modélisation numérique des transistors à effet de champ organiques basé sur la densité d'états Gaussienne

Yongjeong Lee

INSTITUT POLYTECHNIQUE DE PARIS

NNT : 2020IPPAX043

Thèse de doctorat

Gaussian density-of-states driven numerical modeling of organic field-effect transistors

Thèse de doctorat de l'Institut Polytechnique de Paris
préparée à École polytechniuque

École doctorale n°626 Ecole Doctorale de l'Institut Polytechnique de Paris (ED IP Paris)
Spécialité de doctorat: Physique

Thèse présentée et soutenue à Palaiseau, le 16 octobre 2020, par

Yongjeong Lee

Composition du Jury :

Paul Heremans Professeur/Fellow, Katholieke Universiteit Leuven/IMEC	Rapporteur
Olivier Simonetti Maitre de Conférences, Université de Reims Champagne-Ardenne	Rapporteur
Benjamin Iñiguez Professeur, Universitat Rovira i Virgili	Examinateur
Alistair Rowe Chargé de Recherche, École polytechniuque/CNRS (UMR 7643)	Président
Ahmed Nejim R&D Projects Manager, Silvaco Europe Ltd.	Invité
Gilles Horowitz Professeur/Directeur de Recherche Émérite, École polytechniuque/CNRS (UMR 7647)	Invité
Sungyeop Jung Assistant research professor, POSTECH	Co-Directeur de thèse
Yvan Bonnassieux Professeur, École polytechniuque	Directeur de thèse

GAUSSIAN DENSITY-OF-STATES DRIVEN NUMERICAL MODELING OF ORGANIC FIELD-EFFECT TRANSISTORS

Yongjeong Lee
Yongjeong.lee@polytechnique.edu

Thesis Director :
Professeur Yvan Bonnassieux

A thesis for the degree of
Ph.D. in Physics

2020

Abstract

Although the device physics of organic field-effect transistors (OFETs) has been widely studied, the analysis with energetic distribution of the density-of-states (DOS) is still lacking in spite of the disordered nature of organic semiconductors. Because charge transport and injection take place at the Gaussian DOS, this distinctive energetic structure of organic semiconductors could make the charge-accumulation process, and hence the device operation, different. This thesis is dedicated to understanding the effect of Gaussian DOS on device parameters of OFETs, the threshold voltage, charge-carrier mobility and injection barrier via numerical finite-element based 2D simulations and experimental validation. The threshold voltage is comprehended by the charge trapping into the secondary Gaussian trap DOS as well as the intrinsic Gaussian DOS. We show that the overlap of two Gaussian DOSs due to the disorder induces specific threshold behaviors of OFETs. Second, the hopping transport is studied via Gaussian disordered model (GDM) on random spatial sites of organic semiconductors. This model can offer a precise result over GDM with cubic lattice. Also, we propose a correct parametrization of the model for wide range of materials from polymers to small molecules. Lastly, charge-based and transport-based injection barrier are studied and compared with Gaussian DOS. The advantages and limits of each model are evaluated.

Keywords : Organic electronics, Organic field-effect transistors, Device physics, Numerical modeling, Gaussian density-of-states

Acknowledgements

First, I would like to appreciate my advisor Prof. Yvan Bonnassieux, the director of LPICM, for his kind direction of scientific works and entire life in France from the beginning. Thanks to him, my life in France began through EP-KHU dual master program. Me and Korean colleagues remember you forever as a good instructor. I am also grateful to Dr. Sungyeop Jung who led me for 5 years research in the LPICM. His insight and philosophy on scientific works have always been motivating me. I would also like to thank Prof. Gilles Horowitz for guidance and his scientific enthusiasm that taught me a lot on organic electronics. I would like to mention LPICM members, Pere Roca I Cabarrocas, Denis Tondelier, Bernard Geffroy, Jean-Charles Vanel, Abderrahim Yassar, Frederic Liege, Eric Paillassa, Laurence Gerot, Gabriela Medina, Fabienne Pandolf, Haeyeon Jun, Minjin Kim, Robert Benda, Gookbin Cho, Junha Park, Tanguy Levent, Anna Shirinskaya, Lin Qiqiao, Hindia Nahdi, Junbum Park and Heeryung Lee. It was a great pleasure to discuss and work with them. I thank again all LPICM members who supported me for administrative, technical and personal works. I wish to extend my gratitude to my previous Korean colleagues in LPICM, Jeongmo Kim, Mintae Chung, Hyeonseok Sim, Heetae Park, Wonjong Kim, Dongcheon Kim, Jejune Park and Jiho Yoon.

I am appreciating Prof. Sergei Baranovskii for the fruitful discussion on charge transport model that helped me to broad my knowledge and get a final goal of my thesis. I am also thankful Prof. Louis Giraudet, Prof. Olivier Simonetti and Dr. Phillippe Lang who invited me for experimental work and supported my research. I would like to thank Dr. Ahmed Nejim, Dr. Andrew Plews, who invited me to conduct research visit that developed my research work significantly and broadened my experience.

I also acknowledge the Ph.D. fellowship from Ecole doctoral IP Paris, the mobility grants from Horizon 2020 Marie Skłodowska-Curie Fellowship DOMINO RISE Programme and Horizon 2020 research and innovation programme, CORNET project.

I appreciate the community of Association des Scientifiques Coréens en France (ASCoF) that broadened my academic and personal experience.

Lastly, I would like to express my deepest love to my family for all their support.

Contents

1. Introduction **4**

1.1 Organic electronics 4

1.2 Motivation....6

1.3 Thesis overview 8

2. Fundamentals **10**

2.1 Organic semiconductors 10

2.1.1 π-conjugation in organic material....10

2.1.2 Representative polymers for OFET application 12

2.1.3 Representative small molecules for OFET application 13

2.2 Density of states....15

2.2.1 Square-root density of states 15

2.2.2. Exponential density of states 17

2.2.3 Gaussian density of states 18

2.3 Threshold voltage 20

2.3.1 Extraction methods 21

2.3.2. Physical origin of the threshold voltage in various transistors 23

2.4 Charge transport in organic disordered semiconductors 25

2.4.1 Gaussian disorder model....25

2.4.2 Extended Gaussian disorder model in cubic lattice 27

2.4.3 Gaussian disorder model in spatial disorder....28

2.5 Charge carrier injection 30

2.5.1 Injection barrier 30
2.5.2 Non-ideal factors 30

3. Methods **33**
3.1 Numerical simulation 33
3.2 Energetic structure 34

4. Threshold voltage modeling **36**
4.1 Effect of single Gaussian density of states 37
4.1.1 Validation of the ratio method 37
4.1.2 Physical origin of threshold voltage 39
4.1.3 Effect of Gaussian width 42
4.1.4 Fixes charges 43
4.2 Effect of double Gaussian density of states 45
4.2.1 Charge trapping and threshold voltage 45
4.2.2 Effects on the power-law mobility 49
4.2.3 Experimental validation 52

5. Mobility modeling **58**
5.1 Gaussian disorder models 59
5.1.1 Limits of initial parametrization 59
5.1.2 Parametrization method of EGDM 62
5.1.3 Parametrization method of GDM by Baranovskii 65
5.1.4 Advantages of the GDM on spatially random sites 67
5.2 Parametrization 69
5.2.1 Localization length 69
5.2.2. Attempt-to-escape frequency 74
5.3 Experimental validation 76
5.3.1 Experimental data of OFETs 77

5.3.2. Numerical simulation of OFETs 77

6. Injection barrier modeling **81**

6.1 Charge-based injection barrier model 82

6.1.1 Effective injection barrier 82

6.1.2 Numerical validation by contact resistance 82

6.1.3 Degenerate and non-degenerate condition. 86

6.2 Transport-based injection barrier model 89

6.2.1 Mobility edge and transport energy 89

6.2.2 Dependency on the localization length 90

6.2.3 Dependency on the Gaussian width 90

6.3 Experimental extraction 92

6.3.1 Ultraviolet photoelectron spectroscopy spectra 92

6.3.2 Extraction of injection barriers 95

7. Conclusion and outlook **98**

A Publications **101**

B Activities **103**

C Experimental details **104**

Bibliography **106**

Chapter 1

Introduction

1.1 Organic electronics

Organic electronics is new field of electronics based on organic semiconductors such as conjugated polymers [1]–[8] and small molecules [9]–[17], that consist of carbon-hydrogen bonds with many compounds, e.g. oxygen, nitrogen and sulfur. This technology has high potential for future electronic applications because of many distinctive characteristics. Compared to covalent bonds in inorganic semiconductor, weak van der Waals interaction between organic molecules induce high mechanical flexibility. In addition, some materials are soluble or easily reformed in the organic solvents that can help to deposit thin film layer more simply by spin-coating process or ink-jet printing process. Such processes for organic semiconductors are very effective to put materials at desired positions and large-area with low-cost. As a growing interest of bio-electronic interface, bio-compatibility of some organic semiconductor gains attention for bioelectronic devices and systems. Therefore, organic electronics enable to realize a low-cost, flexible and bio-compatible technology in future electronics.

From the initial discovery of conducting polymer, halogen-doped Polyacetylene in 1977 [18], the technology with these materials has been rapidly grown in three major applications, photovoltaic, light-emitting diode and transistors. As milestone works in 1986, two-layer organic photovoltaic (OPV) with copper phthalocyanine (CuPc) and perylene tetracarboxylic derivative [19] and the first organic field-effect transistor (OFET) with polythiophene [20] were introduced. In the following year, Tang developed the organic light-emitting diode (OLED) with Tris(8-hydroxyquinolinato)-aluminum (Alq3) and diamine junction. [21] Today, these devices have been significantly developed. Especially,

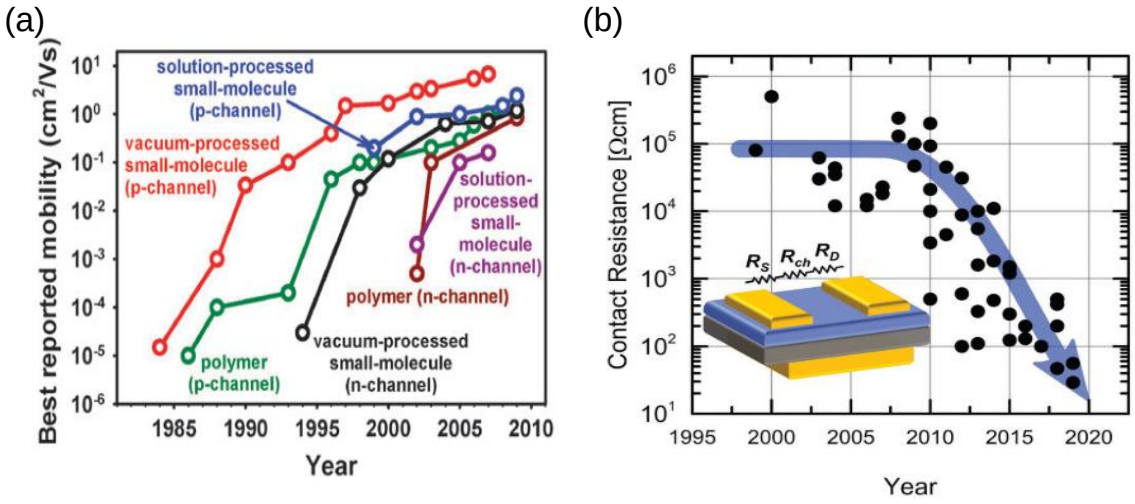

Fig. 1.1. Development of (a) best reported mobility for various type of OFETs from [23] and (b) contact resistance [24] during decades.

OLEDs is the most successful devices based on organic semiconductor that are commonly used in a wide range of displays, e.g. smartphones, televisions and smartwatch. Compared to conventional display technologies like liquid-crystal display (LCD) of plasma display, OLEDs possess many advantages such as low power operation, wide color gamut and fast response. Recently, many foldable or stretchable products based on OLEDs were introduced in display market that was impossible with LCD due to inflexible back-light unit and modules of displays. For OPVs, the maximum efficiency of OPV cells (various type) exhibit 17.4 % for tandem cell and 14.2 % for single cell according to the report of NREL in 2020 [22]. Many current products are available in the market that provide flexible (Minimum bending radius 2cm), lightweight (<1kg/m^2) and ultra thin (<1 mm) OPVs.

For OFETs, the performance of devices has been improved dramatically during decades [23], [24] (Fig. 1.1). In the early stage of OFETs in 1980s, they exhibited very low mobility in a range of ~10^{-5} cm^2/Vs due to the slow hopping conduction in disordered system. This mobility was 5 – 7 orders of magnitude lower than conventional electronic devices such as amorphous silicon and poly-silicon devices. However, in 2000s, maximum reported mobility increased rapidly, and they were comparable with conventional electronic devices thanks to the advanced material design and fabrication process. In addition, the high contact resistance of OFETs at the semiconductor/electrode contact was regarded a great

challenge for high performance devices. Compared to the Si transistors with heavily doped Ni silicide contact that exhibited contact resistance in a range of 10^{-4} Ω·cm, early OFETs reported 10^{6} to 10^{5} Ω·cm. This high contact resistance degraded not only field-effect mobility [25] but also the cutoff frequency [26] in OFETs. Recently, improved materials, device structure and fabrication technique can help to reduce contact resistance. The lowest reported contact resistance of OFET until now is 29 Ω·cm by Borchert and coworkers [27].

Thanks to the highly improved performance, many applications can be feasible with OFETs. Organic integrated circuits based on organic complementary circuits were realized by many groups [28]–[31]. OFETs are adopted in radio frequency identification (RFID) tags [32] that are promising in terms of low-cost fabrication by printing technologies and/or roll-to-roll method. Display back planes in LCDs or OLEDs also developed based on OFETs. Especially, Plastic Logic commercialized ultra-flexible paper-like displays in a wide range of the size (1 inch to 15 inch) [33]. Also, wearable electronics are promising market for OFETs. Large area flexible pressure sensors and temperature sensors widely accepted OFETs [34]–[36]. These large area flexible sensors will be applicable for security systems, regenerative medicine and various purposes related with artificial skins of robots. Application of organic transistors for neuromorphic computing [37], brain interface [38] and bio-inspired electronics [39] have been widely studied nowadays.

1.2 Motivation

The motivation of this thesis is lack of physical understanding of OFETs' device physics based on Gaussian density of states (DOS). Although considerable improvement of performance enables to realize various aforementioned applications with OFETs, current comprehension on fundamental behavior of OFETs is incomplete. In fact, the main research of OFETs has been focused on developing material designs, fabrication process and experimental performances to compete with matured inorganic electronics. Therefore, many theoretical concepts remain vague. Particularly, the effect of Gaussian DOS that represents disordered nature of organic semiconductors on device physics has been commonly overlooked. In organic semiconductors, the weak van der Waals intermolecular bonding induces Gaussian DOS instead of square-root DOS and

exponential DOS because randomly distributed energetic states originate from amorphous phase of molecules. Therefore, Gaussian DOS should be a basis of every electrical behavior.

There are two main reasons that Gaussian DOS has been passed over for device physics during decades. First, ones believed the effect of Gaussian DOS on device physics is trivial except for the charge transport. The hopping transport in localized states studied widely by Gaussian disorder model (GDM) from 1980s, whereas studies on threshold voltage and charge injection based on Gaussian DOS are few compared to that on charge transport. In fact, Gaussian DOS is critical for the charge injection as well as the charge transport. A conventional band edge concept, so-called the onset of highest occupied molecular orbitals (HOMO) and lowest unoccupied molecular orbitals (LUMO), was demonstrated that it is not proper to define band edge in Gaussian DOS because charge carriers behaves as a degenerate condition even very low charge concentration [40]. Also, Gaussian broadening can reduce injection barrier and enhance charge injection due to the deep tail states [41]. These results can give significant effect on electrical behaviors e.g. threshold voltage and contact resistance because OFETs operate in the accumulation regime. Second, Gaussian DOS is merely solved by analytical method. For example, the hole concentration at the contact can be calculated by integral of charge carrier statistics and DOS. In conventional inorganic semiconductors, analytical solution of charge density is easily obtained by the Boltzmann statistics. In contrast, the Boltzmann statistics cannot guarantee an exact analytical solution for Gaussian DOS due to the degenerate condition of charge carriers. Furthermore, Gauss-Fermi integral with Fermi-Dirac statistics does not have full analytical solution yet. This complexity during derivation of analytical models may hinder studies of device physics considering Gaussian DOS.

In this context, the necessity of physical modeling based on Gaussian DOS for OFETs is recognized in an efficient way. TCAD Numerical simulation based on finite-element method can be an alternative solution of analytical model because it can simply calculate all equations regardless of complexity. It is simple to implement physical theories into the calculation such as Gaussian DOS and GDM. Also, used parameters in the numerical simulation can give an insight of physical understanding underneath of models. Besides, it can be helpful to promote the commercialization of organic electronics via the electronic design

automation (EDA) technology by adopting commercial numerical software tools. As aforementioned applications require more complex structures than before, the importance of device modelling and circuit simulation increases because the optimization of complex devices and circuits can success by several iteration processes of modeling, design, fabrication and evaluation [42]. Therefore, it is necessary to study device-level modeling with Gaussian DOS within the iterative numerical solver.

1.3 Thesis overview

The title of thesis is 'Gaussian density of states driven numerical modeling of organic field-effect transistors'. Theoretical approach to understand electrical behavior of OFETs by Gaussian DOS is developing via TCAD numerical simulation. The principle goal is to comprehend device parameters of OFETs such as the threshold voltage, charge carrier mobility and injection barrier through Gaussian DOS and validate theoretical approach to the experimental approach. These three device parameters are in line with our motivations of the thesis. Here, a short description for each chapter is presented.

Chapter 1 Introduction describes a field of organic electronics with recent progress and motivation of the thesis with our final goal.

Chapter 2 Fundamentals summarizes principles of conducting organic semiconductors and OFET devices. The representative organic semiconductors for OEFTs are introduced both small molecules and polymers. The shape of density of states, i.e. square-root, exponential and Gaussian DOS, are categorized depending on materials. Also, the basic concept of the threshold voltage in transistors is delineated as well as various extraction methods. The Gaussian disorder model is explained for charge hopping transport. Two representative GDM, EGDM and GDM by Baranovskii are introduced and compared.

Chapter 3 Methods shows the calculation method of TCAD numerical simulation. Physical models to describe OFETs with organic disordered semiconductors (ODSs) are listed. Also, energetical structure of simulated OFET devices is described.

Chapter 4 Threshold voltage modeling is the first chapter for scientific result. The threshold behavior of OFETs is identified by the charge trapping into

the single and double Gaussian DOS systems. By systematic numerical simulation, the physical meaning of the threshold voltage is examined through a reliable extraction method for organic disordered semiconductor with and without trap states. The effect of simultaneous charge trapping into the overlapped DOS between Gaussian intrinsic and trap DOSs is highlighted to comprehend threshold behavior and concomitant power-law dependency of mobility. The experimental validation of proposed model is carried out by numerical fit to the ink-jet printed OFETs.

Chapter 5 Mobility modeling is the second chapter for scientific result. A correct parametrization of Gaussian disorder model on spatially random sites is studied to describe charge transport in disordered materials and following device characteristics. GDM on random sites is compared with the EGDM that assumed the cubic lattice sites to show the former enables an exact solution over the latter. Then, a new set of model parameters, i.e. the localization length and the attempt-to-escape frequency, is proposed to correctly account for higher mobility conditions for current high performance OFETs. To validate, various OFETs with donor-acceptor copolymer, semi-crystalline polymer and polycrystalline small molecule are examined at various temperature condition and each physical parameters are coupled with each material condition in thin-film. The model is implemented into a numerical simulation tool to compare with the measured device characteristics.

Chapter 6 Injection barrier modelling is the last chapter for scientific result. As the band tail of Gaussian DOS is unclear, we tried to elucidate a physically-based injection barrier. First, we examined validity of charge-based injection barrier, so-called ‘effective injection barrier’ via the contact resistance model of coplanar OFETs. Then, we proposed a new transport-based injection barrier with transport energy of Gaussian DOS. Finally, two injection barriers were extracted from experimental result of photoemission spectroscopy and compared with the conventional injection barrier concept of Gaussian DOS, the onset of HOMO.

Chapter 7 Conclusion and outlook summarize key results of the thesis with some remarks. Suggestions for perspectives work is proposed.

Chapter 2

Fundamentals

2.1 Organic semiconductors

2.1.1 π-conjugation in organic material

Organic semiconductor is the organic material that show semiconducting property. Organic small molecules and polymers are representative materials that consist of hydrogen and carbon. They can be crystalline or amorphous structure on thin films depending on materials. Normally, they are insulators, but convert to semiconductors when charge carriers are introduced by charge injection from electrode, doping and photo-excitation.

Semiconducting properties originated from a conjugated system in carbon atoms. Carbon has four outermost electrons, i.e. a group four element in the periodic table. Each electron occupies separately in 2s, $2p_x$, $2p_y$ and $2p_z$ atomic orbitals. They can be hybridized in various ways that leads to numerous bonding configurations, e.g. sp_1, sp_2 and sp_3 depending on the number of p atomic orbitals that participates in the hybridizations. When 3 p atomic orbitals get involved with four neighboring atoms, four sp_3 hybrid orbitals with equal energy are composed. When 2 p atomic orbitals get involved with three neighboring atoms, three sp_2 hybrid orbitals are created.

Remarkably, the sp_2 hybridization forms additional π bonding that make delocalization of electrons. In ethylene C_2H_4 (Fig. 2.1), each carbon atom has 3 sp_2 orbitals with two hydrogen atoms and one carbon atom. Strong σ bonding is formed by sp_2 orbitals between two carbon atoms and this bonding is difficult to be broken due to the large overlap of orbitals. Also, 3 sp_2 orbitals are in the planar plane to minimize the repulsion energy. For remaining p_z orbitals that are

perpendicular to the sp_2 plane form π bond by sharing their electrons. Although this π bonding energy is weaker than σ bonding due to the small overlapped orbitals, this weak bonding results in the semiconducting property of organic molecules. In organic semiconductors, the HOMO and the LUMO corresponds to the occupied π binding orbital and unoccupied π binding orbital, respectively. The energetic difference between occupied binding orbital and unoccupied binding orbital is small for π bonding due to the weak binding energy. Therefore, such organic materials that possess frontier orbital created π bonding lead to the semiconducting property. For σ bonding, the energetic difference between occupied binding orbital and unoccupied binding orbital is large due to the strong binding energy. For large molecules such as benzene C_6H_6 (Fig. 2.2), π bonding results in the delocalization of electrons. Six electrons in the benzene from the six p_z orbitals are weakly bounded to neighboring p_z orbitals. By increasing number of p_z orbitals that participate to the π bonding, the HOMO and LUMO split to close similarly to the inorganic semiconductors.

Thanks to the delocalization of the electrons via π bonding, charge carrier can move freely in a molecule. In such molecule, π bonding makes electrons move and σ bonding maintain a rigid structure of the molecule. This molecular system is a π-conjugated system.

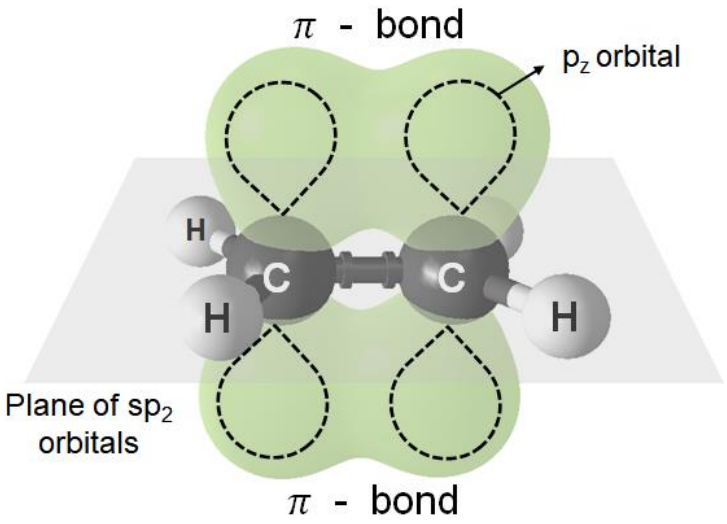

Fig. 2.1. Schematic of $\boldsymbol{\pi}$-conjugated system of ethylene C_2H_4.

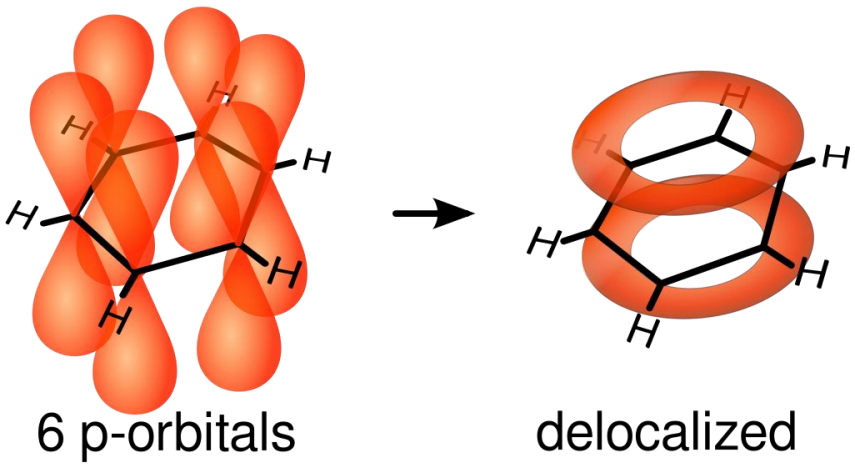

Fig. 2.1. Schematic of $\boldsymbol{\pi}$-conjugated system of benzene C_6H_6.

2.1.2 Representative polymers for OFET application

For OFET application, organic semiconductor materials can be divided by two categories, conjugated polymers and conjugated small molecules. The polythiophene has been regarded as a prototypical material for semiconducting polymer. Particularly, regioregular poly(3-hexylthiophene) (P3HT) that is alkyl-substituted polythiophene (Fig. 2-3a) is the most widely used material thanks to the good solubility [43] and high mobility. Although initial pristine polythiophene showed poor mobility, its self-organization into lamella crystalline structure of the regioregular P3HT increases mobility significantly. The coplanarity of the polymer backbone enhance the extent of intermolecular π conjugation. Compared to regiorandom P3HT (Fig. 2-3b), regioregular material show 3 orders of magnitude higher mobility [44].

Poly(2,5-bis(3-alkylthiophen-2-yl)thieno-[3,2-b]thiophene (pBTTT) [45] (Fig. 2-3c) is proposed by McCulloch and coworkers to improve the stability and performance of alkyl-substituted polythiophenes. Thieno[3,2-b]thiophene in the backbone can produce a ordered crystalline structure because of the rotational invariance. The liquid-crystalline phase can be crystallized by annealing and cooling process to increase the molecular ordering. The mobility in the pBTTT based transistor reached up to 1.1 cm^2/Vs [46].

More recently, alternating donor-acceptor copolymers show very high

mobility more than 1 cm^2/Vs [47], [48]. Especially, indaceno-dithiophene–benzothiadiazole (IDT-BT) [49] (Fig. 2-3d) studied widely because this material showed high mobility without long-range order. Recent study proved that charge transport occurs quasi one dimensionally along the backbone with occasional intermolecular hopping within face-on structure [50]. In addition, IDT-BT exhibit nearly disorder-free characteristics because of the planar and torsion-free backbone [1].

2.1.3 Representative small molecules for OFET application

Many small molecules are deposited by thermal evaporation because they are commonly insoluble in organic solvents. During thermal evaporation, these materials form polycrystalline structure by self-organization. Pentacene (Fig. 2-3e) is the most widely used small molecule for OFET application. Thanks to the large overlap of frontier orbitals by crystal structure, pentacene exhibit the fastest mobility, even 6 cm^2/Vs with low surface energy gate dielectric [51], [52]. However, pentacene is vulnerable to the oxidation by exposing oxygen, water and ozone. Hydrogen atoms at the center benzene ring can be substituted by oxygen atoms that results in destruction of π conjugation in pentacene. As a consequence, charge carrier mobility decreases proportional to the extent of oxidation.

To improve the resistance against oxidation of pentacene, Yamamoto and coworkers proposed dinaphtho-[2,3-b:20,30-f]thieno[3,2-b]thiophene (DNTT) (Fig. 2-3f) [53], [54]. DNTT show similar or large mobility compared to pentacene with good overlap of molecular orbital. By replacing central benzene ring in pentacene with two thiophenes, the stability to oxidation improved significantly. Similar to DNTT, 2,6-di[2-(4-phenyl)vinyl]anthracene (DPVAnt) (Fig. 2-3g) offers similar characteristics [55].

For soluble process of small molecules, Anthony and co-workers proposed triisopropylsilylethynyl pentacene (TIPS pentacene) (Fig. 2-3h) [56], [57]. By functionalization of pentacene, the solubility of material increased dramatically. Furthermore, such functionalization help to increase the molecular packaging and reduce the intermolecular distance. The degradation of mobility by oxidation of central benzene ring can be reduced thanks to the functional group. Triethylsilylethynyl anthradithiophene (TESADT) (Fig. 2-3i) [58] and Difluoro-triethylsilylethynyl anthradithiophene (diF-TESADT) (Fig. 2-3j) [59] is similar

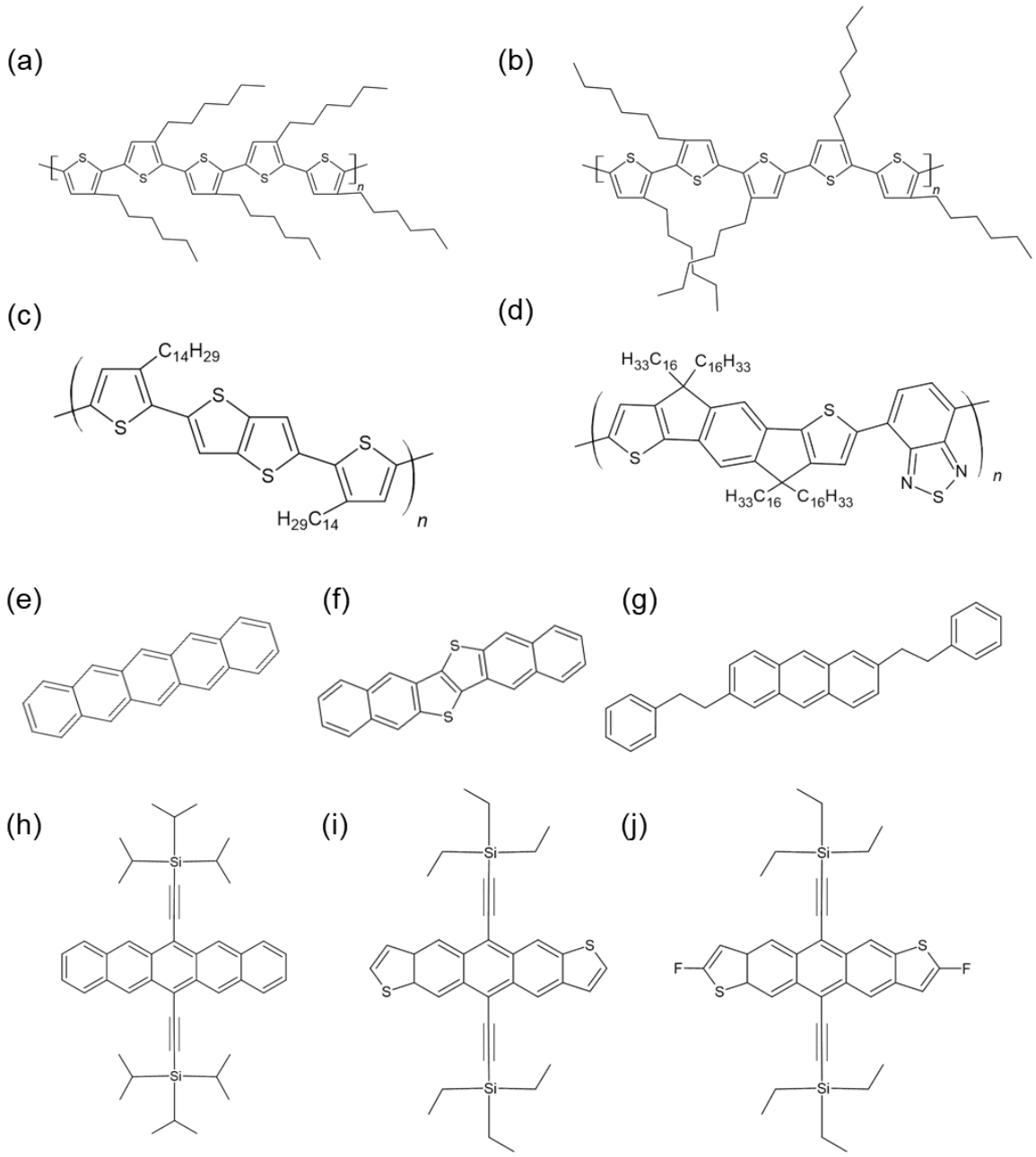

Fig. 2.3. (a) regioregular poly(3-hexylthiophene) (P3HT), (b) regiorandom P3HT, (c) poly(2,5-bis(3-alkylthiophen-2-yl)thieno-[3,2-b]thiophene (pBTTT), (d) indaceno-dithiophene–benzothiadiazole (IDT-BT), (e) pentacene, (f) dinaphtho-[2,3-b:20,30-f]thieno[3,2-b]thiophene (DNTT), (g) 2,6-di[2-(4-phenyl)vinyl] anthracene (DPVAnt), (h) triisopropylsilylethynyl pentacene (TIPS pentacene), (i) triethylsilylethynyl anthradithiophene (TESADT) and (j) difluoro-triethylsilylethynyl anthradithiophene (diF-TESADT).

high soluble small molecules as the TIPS-pentacene.

For small molecules, SAM treatment can enhance the carrier mobility because SAM decreased surface energy on the gate dielectrics and metal electrodes. When the surface energy of pristine gate dielectric and electrode is high such as silicon dioxide and gold, small molecules tend to deposit two dimensionally. This prevents well ordered molecular packaging and reduces charge carrier mobility. SAM such as octadecyltrichlorosilane (OTS) help to increase molecular packaging on the gate dielectric [60], [61]. By three-dimensional molecular stacking, void between grains is reduced and π conjugation increases. Also, Pentafluorobenzene thiol (PFBT) helps to ordered deposition of small molecules such as pentacene [62] and diF-TES-ADT [63], [64] on diverse metal electrodes. SAM treatment on the metal electrode not only increases charge carrier mobility but also decreases contact resistance by enhancing charge injection at metal-semiconductor junction.

2.2 Density of states

The density of states is the number of states that are to be filled by the charge carrier, i.e. electrons and holes, at a particular energy. This DOS structure depends on the material properties such as crystallinity. In this section, we will cover several DOS concept that are commonly adopted in the solid state physics. Particularly, Gaussian DOS for organic disordered semiconductor will be highlighted.

2.2.1 Square-root density of states

Solving a free electron's three-dimensional Schrodinger wave equation results in the parabolic shape of the crystalline inorganic semiconductor as (Fig. 2.4a),

$$g_C(\varepsilon) \propto \sqrt{\varepsilon - \varepsilon_C} \tag{2.1}$$

$$g_V(\varepsilon) \propto \sqrt{\varepsilon_V - \varepsilon} \tag{2.2}$$

where ε_C and ε_V are the conduction band edge and the valence band edge,

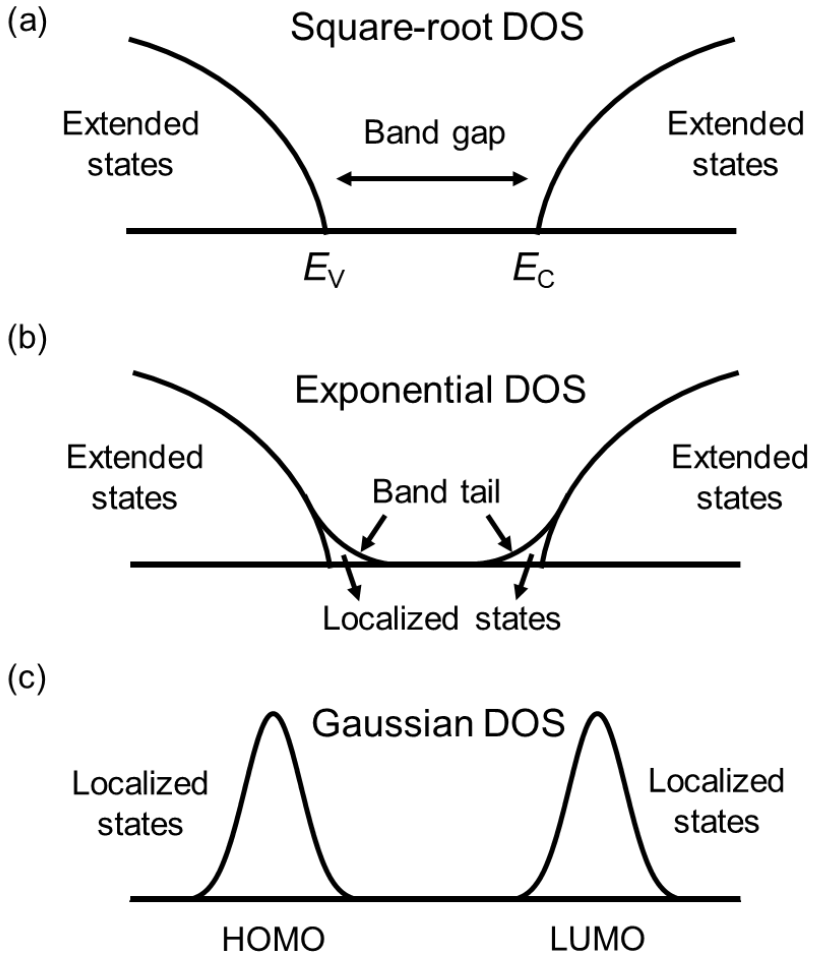

Fig.2.4. Illustration of (a) square-root DOS, (b) exponential DOS and (c) Gaussian DOS

respectively. The square-root DOS falls to zero at these band edge.

The occupied charge density in the DOS can be calculated by the integrating the DOS and the Fermi-Dirac distribution $f_{FD} = \{1 + \exp[(\varepsilon - \varepsilon_F)/kT]\}^{-1}$ with respect to the energy. Here, ε_F is the Fermi energy, k is the Boltzmann constant and T is the temperature. Normally, the integration of DOS and Fermi-Dirac distribution cannot be analytically solved, a simple approximation of the Fermi-Dirac distribution, i.e. Boltzmann distribution allows to lead a simple analytical equation of the occupied charge density as,

$$n = N_C \exp\left(-\frac{\varepsilon_C - \varepsilon_F}{kT}\right), \tag{2.3}$$

$$p = N_V \exp\left(-\frac{\varepsilon_F - \varepsilon_V}{kT}\right). \quad (2.4)$$

Here, N_C and N_V is the effective density of states at each conduction and valence band edge. For silicon, germanium and gallium arsenide, N_C and N_V values are listed up in the Table 2.1.

Table 2.1. The set of N_C and N_V for conventional inorganic semiconductors.

	N_C (cm^{-3})	N_V (cm^{-3})
Silicon (Si)	2.8×10^{19}	1.04×10^{19}
Germanium (Ga)	1.04×10^{19}	6.0×10^{18}
Gallium arsenide (GaAs)	4.7×10^{17}	7.0×10^{18}

2.2.2. Exponential density of states

According to Anderson's model [65], disorder in the amorphous silicon incudes the localization of states. When the disorder exists in the crystalline silicon, its delocalized band changes gradually to the localized states. The degree of disorder can be quantified by the width of the energy band. For the silicon, the width of conduction and valence band is close to 5 eV so that the degree of disorder is low in the amorphous silicon. Therefore, the extended delocalized states and localized states can coexist. Here, the localized states can be commonly described as an exponential band tail states as (Fig. 2.4b),

$$g(\varepsilon) = \frac{N}{\varepsilon_0} \exp\left(\frac{\varepsilon}{\epsilon_0}\right) \quad (2.5)$$

where N is the molecular density and ε_0 is the energy scale of the DOS.

For early research of organic disordered semiconductor, exponential DOS adopted widely to study the charge transport mechanism, e.g. the variable range hopping transport [66] and the multiple-trapping and release model [67]. However, recent study proved that the charge transport of organic disordered semiconductors is governed by the Gaussian DOS rather than the exponential DOS.

2.2.3 Gaussian density of states

In organic disordered semiconductors, the weak van der Waals interaction induces low binding energy between the basic component of the solid. Due to this, only small orbital overlap between molecules exist and electronic bands are narrow. The width of HOMO and LUMO is much lower than that of inorganic counterpart that the tight covalent bonding induces very strong binding energy. Inorganic semiconductors have several eV as a bandwidth, whereas organic semiconductors have the order of 0.1 eV as a bandwidth. According to the Anderson's localization theory, such a small bandwidth induces a strong localization on the disorder; all states are fully localized. This fully localized states can be commonly expressed by the Gaussian distribution as (Fig. 2.4c),

$$g(\varepsilon) = \frac{N_0}{\sigma\sqrt{2\pi}} \exp\left(-\frac{\varepsilon^2}{2\sigma^2}\right), \tag{2.6}$$

where N_0 is the total molecular density and σ the Gaussian width.

For organic disordered semiconductors, effectiveness of the Gaussian DOS versus exponential DOS has been discussed widely. Baranovskii showed a clear evidence of Gaussian DOS by correlating specific charge transport behavior of organic semiconductors and equilibrium energy ε_∞. This energy corresponds to the maximum of $g(\varepsilon) \times f_{\mathrm{FD}}$ and it can be calculated as[68],

$$\varepsilon_\infty = \frac{\int_{-\infty}^{\infty} \varepsilon g(\varepsilon) \exp\left(-\frac{\varepsilon}{kT}\right) d\varepsilon}{\int_{-\infty}^{\infty} g(\varepsilon) \exp\left(-\frac{\varepsilon}{kT}\right) d\varepsilon} = -\frac{\sigma^2}{kT}. \tag{2.7}$$

When the $\varepsilon_\infty - \varepsilon_F \gg kT$ at the low charge concentration *p,* most carriers exists in the vicinity of ε_∞, not ε_F because the DOS below ε_∞ decreases so steeply (Fig. 2.5a). This result is at variance at the exponential DOS that most carriers occupy at ε_F in spite of the low *p* (Fig. 2.5b). Existence of ε_∞ induces exceptional charge transport behavior of organic semiconductors. First, mobility is constant at low *p* and is *p* dependent at high *p* [69] (Fig. 2.6a). The charge transport in Gaussian DOS occurs by hopping toward the particular energy level, so-called 'transport energy ε_t' from the energy of initially occupied state. If $\varepsilon_\infty > \varepsilon_F$, the initial occupied energy level is equal to ε_∞ that is independent to the position of ε_F. If $\varepsilon_\infty < \varepsilon_F$, the initial occupied energy level corresponds to ε_F. Therefore, the hopping mobility is constant at low *p* regardless of *p*, whereas

the mobility increases depending on the p at high p value. This p dependent mobility cannot be explained by the exponential DOS. Second, a single charge carrier in the empty Gaussian DOS system is non-dispersive transport; charge hopping stops diving further than ε_∞ at some relaxation time although the states are empty below ε_∞ [68] (Fig. 2.6b). This result is a clear evidence of the ε_∞ and Gaussian DOS in the organic disordered semiconductors because dispersive transport occurs in the exponential DOS.

The occupied charge density can be calculated by,

$$p = \int_{-\infty}^{\infty} g(\varepsilon) f_{FD}(\varepsilon, \varepsilon_F) d\varepsilon \,. \tag{2.8}$$

Eq. (2.8) can be expressed under the Boltzmann approximation as,

$$p = N_0 \exp\left[-\frac{1}{kT}\left\{\varepsilon_F - \left(\mathrm{HOMO}_{\max} + \frac{\sigma^2}{2kT}\right)\right\}\right]. \tag{2.9}$$

where $\mathrm{HOMO}_{\max}$ is the energy at the maximum of HOMO. This charge density p is only effective for the non-degenerate condition because of the Boltzmann approximation. Remarkable researches pointed out [40], [70] that organic semiconductors belong to the non-degenerate condition only at very low p in the Gaussian DOS, i.e. ε_F situates far from the $\mathrm{HOMO}_{\max}$. When p increases, the Boltzmann approximation is not valid anymore so that Gaussian DOS leads to the degenerate condition that the relation between p and ε_F is not analytical. Here, p can be semi-analytically as,

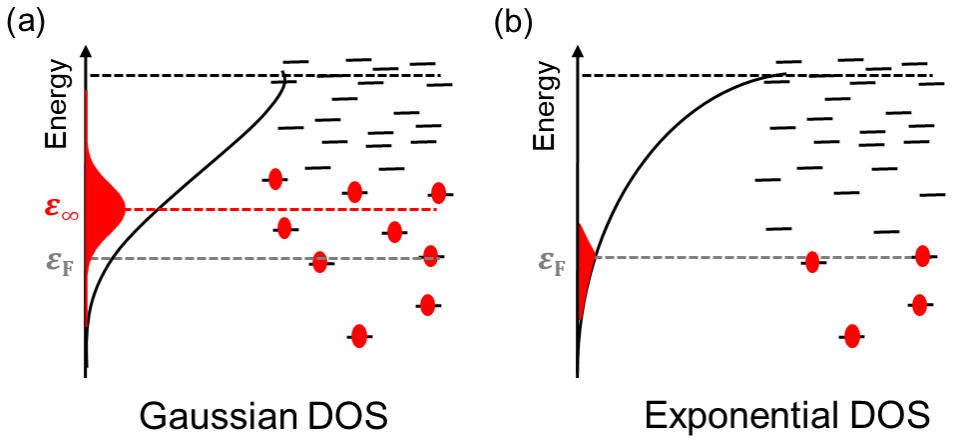

Fig. 2.5. Schematic of occupied charge density in the (a) Gaussian DOS and (b) exponential DOS.

$$p = \frac{N_0}{2}\,\mathrm{erfc}\left[\frac{\varepsilon_F - \mathrm{HOMO_{max}}}{\sqrt{2}\sigma}\right]. \tag{2.10}$$

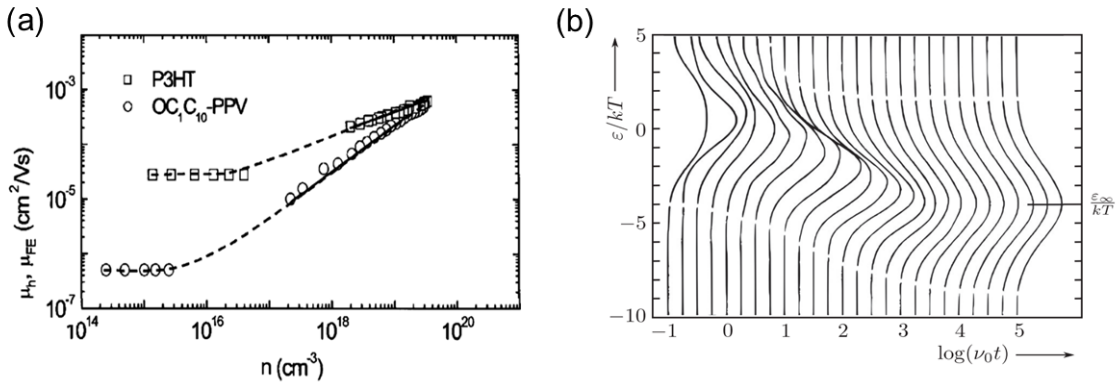

Fig. 2.6. (a) Field-effect mobility with respect to the charge density for P3HT and OC1C10-PPV from [69]. (b) Time dependent distribution of charge energy in the Gaussian DOS from [68]

2.3 Threshold voltage

In a field-effect transistor, the threshold voltage V_{T} is the gate voltage at which a transistor shifts between its 'on' state and its 'off' state. Before the gate voltage V_{GS} reaches to V_{T}, a conductive channel does not exist between source and drain electrodes (Fig. 2.7a) This state is literally 'off' state. When the gate voltage goes beyond V_{T}, a conductive channel is finally created (Fig. 2.7b). This state is literally 'on' state. In industrial point of view, V_{T} is one of the most important parameters in all transistors and circuits because if V_{T} is not optimized, the design of complex circuits is very difficult. Therefore, accurate understanding of V_{T} is mandatory.

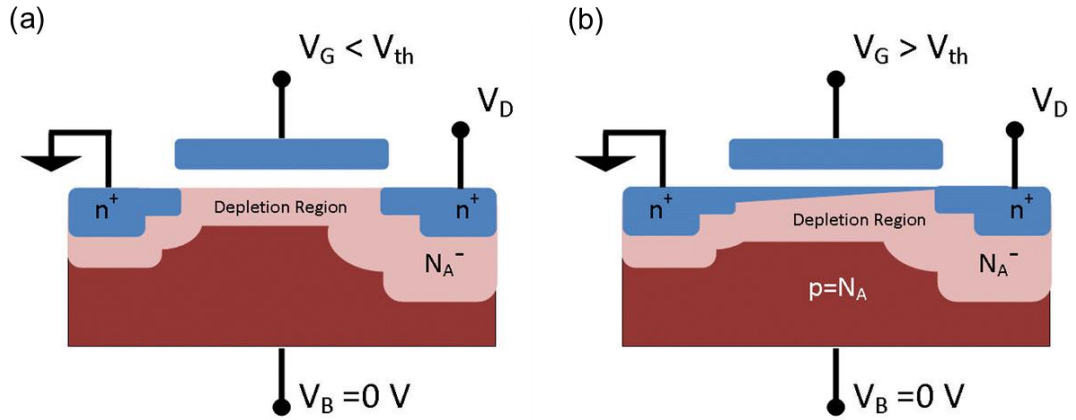

Fig. 2.7. Schematic of (a) below and (b) above threshold operation in n-type MOSFET.

2.3.1 Extraction methods

Extraction methods of the threshold voltage have been widely studied because of the importance of reliable value of the threshold voltage [71]–[73]. Commonly, a linear or saturation transfer characteristic of a single transistor determines the threshold behavior. Depending on the semiconductor material and device structure, the selection of the extraction method should be careful. Extrinsic factors such as disorder of semiconductor and high contact resistance can induce a non-linear transfer characteristic and this sometimes results in inaccurate extraction of the threshold voltage [12], [74], [75]. In this section, we review widely-accepted extraction method of the threshold voltage.

The simplest method is the constant-current method (Fig. 2.8a). Because a single point of voltage-current measurement determines the threshold voltage quickly, this method is widely used in industry. A common value of a constant drain current is $W/L \times 10^{-7}$, where W is the channel width and L the channel length [76]. However, this method highly depends on the constant drain current.

Linear extrapolation method in the linear transfer characteristics (Fig. 2.8b) and in the transconductance (Fig. 2.8c) are also popular method to extract the threshold voltage. When the linear extrapolation at the maximum transconductance (maximum slope) is plotted, the threshold voltage corresponds to the V_{GS}-axis intercept, i.e. the drain current or the transconductance equals to 0. This method originated from the ideal drain current equation at the linear condition as,

$$I_D = \frac{W}{L}\mu C_i(V_{GS} - V_T)V_{DS} \tag{2.11}$$

where μ is the mobility and C_i is the capacitance of gate dielectric. In contrast, this method is inaccurate with the non-linear transfer curves due to the V_{GS} dependent mobility or high contact resistance [12], [75].

The second derivative method can be an alternative method because this method can ignore the effect of high contact resistance (Fig. 2.8d). The maximum of the derivate of the transconductance indicates the threshold voltage by this method. This method is very sensitive to the noise so that suppression of the noise is important. For OFET devices, the second derivate method frequently adopted to avoid the effect of high contact resistance [77], [78].

The threshold voltage can be extracted in the saturation region (Fig. 2.8e). The saturation extrapolation method determines the threshold voltage from the V_{GS}-axis intercept of linearly extrapolated fit to the $\sqrt{I_D}$ vs V_{GS} curve at the maximum transconductance (maximum slope). This method stem from the ideal drain current equation at saturation regime as,

$$I_D = \frac{W}{L}\mu C_i(V_{GS} - V_T)^2. \tag{2.12}$$

Lastly the ratio η can be numerically and analytically calculated by,

$$\eta = \frac{\partial R_{\mathrm{on}}/\partial V_{\mathrm{GS}}}{\partial^2 R_{\mathrm{on}}/\partial V_{\mathrm{GS}}^2} = \frac{V_{\mathrm{GS}} - V_{\mathrm{T}}^{\mathrm{eff}}}{\gamma + 2}, \tag{2.13}$$

where R_{on} is the on-state resistance and γ is the exponent of the power-law dependency. The analytical solution allows to determine $V_{\mathrm{T}}^{\mathrm{eff}}$ and γ by a linear fit to numerical solution (Fig. 2.8f). The method excludes the effect of the drain voltage on V_{T} by $V_{\mathrm{T}}^{\mathrm{eff}} = V_{\mathrm{T}} + V_{\mathrm{DS}}/2$ [79]. In addition, the method is suitable not only for a transistor consisting of a crystalline semiconductor that exhibits perfectly linear transfer characteristics but also for a transistor consisting of a semiconductor with disorder or traps that exhibits a superlinear or a sublinear transfer characteristics due to V_{GS}-dependent mobility and contact resistance by power law.

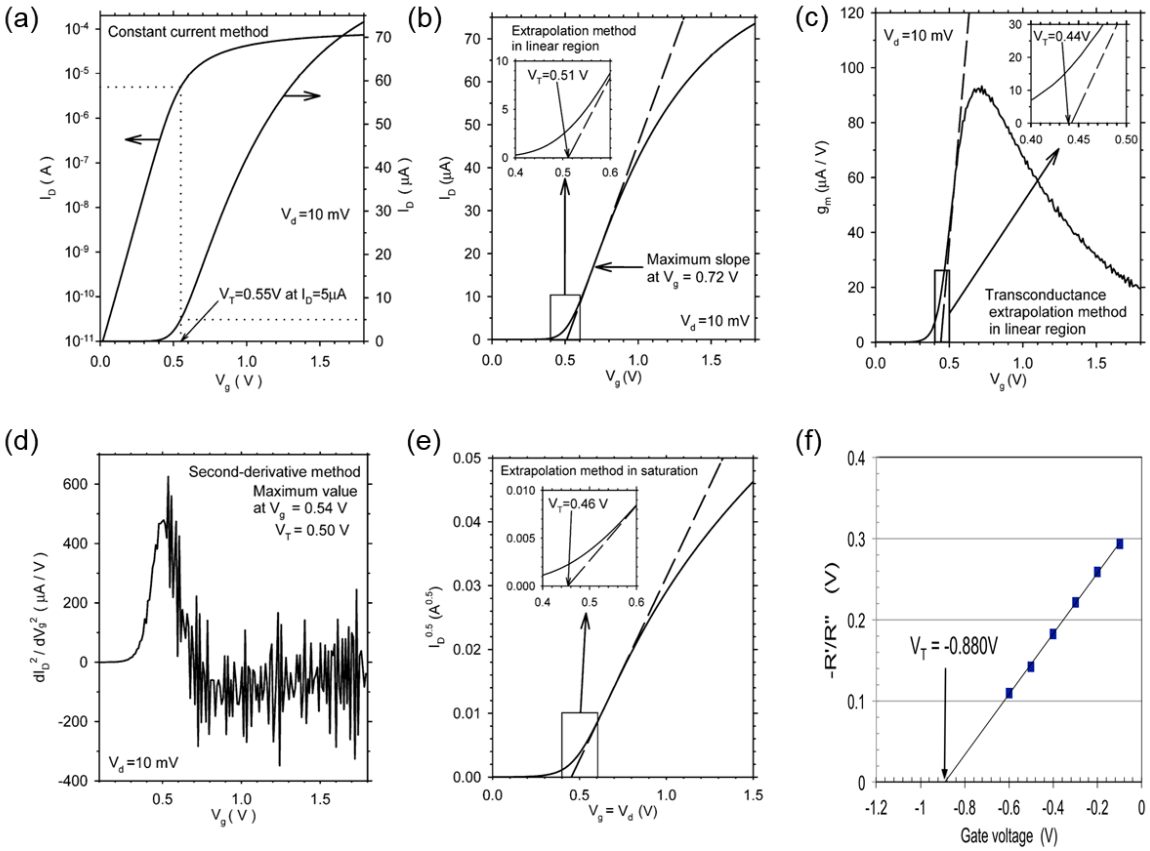

Fig. 2.8. Threshold voltage extraction by (a) constant current method, (b) linear extrapolation method, (c) linear transconductance extrapolation method, (d) second derivative method, (e) saturation extrapolation method and (f) ratio method. The extraction result from [72] and [73].

2.3.2. Physical origin of the threshold voltage in various transistors

The physical origin of the threshold voltage depends on the type of the field-effect transistors. We now compare the threshold voltage of OFETs to that of metal-oxide-semiconductor field-effect transistors (MOSFETs) and a-Si TFTs (Fig. 2.9). In MOSFETs that operate in inversion mode, the channel threshold is the intrinsic origin of V_T^{eff}. The channel is created as a result of a strong inversion, in which the density of minority carriers exceeds that of majority carriers. The onset of strong inversion is clearly defined also in band diagram (Fig. 2.9a). At threshold, the surface potential V_S is twice the bulk potential V_F so that $qV_S = 2 \cdot qV_F$ where q is the elementary charge, which can be derived from the assumption of the surface minority carrier equal to the bulk majority carrier [71].

For a-Si TFTs that operate in accumulation mode, the mobility threshold

is the intrinsic origin of V_T^{eff} due to inherent exponential trap states [80]. Although the increase of V_{GS} makes charge carriers accumulate in the DOS, the device does not conduct current until the Fermi level reaches close to a particular level, i.e. the 'mobility edge'. This threshold behavior of a-Si TFT can be described by the DOS structure based on the multiple trapping and thermal release (MTR) model [81]. When the Fermi level is far below than the mobility edge, all of the carriers are trapped in exponential trap states. However, trap states release charge carriers into the extended states when the Fermi level increases and thermal energy of charge carriers kT can overcome the activation energy E_a. (Fig. 2.9b). Therefore, this threshold behavior of a-Si TFTs is better described by the mobility threshold than the channel threshold.

In OFETs, the channel threshold is the internal origin of V_T^{eff}. OFETs operate in the accumulation regime [17], [79] unlike its most of conventional inorganic counterpart, i.e. crystalline Silicon-based MOSFETs, which operate in the inversion regime [71]. Therefore, the physical meaning of V_T differs in these two types of transistor. Early reports explained the threshold behavior of OFETs in regards to the accumulation regime operation. Horowitz [17] attributed the origin of V_T to a dependence of carrier mobility of gate voltage V_{GS} by developing a comprehensive OFET model in the accumulation regime similar to

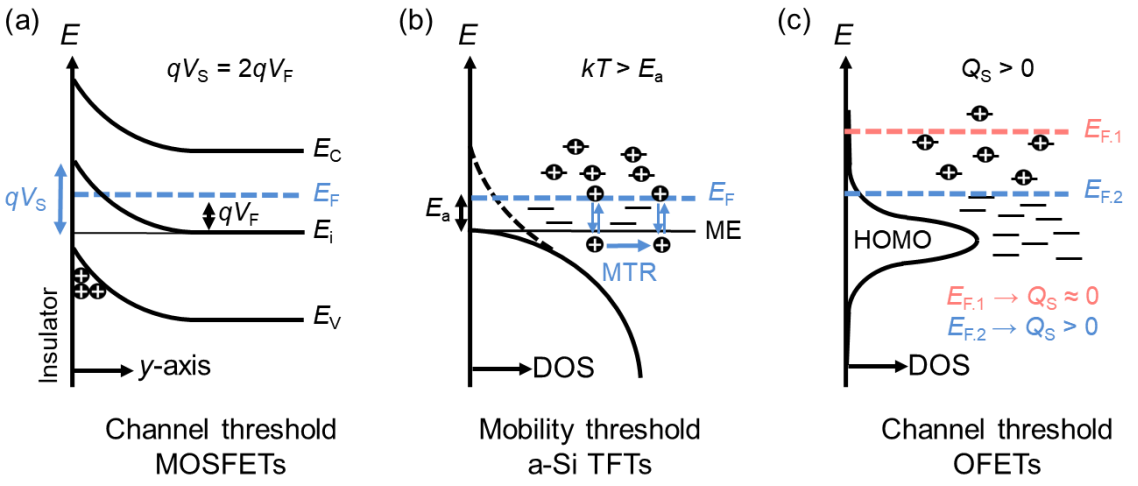

Fig. 2.9. Schematics of intrinsic non-zero $\boldsymbol{V_T^{eff}}$ origin for (a) MOSFET, (b) a-Si TFT and (c) OFET. $\boldsymbol{V_s}$ and $\boldsymbol{V_F}$ represent the surface and bulk potential, ME mobility edge, $\boldsymbol{E_a}$ activation energy, $\boldsymbol{kT}$ thermal energy and MTR multiple trapping and thermal release model.

the amorphous silicon thin-film transistor (a-Si TFT) [80]. In addition, Jung and coworkers proved numerically that V_T in OFETs is the onset of charge carrier accumulation in the channel [79]. At threshold, a significant amount of charge carriers is injected into the semiconductor and is accumulated at the surface ($Q_S > 0$) creating a conducting channel (Fig. 2.9c).. This threshold behavior of OFETs is analogous to that of MOSFETs despite the difference in operation mode. This result suggests that channel formation determines in general the threshold voltage of trap-free devices.

2.4 Charge transport in organic disordered semiconductors

It is difficult to understand the charge transport model of organic semiconductors for various materials that have diverse energetic configurations by the process-dependent microstructure and molecular structure of organic semiconductor. To comprehend charge transport behavior of organic semiconductors, many models have been studied and developed such as the band-like transport, multiple trapping-release (MTR) model and GDM. In this section, we introduce Gaussian disorder models that accounts for the hopping transport between localized states due to the weak inter-molecular bonding for both polymers and small molecules.

2.4.1 Gaussian disorder model

The Gaussian disorder model is the model of thermally-assisted hopping transport within randomly distributed localized states (Fig. 2.10). Principal assumptions of the GDM are the Gaussian DOS and the Miller-Abrahams (MA) hopping transition rate. The MA transition rate is the frequency of charge carrier hopping from an occupied state *i* to an unoccupied state *j*,

$$\nu_{ij} = \nu_0 \exp\left(-\frac{2r_{ij}}{a} - \frac{\varepsilon_j - \varepsilon_i + |\varepsilon_i - \varepsilon_j|}{2kT}\right), \tag{2.14}$$

where a is the localization length of a charge carrier, r_{ij} the distance between site *i* and *j*, ε_j and ε_i the energies of initial and final state and *k* the Boltzmann constant and *T* the temperature. A prefactor ν_0 is the attempt-to-escape frequency, typically in the range of 10^{12} to 10^{13} s^{-1}[82], [83].

As an initiative work, Bassler proposed the mobility model that depends on the electric-field F and temperature T within a cubic lattice system. Parametrized equation of the mobility can be expressed as [68],

$$\mu(F) = \mu_0 \times \exp\left\{-\left(\frac{2\sigma}{3kT}\right)^2\right\} \times \exp\left\{\left[\tilde{C}\left(\frac{\sigma}{kT}\right)^2 - \tilde{B}\right]\sqrt{F}\right\} \qquad (2.15)$$

where μ_0 is mobility prefactor, $\tilde{C}$ the parameter to account for the lattice constant. $\tilde{B}$ is the parameter to consider the spatial disorder of the system. $\tilde{B} = 2.25$ for $\Sigma < 1.5$ and $\tilde{B} = \Sigma^2$ for $\Sigma > 1.5$ where Σ is the non-diagonal disorder to consider the spatial disorder in the cubic lattice model. For spatial distribution of localized states in GDMs, 2 different conditions were commonly studied; a rigid cubic lattice model that mimic the crystalline structure (Fig. 2.11a) and the spatial disorder model that represents the fully disordered structure (Fig. 2.11b).

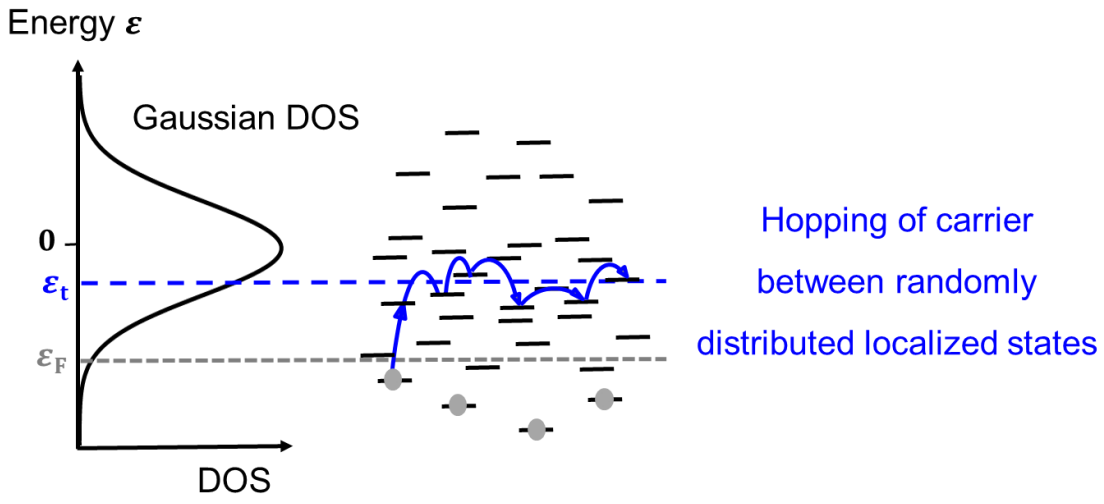

Fig.2.10. Schematic of the Gaussian disorder model in the Gaussian DOS. Charge carriers hop adjacent to the so-called 'transport energy $\boldsymbol{\varepsilon_t}$'.

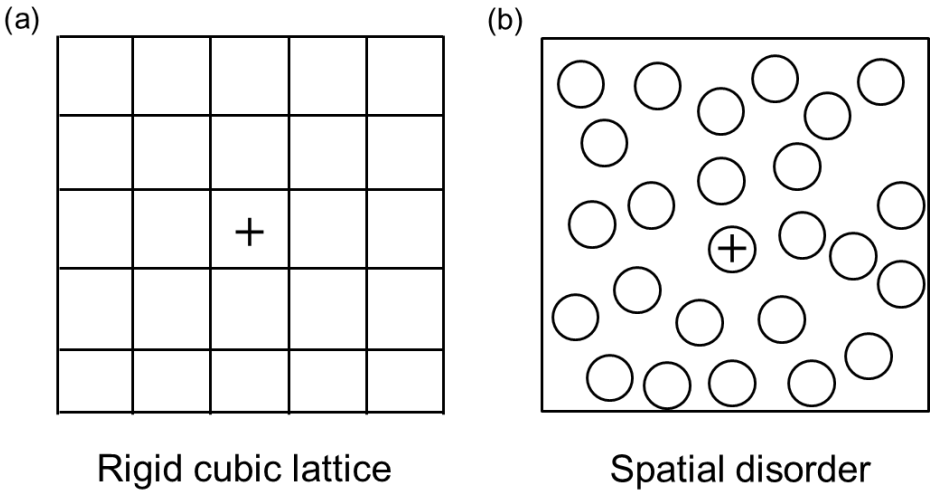

Fig.2.11. Schematic of rigid cubic lattice model and spatial disorder model for the spatial distribution of localized states for the GDM.

2.4.2 Extended Gaussian disorder model in cubic lattice

Pasveer and coworkers proposed the GDM with the rigid cubic lattce, i.e. the spatial disorder was completely eliminated by $\Sigma = 0$. This model is so-called extended GDM (EGDM) and they considered the charge carrier dependency of the mobility [84]. Today, EGDM is the most widely accepted hopping transport model for ODSs and many commercial simulation software provide this model for users [85], [86].

The mobility of the EGDM at the low electric field *F* is a function of T and carrier density p as [84],

$$\mu(T,p) = \mu_0(T) \times \exp\left[\frac{1}{2}(\hat{\sigma}^2 - \hat{\sigma})(2pb^3)^{\delta}\right], \tag{2.16}$$

where $\hat{\sigma} = \sigma/kT$, b is the intersite distance and $\delta \equiv 2(\ln(\hat{\sigma}^2 - \hat{\sigma}) - \ln(\ln 4))/\hat{\sigma}^2$. Here, $\mu_0(T)$ is the T dependent zero-carrier mobility which has the form,

$$\mu_0(T) = \mu_0 \times c_1 \exp(-c_2\hat{\sigma}^2), \tag{2.17}$$

where $\mu_0 = b^2\nu_0 e/\sigma$, e the elementary charge and c_1 and c_2 are parametrized constants.

The mobility of the EGDM at the high electric field is a function of T, p F as,

$$\mu(T,p,F) = \mu(T,p)g(T,E), \tag{2.18}$$

and the dimensionless prefactor $g(T,E)$ is parametrized by,

$$g(T,E) = \exp\left\{0.44\left(\hat{\sigma}^{\frac{3}{2}} - 2.2\right)\left[\sqrt{1 + 0.8\left(\frac{Feb}{\sigma}\right)^2} - 1\right]\right\}. \tag{2.19}$$

The parametrization of c_1 and c_2 in Eq. (2.17) were carried out by a fitting between Eq. (2.16) and a numerical result of master equation,

$$\sum_{\mathrm{j}\neq\mathrm{i}}\left[\nu_{\mathrm{ij}} \cdot p_{\mathrm{i}}\left(1 - p_{\mathrm{j}}\right) - \nu_{\mathrm{ji}} \cdot p_{\mathrm{j}}(1 - p_{\mathrm{i}})\right] = 0\,. \tag{2.20}$$

Here, p_{i} is the probability of charge occupation on site *i*. Based on this method, initial parametrization of EGDM was $c_1 = 1.8 \times 10^{-9}$ and $c_2 = 0.42$ at $N_0 \cdot a^3 = 10^{-3}$ [84].

2.4.3 Gaussian disorder model in spatial disorder

Baranovskii and coworkers proposed a solution of GDM by a transport energy [82], [87], [88] for any steeply energy-dependent DOS, i.e. exponential DOS and Gaussian DOS. At the low electric field, the mean time of upward hopping transition rate toward the transport energy from states below the transport energy determines mobility. At the high electric field, a concept of the effective temperature was adopted to describe charge transport behavior [89], [90]. During the derivation of GDM by Baranovskii, the model assumed consistently both the spatial disorder and a variable-range hopping (VRH) that led a more precise GDM than previous EGDM.

The basic idea of the model is that every charge carrier hopping occurs by multiple activation and relaxation of carriers via the transport energy ε_{t} in Gaussian DOS [87], [91]. Charge carriers at states below ε_{t} hop upwards and carriers at states above ε_{t} hop downwards towards ε_{t}.

With Fermi level ε_{F} estimated by the Gauss-Fermi integration, the transport energy ε_{t} for a finite charge carrier density in the Gaussian DOS is determined by [87]

$$\frac{2}{3}\left(\frac{4\pi}{3B_c}\right)^{-\frac{1}{3}}\frac{kT}{a}\left[\int_{-\infty}^{\varepsilon_t}[1-f(\varepsilon,\varepsilon_F)]g(\varepsilon)d\varepsilon\right]^{-\frac{4}{3}}\times[1-f(\varepsilon_t,\varepsilon_F)]g(\varepsilon_t)=1, \quad (2.21)$$

where $f(\varepsilon,\varepsilon_F)$ is the Fermi function. Validity of the derived ε_t was examined by numerical simulation [92]. One can calculate the hopping distance $r(\varepsilon_t)$ by

$$r(\varepsilon_t)=\left[\frac{4\pi}{3}\int_{-\infty}^{\varepsilon_t}g(\varepsilon')[1-f(\varepsilon',\varepsilon_F)]d\varepsilon'\right]^{-\frac{1}{3}}. \quad (2.22)$$

Then, the carrier mobility can be calculated with the generalized Einstein relation via [82], [87]

$$\mu\simeq\frac{e}{kT}F_{ER}\frac{r^2(\varepsilon_t)}{\langle t\rangle}, \quad (2.23)$$

where F_{ER} is dimensionless function for generalized Einstein relation [93] as,

$$F_{ER}=\frac{\int_{-\infty}^{\infty}d\varepsilon g(\epsilon)\frac{\exp[(\varepsilon-\varepsilon_F)/kT]}{(1+\exp[(\varepsilon-\varepsilon_F)/kT])^{\,2}}}{\int_{-\infty}^{\infty}d\varepsilon g(\epsilon)\frac{1}{(1+\exp[(\varepsilon-\varepsilon_F)/kT])}}, \quad (2.24)$$

and $\langle t\rangle$ is the average upward hopping time for all states below ε_t as [94], [95],

$$\langle t\rangle=\nu_0^{-1}\frac{\int_{-\infty}^{\varepsilon_t}\exp\left[\frac{2B_c^{1/3}r(\varepsilon_t)}{a}+\frac{\varepsilon_t-\varepsilon}{kT}\right]g(\varepsilon)[1-f(\varepsilon)]d\varepsilon}{\int_{-\infty}^{\varepsilon_t}g(\varepsilon)[1-f(\varepsilon)]\,d\varepsilon}. \quad (2.25)$$

Here, $\langle t\rangle$ neglects downward hopping transition rates because it is exponentially faster than upward hopping. Finally, the charge carrier mobility at low electric field of GDM by Baranovskii by using Eq. (2.23) and Eq. (2.25) is

$$\mu\simeq\nu_0\frac{e}{kT}\frac{3B_cF_{ER}}{4\pi r(\varepsilon_t)p}\times\exp\left(-\frac{2B_c^{1/3}}{a}r(\varepsilon_t)-\frac{\varepsilon_t-\varepsilon_F}{kT}\right). \quad (2.26)$$

2.5 Charge carrier injection

2.5.1 Injection barrier

At the ideal metal/semiconductor junction, the injection barrier that is an energetic mismatch between Fermi levels of two materials can be defined by the Schottky-Mott rule [58,59]. As the vacuum level of two layers are aligned in the Schottky-Mott limit (Fig. 2.12a), the injection barriers for electrons $E_{b.n}$ and holes $E_{b.p}$ can be expressed as,

$$E_{b.n} = \Phi - EA, \tag{2.27}$$

$$E_{b.p} = IE - \Phi, \tag{2.28}$$

where Φ denotes the work function of metal, *EA* the electron affinity and *IE* the ionization energy. The ideal Schottky-Mott limit considers only the energetic level of metals and semiconductors to determine the barrier height. In other words, the injection barrier will change when energetic levels are varied. Also, there are no gap states in the forbidden gap that induces very sharp edge of HOMO (or E_V) and LUMO (or E_C) level.

By injection barrier, one can quantify injected charge density at the metal/semiconductor junction. When the band edge is clearly defined with square-root DOS, the charge density at the metal/semiconductor junction can be calculated by Eq. (2.3) and (2.4) with the Boltzmann statistics as an exponential function of the injection barrier. Therefore, charge carrier increases exponentially with decreasing injection barrier. Depending on the magnitude of $E_{b.n}$ and $E_{b.p}$, the dominant charge polarity is determined. That is to say, the hole dominant device, i.e. p-type conduction, is expected when $E_{b.p} < E_{b.n}$, whereas the electron dominant device, i.e. n-type conduction, is expected when $E_{b.p} > E_{b.n}$. In the case of $E_{b.p} \approx E_{b.n}$, both electrons and holes can be injected from the metal and ambipolar conductor can take place.

2.5.2 Non-ideal factors

In the realistic metal/semiconductor junction, the Schottky-Mott limit is not always effective (Fig. 2.12b) [60]. The primary non-ideal factors at the metal/semiconductor junction is an interface dipole that induces a significant shift

of injection barrier. The interface dipole can cause by several origins such as induced dipoles by a self-assembly monolayer [61], charge transfer [62]. The interface dipole creates the dipole moment vector that induces the mismatch of the vacuum level Δ between metal and semiconductor layer. As a consequence, injection barrier increases or decreases depending on the direction of dipole moment vector. For example, the positive dipole moment vector lifts the vacuum level and thereby the injection barrier for holes decreases. This is widely adopted method to increase charge injection via self-assembly monolayer [22,23,61,63]. Sometimes, the contamination on the metal surface impedes the formation of interface dipole and affects on the charge injection [64,65]. With considering vacuum level mismatch by the interface dipole, the injection barrier can be newly defined as,

$$E_{b.n} = \Phi + \Delta - EA, \tag{2.29}$$

$$E_{b.p} = IE - (\Phi + \Delta). \tag{2.30}$$

Secondly, the Fermi level pinning can break the Schottky-Mott rule. When the density of interfacial states exists at the metal/semiconductor junction, charge carriers fill until these states are totally occupied. If the interface states are very high, all carriers would be trapped at the energetic level of interface trap states and therefore the Fermi level is pinned. This phenomenon means that the injection barrier is independent to the work function of metal and injection barrier cannot be controlled.

Lastly, the energetic disorder of DOS is another non-ideal factor. As we described in Sec. 2.2.3, the weak intermolecular binding energy in the amorphous organic solid induces the absence of long-range order and it results in the energetic disorder, i.e. Gaussian DOS. In fact, this energetic disorder of HOMO and LUMO is non-trivial to define the injection barrier because the disorder causes the divergent definition of the *EA* and *IE*. Therefore, in organic disordered semiconductors, the onset [66] or the maximum [67] of HOMO and LUMO are widely adopted to define *EA* and *IE*. However, these methods cannot guarantee a strict band edge due to the gap states.

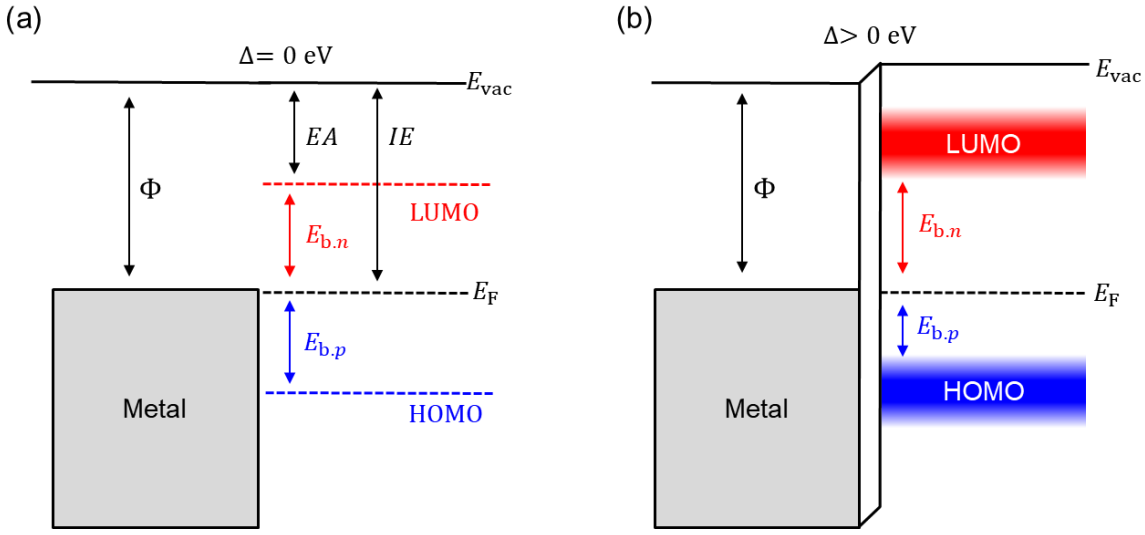

Fig.2.12 (a) Energy diagram of the ideal metal/semiconductor junction. Here, Φ denotes the work function of metal, *EA* the electron affinity, *IE* the ionization energy, $E_{b.n}$ injection barrier for electrons and $E_{b.p}$ injection barrier for holes. (b) Energy diagram of a realistic metal/semiconductor junction. Here Δ is the mismatch of vacuum level. HOMO and LUMO band exhibit the energetic disorder.

Chapter 3

Methods

3.1 Numerical simulation

A commercial numerical software ATLAS from Silvaco. Inc. [85] is used in entire works. ATLAS is finite-element method (FEM) based technology computer-aided design (TCAD) tool to simulate semiconductor devices. It helps to correlate between physical descriptions and device configuration that is essential to design devices or circuits. This simulator allows to model organic electronic devices such as OLEDs, OPVs and OFETs with physical models of organic semiconductors.

The main advantage of TCAD simulator is that we can simply predict electrical output of devices with various material condition. Properties of each material can be defined by relative permittivity, HOMO and LUMO level, Gaussian width for organic disordered semiconductors and by work function for metal electrode. Also, various geometrical and energetical configuration can be tested. For example, it helps to optimize the device through simulation with various thickness of each thin film.

However, the numerical simulation does not give a solution for any input condition. They calculate various equation simultaneously. If the output is not self-consistently acquired, the calculation would be never converged. Therefore, selection of appropriate material parameters, mesh definition and boundary condition is very important.

Particularly, defining mesh is important. Mesh in the TCAD simulator can be defined by series of vertical and horizontal lines (Fig. 3.1) The point where a vertical line and a horizontal line meet is called a node. All calculation is occurred

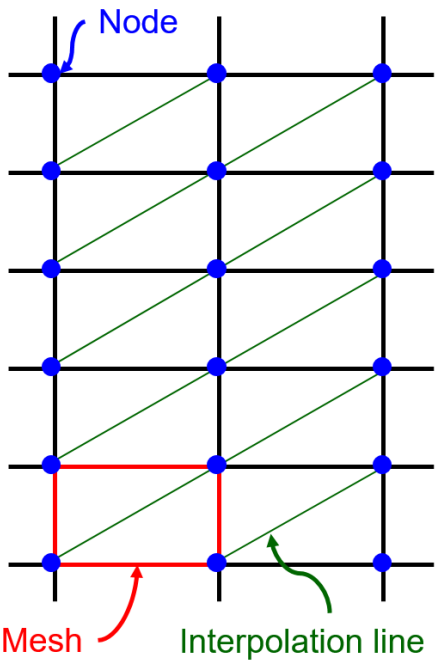

Fig. 3.1. Schematic of mesh definition in ATLAS.

in these nodes and the other regions is calculated by interpolation between nodes. Although highly dense mesh is effective to increase the reliability of the calculation, the consuming time for calculation will increase.

In each mesh, the simulator calculate basic semiconductor equations such as Poisson's, continuity and current equations in the self-consistent manner. In addition, we considered additional physical equations for organic disordered semiconductors, e.g. Gaussian DOS, generalized Einstein relation. As for the transport model, two GDMs, EGDM in cubic lattice and GDM in spatial disorder. Thanks to the intimate cooperation of Silvaco Europe Ltd in the United Kingdom, we can successfully implement the new GDM with spatial disorder into ATLAS.

3.2 Energetic structure

The energetic structure of organic disordered semiconductor is defined by double Gaussian DOS system (Fig. 3.2). The injection barrier E_b is defined by the energy difference between the Fermi level and maximum of HOMO [41]. The Fermi level before junction formation was assumed to be same with a work function of gate electrode W_G. The position and shape of the intrinsic Gaussian

DOS is determined by E_b and Gaussian degree of disorder σ_i and total DOS, N_i. In addition to the intrinsic Gaussian DOS, we considered a secondary Gaussian DOS that accounts for the extrinsic trap states [96]. As shown in Fig. 3.2 (c), σ_d represents Gaussian degree of disorder for trap DOS, E_d the energy difference between the maximum of each DOS function. The complete energetic structure $g(E)$ is described by the following equation:

$$g(\varepsilon) = \frac{N_i}{\sigma_i\sqrt{2\pi}}\exp\left(-\frac{\varepsilon^2}{2\sigma_i^2}\right) + \frac{N_d}{\sigma_d\sqrt{2\pi}}\exp\left(-\frac{\varepsilon^2}{2\sigma_d^2}\right), \quad (3.1)$$

where N_d is the total trap DOS. In addition, we define the node as the energy where two Gaussian functions coincide. The trapped charges in these extrinsic trap states, induced by the gate bias, are assumed to be fixed in the device and thereby they do not contribute to the drain current [97].

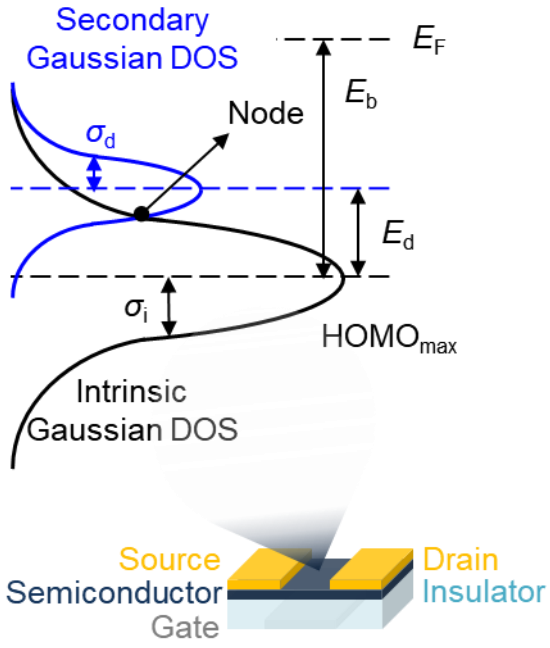

Fig. 3.2. Energetic structure of organic disordered semiconductors by double Gaussian DOS system.

Chapter 4

Threshold voltage modeling

V_T is one of the most important parameters in all transistors and circuits. If V_T is not optimized, the design of complex circuits is difficult. For organic field-effect transistors (OFETs), the threshold behavior has been widely studied by the charge accumulation in the intrinsic DOS [17], [74], [79] and the charge trapping in the extrinsic trap DOS [97] that mainly originated from intrinsic and extrinsic factors such as disorder of semiconductor [98], humidity [99], applied gate or drain bias [100], [101] and the thickness of the semiconductor film [102]. However, understanding of the threshold behavior by the energetic disorder of intrinsic and trap DOSs is still lacking in spite of the disordered nature of organic semiconductors, i.e. fully-localized Gaussian DOS through which both charge transport and injection take place [82]. This distinctive energetic structure of organic semiconductors could make the charge-accumulation process, and hence the threshold behavior, different.

Considering Gaussian DOS for the intrinsic DOS, Scheinert et al. developed a numerical OFET model with the fixed interface charges to modulate V_T [103] and Hain et al. derived the analytical compact V_T model with the constant trap states [104]. Although these early reports modelled the threshold behavior of OFETs in regards to the energetic disorder in the intrinsic DOS, both studies lacked the effect of the charge trapping in the energy-dependent trap DOS on V_T. The trap DOS has been modelled using discrete levels [105]–[107], an exponential distribution [108], [109], and a Gaussian distribution [110], [111]. The interpretation of photo-emission spectra [40], [112] and the host-guest dopant system of ODSs [113]–[115] favor the choice of double-Gaussian DOS. Previous work on that topic considered double Gaussian DOS has focused on their effect on charge transport in ODSs [110]–[115]. A study should be conducted to

determine how the Gaussian trap DOS alters charge carrier accumulation and subsequent threshold behavior in OFETs with ODSs.

The aim of this work is to understand the effect of charge trapping in the secondary Gaussian trap DOS on threshold behavior through the double Gaussian DOS model and accumulation mode operation of OFETs. By varying an energetic position of the secondary Gaussian trap DOS from the intrinsic Gaussian DOS, we extract the Fermi-level, surface charge density and the gate-voltage dependent field-effect mobility. These parameters allow to clarify a physical mechanism of the charge filling into Gaussian intrinsic and trap DOSs as well as the concomitant effect on the V_{T}.

In Sec. 4.1, we examined the ratio method that is reliable V_{T} extraction mehtod for non-linear transfer characteristics. Also, we demonstrate the physical meaning of V_{T} through the single Gaussian DOS and the accumulation mode operation. In Sec. 4.2, the charge trapping in the secondary Gaussian trap DOS is comprehended by the double Gaussian DOS model. Also, relevant variation of the threshold behavior and the power-law mobility are studied. Lastly, the experimental validation is studied by numerical fitting to experimental data.

4.1 Effect of single Gaussian density of states

4.1.1 Validation of the ratio method

First and foremost, a quantitative analysis on threshold behavior requires a precise, simple and rigorous extraction method for the threshold voltage. In this study, we used the ratio method to extract the effective threshold voltage $V_{\mathrm{T}}^{\mathrm{eff}}$ [116], [117]. The ratio η can be numerically and analytically calculated by,

$$\eta = \frac{\partial R_{\mathrm{on}}/\partial V_{\mathrm{GS}}}{\partial^2 R_{\mathrm{on}}/\partial V_{\mathrm{GS}}^2} = \frac{V_{\mathrm{GS}} - V_{\mathrm{T}}^{\mathrm{eff}}}{\gamma + 2}, \tag{4.1}$$

where R_{on} is the on-state resistance and γ is the exponent of the power-law dependency. The analytical solution allows to determine $V_{\mathrm{T}}^{\mathrm{eff}}$ and γ by a linear fit to numerical solution. The method excludes the effect of the drain voltage on V_{T} by $V_{\mathrm{T}}^{\mathrm{eff}} = V_{\mathrm{T}} + V_{\mathrm{DS}}/2$ [79]. In addition, the method is suitable not only for a transistor consisting of a crystalline semiconductor that exhibits perfectly linear

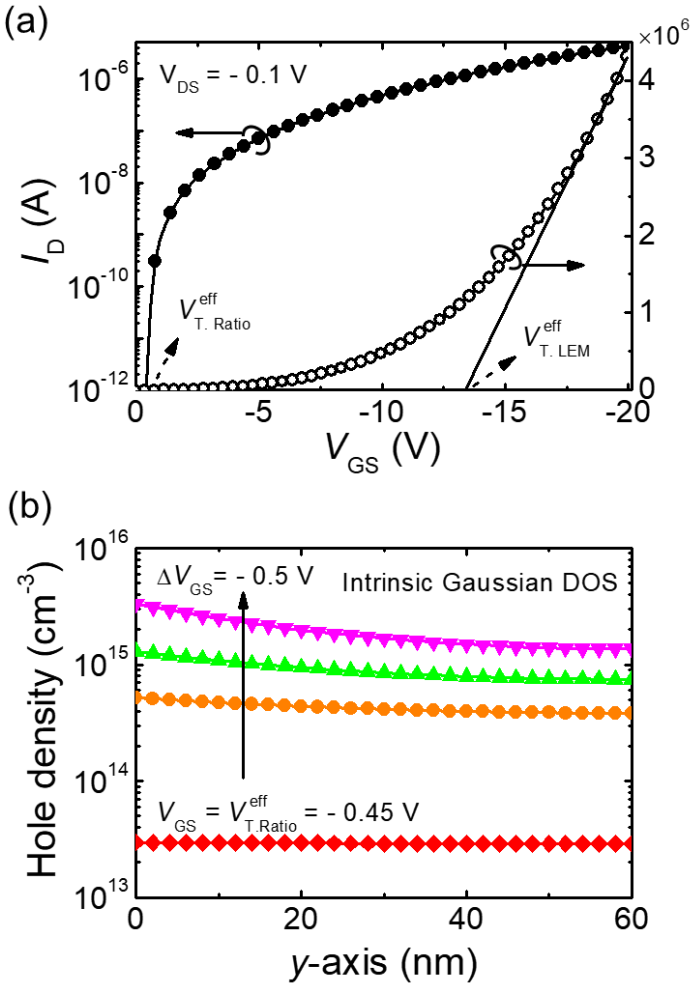

Fig. 4.1. (a) Simulated transfer characteristic and extracted V_T^{eff} by both ratio and linear extrapolation methods. (b) Calculated hole density along the *y*-direction at the center of channel.

transfer characteristics but also for a transistor consisting of a semiconductor with disorder or traps that exhibits a superlinear or a sublinear transfer characteristics due to V_{GS}-dependent mobility and contact resistance by power law.

The transfer curve was simulated assuming only the single Gaussian DOS and that there are no extrinsic traps and interface charges (Fig. 4.1a). The simulation used parameters (Table 4.1) that are typical of this type of device. The value of V_T^{eff} extracted by the ratio method ($V_{T.Ratio}^{eff} = -0.45\ V$) was significantly smaller than that extracted by the linear extrapolation method (LEM) ($V_{T.LEM}^{eff} = -13.1\ V$). The drain current I_D was ~10^{-12} A at $V_{GS} = V_{T.Ratio}^{eff}$ and the drain current exponentially increased around $V_{T.Ratio}^{eff}$, whereas I_D was ~10^{-6} A at

Table 4.1. List of parameters for the numerical simulation.

Categories	Parameters	Values
Source/Drain electrode	Work function $W_{S/D}$	4.9 eV
Insulator	Dielectric constant ε_i	2.5
Organic semiconductor	Dielectric constant ε_s	4
	Total molecular density N_i	3×10^{21} cm^{-3}
	Gaussian disorder σ_i	0.2 eV
	Injection barrier E_b	1.0 eV
	Zero-carrier mobility $\mu_0(T = 300\ \text{K})$	3×10^{-3} cm^2/V·s
Donor-like bulk trap	Total trap density N_d	1×10^{15} cm^{-3}
	Gaussian width σ_d	0.2 eV
	Energy difference E_d	Variable

$V_{GS} = V_{T.LEM}^{eff}$ which suggests that the transistor is already turned on (Fig. 4.1a). Many researchers adopt the LEM to extract V_T^{eff}, but this method is not applicable for OFETs due to non-linear transfer characteristics [117]. Because most of OFETs show non-linear transfer curves, $V_{T.Ratio}^{eff}$ is a more appropriate parameter than $V_{T.LEM}^{eff}$ for the analysis of the threshold behavior of OFETs.

4.1.2 Physical origin of threshold voltage

The simulated hole carrier density profile across the channel at the center of the channel (Fig. 4.1b) as well as pseudo three-dimensional (3D) plots of hole density (Fig. 4.2) near $V_{T.Ratio}^{eff}$ illustrates the channel-formation process by accumulation and provides a physical meaning to the value of V_T^{eff}. The hole carrier density profile across the channel (i.e. along the *y* direction) was simulated considering a Gaussian DOS with $\sigma_i = 0.2$ eV at V_{GS} = -0.45 V ($V_{T.Ratio}^{eff}$), -0.95 V, -1.45 V and -1.95 V. When $V_{GS} = V_{T.Ratio}^{eff}$, the carrier density was constant all along the y-direction (Fig. 4.1b). This clearly shows that there is no preferential

accumulation of charge-carrier at the semiconductor-insulator interface at threshold. When $|V_{GS}| > |V_{T.Ratio}^{eff}|$, the carrier density became higher at the interface than the bulk. In addition, the hole density in the channel region was comparable to (Fig. 4.2b) or higher than (Fig. 4.2c and d) the source/drain region, establishing the conducting channel.

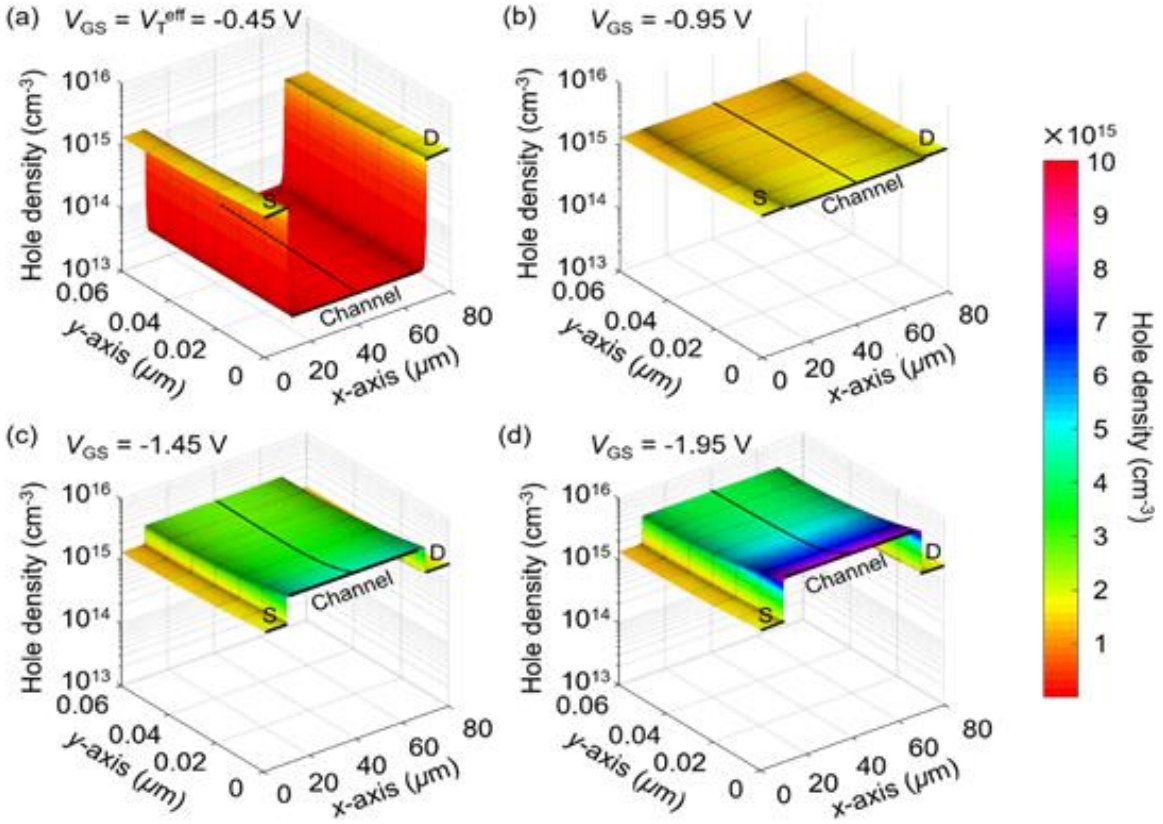

Fig. 4.2. 3D plot of hole density in semiconductor region for (a) V_{GS} = -0.45 V = V_T^{eff}, (b) -0.95 V, (c) -1.45 V and (d) -1.95 V. Each cutline represents a line to extract results of Fig. 3.1b. S: Source, D: Drain.

The surface charge density per unit area Q_S (Fig. 4.3a) and the surface potential V_S (Fig. 4.3b) near V_T^{eff} provide a consistent physical meaning to V_T^{eff}. Q_S was obtained by integrating the hole density along the y-axis (Fig. 4.1b) and by multiplying by the elementary charge. Before V_{GS} reaches V_T^{eff}, Q_S increased exponentially but still negligible in quantity due to a weak accumulation. Therefore, $V_{GS} \approx V_S$ because the voltage across the insulator $V_i \approx 0$ ($V_i = Q_S/C_i$ and $V_{GS} = V_i + V_S$ where $C_i = \varepsilon_i\varepsilon_0/d_i$ [F · cm^{-2}] is the

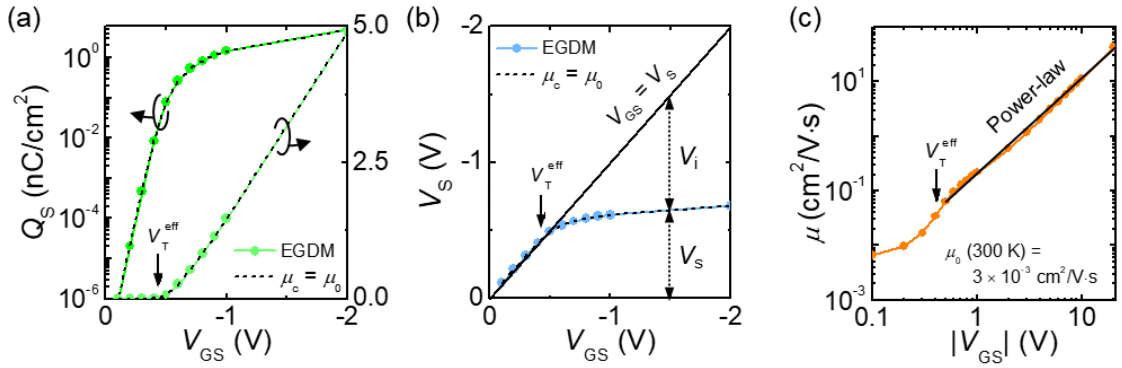

Fig. 4.3. (a) The surface charge density per unit area (b) and the surface potential at the interface with insulator $(y = 0)$ EGDM (filled symbol and line) and constant mobility (dotted line) were assumed in the calculation. (c) Calculated mobility by EGDM. The mobility exhibits the power-law dependence to V_{GS} for $|V_{GS}| > |V_T^{eff}|$.

areal gate insulator capacitance). This phenomenon originates from the initial position of the equilibrium Fermi level of the semiconductor. In intrinsic ODSs, the Fermi level is located near the middle of the band gap at which the energetic distance from HOMO edge is few eV. Therefore, Q_S is negligible and $V_{GS} \approx V_S$ before the Fermi level reaches the edge of HOMO. When $|V_{GS}| > |V_{T.Ratio}^{eff}|$, charge density rose exponentially and more abruptly indicating a strong accumulation. In this regime, $V_{GS} \approx V_i$ because V_S was saturated and $V_i \gg V_S$. Therefore, we can define V_T^{eff} as the voltage at which Q_S starts to rise exponentially and this result supports the hypothesis that the origin of V_T^{eff} is a channel threshold by charge accumulation. Moreover, calculated Q_S and V_S under both variable (EGDM) and constant mobility were identical. This result convinces that the channel formation by Q_S is not controlled by the mobility.

To validated $V_{T.Ratio}^{eff}$ in OFET device, the field-effect mobility (Fig. 4.3c) was calculated using the EGDM [84]. In general, the carrier mobility increases monotonically throughout the entire regime, and shows a power-law dependence on V_{GS} for $|V_{GS}| \geq |V_T^{eff}|$ in agreement with what observed for various OFETs [118], [119]. This was attributed to the disorder in the semiconductor layer. The power-law carrier mobility was initially explained for a transistor with exponential DOS by using an analytical approach [25]. The validity of the power-law dependence was further extended to a transistor with Gaussian DOS for a practical range of operation voltage [6]. The appearance of power-law

dependence for $|V_{GS}| \geq |V_T^{eff}|$ is evidence that the conducting channel is well formed. This inference reinforces the correlation between the definition of V_T (as the gate voltage at which Q_S starts to appear in the semiconductor) and the physical meaning of V_T (at which the channel is created).

Lastly, V_T^{eff} by the ratio method is comparable with the turn-on voltage V_0 that commonly defined as a crossover of a current threshold in the logarithm scale [74], [75], [120]. V_0 is an alternative parameters of the V_T because classical V_T extraction methods [72] such as LEM [75] and $\sqrt{I_{DS}}$ method [74] were not successful for OFETs. In our calculation, V_T^{eff} was similar with V_0 (crossover of a current threshold at $I_{DS} = 10^{-12}$ A) because the physical origin of both parameters are identical as the voltage where the preferential accumulation of charge carrier starts [75]. However, because V_0 is highly depending on an off-current level in the real, the reliable extraction of V_0 is vulnerable to the property of the gate dielectric and the amount of trap states [121]. In contrast, $V_{T.Ratio}^{eff}$ is only determined by the energetic structure and the accumulation not by the off-current level so that $V_{T.Ratio}^{eff}$ is more reliable parameter than V_0.

4.1.3 Effect of Gaussian width

In this section, we examine the effect of Gaussian width on the threshold voltage. We fixed the energetic distance between Fermi level E_F and $HOMO_{onset}$ as 1.2 eV and varied $\sigma = 0.05,\ 0.1, 0.15$ and 0.2 eV (Fig. 4.4a) where $HOMO_{onset} = HOMO_{max} + 2\sigma$. Calculated transfer characteristics with various σ is normalized to maximum of each drain current (Fig. 4.4b). Through the ratio method, extracted V_T^{eff} decreased when σ decreased; $V_T^{eff} = -0.86, -0.81, -0.69$ and -0.45 V for $\sigma = 0.05,\ 0.1,\ 0.15$ and 0.2 eV.

Extracted V_T^{eff} values reduced because of the deep tail states of Gaussian DOS. When σ increased, Gaussian broadening is significant and tail states deeply penetrate toward E_F. Therefore, the energetic distance between the initial position of the equilibrium Fermi level (middle of bandgap) and the band edge reduce. As aforementioned explain in Fig. 4.3, this energetic distance is origin of V_T^{eff} under the intrinsic condition, Gaussian width affects on V_T^{eff}.

Also, the discrepancy between the ratio method and the LEM decreased when σ decreased because non-linear transfer characteristics disappeared gradually. Linearity of transfer curve depends on the gate-voltage dependent mobility that is almost zero at low Gaussian width, e.g. σ=0.05 eV. Therefore, the validity of LEM relies on the Gaussian width.

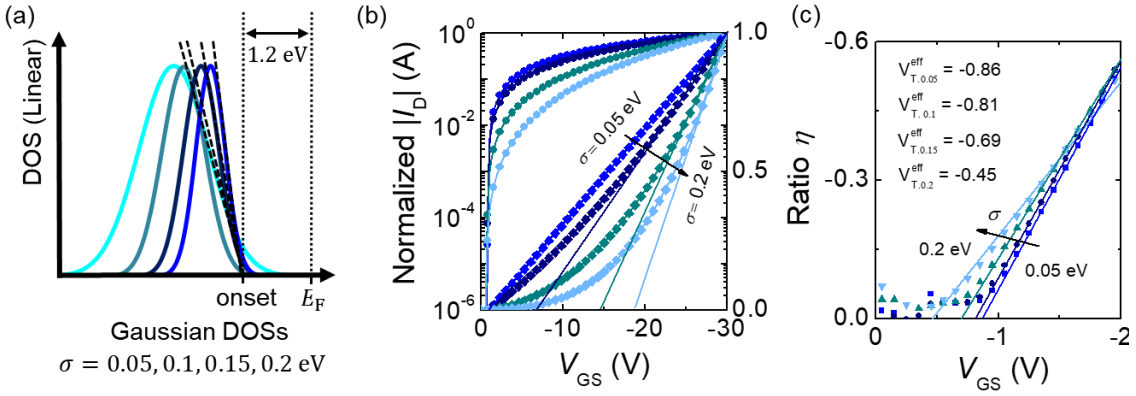

Fig. 4.4. (a) Schematic of Gaussian DOS with various $\sigma = 0.05, 0.1, 0.15$ and 0.2 eV. Energetic distance between Fermi level and $\mathrm{HOMO_{onset}}$ is fixed to 1.2 eV. (b) Simulated transfer characteristics with various σ and (c) ratio method to extract V_T^{eff}.

4.1.4 Fixes charges

In FETs, fixed charges Q_F can be generated unintentionally at the insulator-semiconductor interface during fabrication (Fig. 4.5a) [71]. The presence of the fixed charges leads to band bending, which requires application of additional V_{GS} to flatten the band and causes a shift in V_T^{eff}. Many researchers adopted this concept to account for the threshold behavior of OFETs [122]–[124]. In this section, we present the effect of the fixed charge on V_T^{eff} in OFETs under the intrinsic Gaussian DOS by systematic numerical simulation and analytical interpretation.

The transfer curves were calculated for Q_F = 0, 1×10^{10}, 5×10^{10} and 1×10^{11} cm^{-2} (Fig. 4.5b) using parameters in Table 4.1. V_T^{eff} for each transfer characteristic was then determined using the ratio method (Fig. 4.5c). V_T^{eff} increases linearly with Q_F and this behavior can be modelled as

$$V_{\mathrm{T}}^{\mathrm{eff}} = q \cdot Q_{\mathrm{F}}/C_{\mathrm{i}}. \tag{4.2}$$

The slope extracted from Fig. 4.5c (4.35×10^{-11} C/(F·cm^{-2})) is almost identical to that calculated from C_{i} (4.34×10^{-11} C/(F·cm^{-2})). The values of sub-threshold swing were SS = 84 mV/dec for all Q_{F} values. In addition, when simulated transfer curves and mobility by EGDM were plotted with respect to the $|V_{\mathrm{GS}} - V_{\mathrm{T}}^{\mathrm{eff}}|$ (Fig. 4.5d and e) instead of V_{GS}, curves overlapped to a perfect single curve for various Q_{F}. This means, interestingly, that the presence and the variation of Q_{F} affects only the threshold behavior and does not affect other transistor parameters; a previous paper reported the same conclusion [107].

As Q_{F} does not affect electrical characteristic of OFETs, the origin of $V_{\mathrm{T}}^{\mathrm{eff}}$ with Q_{F} should be same as the channel threshold despite their large values. As can be anticipated by Fig. 4.3a, Q_{s} was insignificant for $|V_{\mathrm{GS}}| < |V_{\mathrm{T}}^{\mathrm{eff}}|$ and increased abruptly from the threshold (Fig. 4.5f). $V_{\mathrm{T}}^{\mathrm{eff}}$ where Q_{s} starts to be

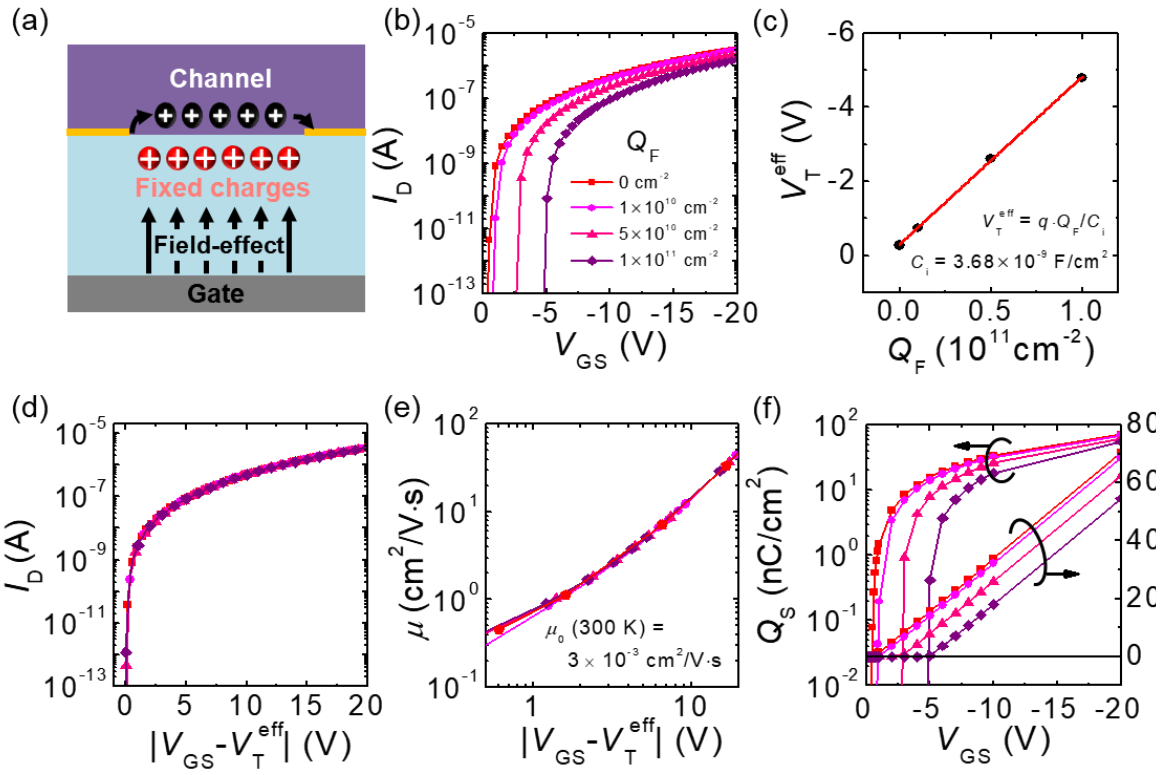

Fig. 4.5. (a) Schematic of fixed charges in the OFET device. (b) Simulated transfer curves and (c) extracted $V_{\mathrm{T}}^{\mathrm{eff}}$ by ratio method for various Q_{F}. (d) Plotted transfer curves and (e) charge carrier mobility with respect to $|V_{\mathrm{GS}} - V_{\mathrm{T}}^{\mathrm{eff}}|$. (f) Extracted Q_{S} for each Q_{F}.

accumulated followed the prediction of Eq. (4.2) while slopes of Q_s were identical for various Q_F; it is proved again that Q_F affects only the threshold behavior of the device. Here, Q_F delays the channel formation because positive fixed charges behave as positive gate bias [71] and they screen the semiconductor layer from the field-effect.

Although the threshold behavior of OFETs with Q_F and its analytical relation in Eq. (4.2) are equivalent to those in MOSFETs, its physical understanding should be differed. In MOSFETs, an additional voltage is necessary to flatten the band because Q_F induces the unexpected charges and band bending. However, the absence of charge density at below threshold in OFETs $(Q_s \approx 0)$, neither the hole nor the electron, signifies that there is no band bending by Q_F. This phenomenon originates from the full depletion of unintentionally-doped organic semiconductor in OFETs at variance with MOSFETs [125]. At full depletion condition, there are no electrons ionized from dopant molecules or injected from the contact because of a high electron injection barrier. Therefore, an additional voltage is necessary by Q_F to alleviate its screening effect on the semiconductor and to form the channel in OFETs.

4.2 Effect of double Gaussian density of states

4.2.1 Charge trapping and threshold voltage

The charge trapping in the extrinsic trap states have been regarded as a key factor that modifies V_T^{eff} [97]. These states could originate from impurity guest molecules [126] or chemical reactions with oxygen or moisture [127], [128]. In this section, we study the mechanism of the charge trapping into the secondary Gaussian trap DOS and concomitant threshold behavior by the double Gaussian DOS model [96]. For secondary Gaussian trap DOS, we consider donor-like trap states because they trap charge carriers in *p*-type OFETs, whereas acceptor-like trap states give additional charge carriers as a dopant. In addition, surface termination of organic semiconductor merely induces interface traps due to the weak intermolecular bonding of ODS [97] so the trap effect on V_T^{eff} is attributed only to the bulk trap states. The double Gaussian DOS model is different from a previous model that used trap states that had a single energy level [129]. The total density of trap states N_d and the distance between the trap states and the intrinsic

DOS E_{d} are independent of each other in the single-energy level model, but they are correlated in the double-Gaussian DOS model. For the double-Gaussian DOS model, if E_{d} decreases, then the tail of the trap Gaussian DOS merges with the intrinsic Gaussian DOS and the trapped charge density p_{trap} decreases. If E_{d} increases, the DOSs separate and p_{trap} increases.

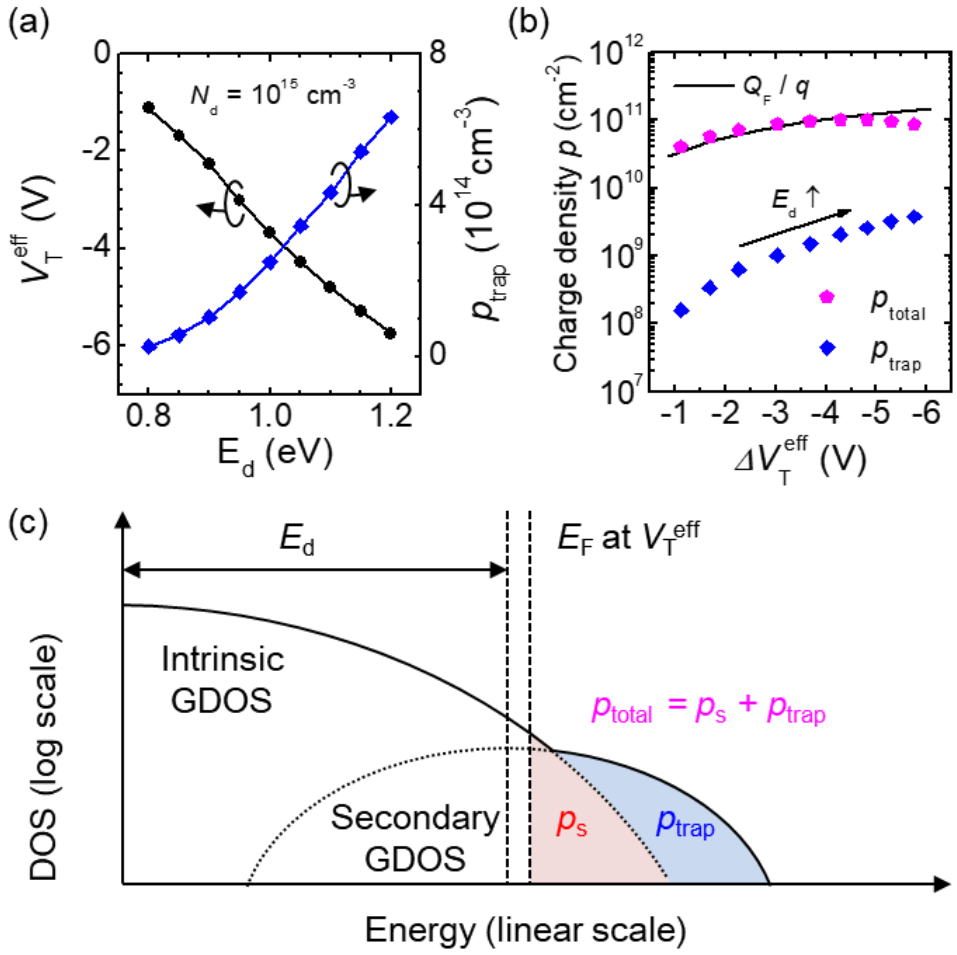

Fig. 4.6. (a) $V_{\mathrm{T}}^{\mathrm{eff}}$ extracted by ratio method (black) and p_{trap} (blue) with respect to various E_{d}. (b) Areal charge density of the fixed charge at the insulator Q_{F}/q (solid) and filled in double Gaussian DOS at each $\Delta V_{\mathrm{T}}^{\mathrm{eff}}$. p_{total} considers both intrinsic and secondary DOS and p_{trap} considers only un-overlapped secondary DOS. (c) Schematic of the double Gaussian DOS at $V_{\mathrm{GS}} = V_{\mathrm{T}}^{\mathrm{eff}}$.

In our calculation, when E_{d} increased from 0.8 eV to 1.2 eV, $V_{\mathrm{T}}^{\mathrm{eff}}$ extracted by the ratio method from simulated transfer curves decreased monotonically because p_{trap} increased due to the separation of two Gaussian DOSs (Fig. 4.6a). In particular, it was not p_{trap} but p_{total}, which is defined as the sum of p_{trap} and space charge density p_{s} in the intrinsic Gaussian DOS, that led to the same amount of threshold voltage shift $\Delta V_{\mathrm{T}}^{\mathrm{eff}}$ as Q_{F} does (Fig. 4.6b). The threshold voltage shift resulting from fixed interface charge abides by $V_{\mathrm{T}}^{\mathrm{eff}} = qQ_{\mathrm{F}}/C_{\mathrm{i}}$ (Fig. 4.5c). Electrostatically, the same $\Delta V_{\mathrm{T}}^{\mathrm{eff}}$ is expected regardless of the origin of charge. Therefore, it can be inferred that the charge carriers are filling the intrinsic and secondary Gaussian trap DOS simultaneously (Fig. 4.6c). Note that these charges reside at $E \geq E_{\mathrm{F}}(V_{\mathrm{T}}^{\mathrm{eff}})$ dominantly manifest the subthreshold and near-threshold current. The double Gaussian DOS model is different from the previous model consisting of band-like intrinsic DOS and single level or uniform trap states [129] in that the depth and the total trap density can be tailored.

The simultaneous charge filling in the double Gaussian DOS makes a difference in transfer characteristics. When transfer curves were calculated with the secondary Gaussian trap DOS with various E_{d} (Fig. 4.7a), the trap states led to the hump effect while $V_{\mathrm{T}}^{\mathrm{eff}}$ shifted negatively. By ratio method (Fig. 4.7b), $V_{\mathrm{T}}^{\mathrm{eff}}$ varied from -0.45 V, -2.54V, -3.7V and -4.7 V and γ varied from 1.91, 1.99, 2.02 and 2.04 (Fig. 4.7c). The subthreshold swing *SS* increased from 0.084 V/dec to 2.1, 2.3, 2.4 V/dec for the trap-free, $E_{\mathrm{d}} = 0.9, 1.0$ and 1.1 eV. This result is at variance with the presence of Q_{F} in Fig. 4.5 that any hump effect was not found in calculated transfer characteristics with various Q_{F} and *SS* were almost identical for all Q_{F}. This behavior can be understood by calculated Q_{S} (Fig. 4.7d) and E_{F} (Fig. 4.7e) with various condition. The Fermi levels from the maximum energy of the HOMO were extracted by the Gauss-Fermi integral by the mean hole density across the center of the channel (x = L/2). With the secondary Gaussian trap DOS, the rise of Q_{S} and E_{F} delayed when E_{d} increased, similar with the hump effect in transfer curves. Because Q_{S} and E_{F} only accounted for the mobile charge density in the intrinsic Gaussian DOS, this illustrates that the

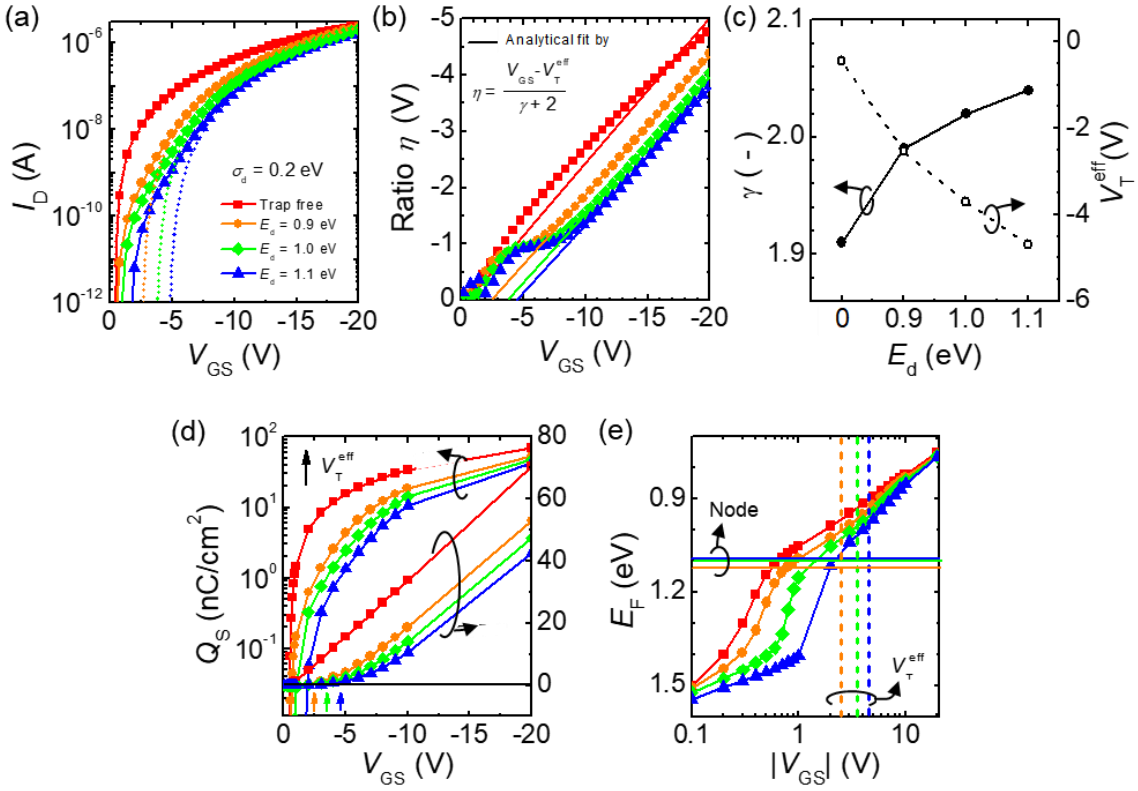

Fig. 4.7. Calculated (a) transfer curves, (b) ratio method, (c) extracted $V_{\mathrm{T}}^{\mathrm{eff}}$ and γ (d) Q_{s}, (e) Fermi level E_{F} with various E_{d} value for $\sigma_{\mathrm{d}} = 0.2$ eV. In (a), voltages where dotted lines meet x-axis indicate $V_{\mathrm{T}}^{\mathrm{eff}}$ extracted using the ratio method.

accumulation of mobile charge reduced at $|V_{\mathrm{GS}}| < |V_{\mathrm{T}}^{\mathrm{eff}}|$ due to the division of charge filling in two DOSs. If the charge carriers start to fill in the intrinsic DOS after they populate all trap states completely, Q_{S} and E_{F} would have not rise at $|V_{\mathrm{GS}}| < |V_{\mathrm{T}}^{\mathrm{eff}}|$ and there would have been no hump effect.

In addition, the physical meaning of $V_{\mathrm{T}}^{\mathrm{eff}}$ under the presence of extrinsic trap states can be comprehended by p_{trap}. We numerically calculated the trapped charge density with respect to the E_{F}, $p_{\mathrm{trap}}(E_{\mathrm{F}})$, and it was aligned with the double Gaussian DOS (Fig. 4.8a). When E_{F} decreased toward $\mathrm{HOMO}_{\mathrm{max}}$ ($E_{\mathrm{F}} = 0$ eV) at T=300 K, $p_{\mathrm{trap}}(E_{\mathrm{F}})$ for each E_{d} gradually increased and finally saturated at E_{F} of $V_{\mathrm{GS}} = V_{\mathrm{T}}^{\mathrm{eff}}$. That is to say, the energy that trap states were totally filled indicates E_{F} of $V_{\mathrm{T}}^{\mathrm{eff}}$, not $E_{\mathrm{F}} = E_{\mathrm{node}}$ where trap DOS is completely absorbed into the intrinsic DOS. This originated from the distribution of the Fermi-Dirac statistics. The Fermi-Dirac distribution is a perfect step

function at T=0 K, whereas the distribution is a gradual curve at T=300 K due to the thermally generated charges. Thus, E_{F} should move closer to $\mathrm{HOMO}_{\mathrm{max}}$ at 300 K than 0 K to finish the trap filling process. (Fig. 4.8b). The fact that $p_{\mathrm{trap}}(E_{\mathrm{F}})$ saturated at $E_{\mathrm{F}} = E_{\mathrm{node}}$ for T=0 K can support this argument.

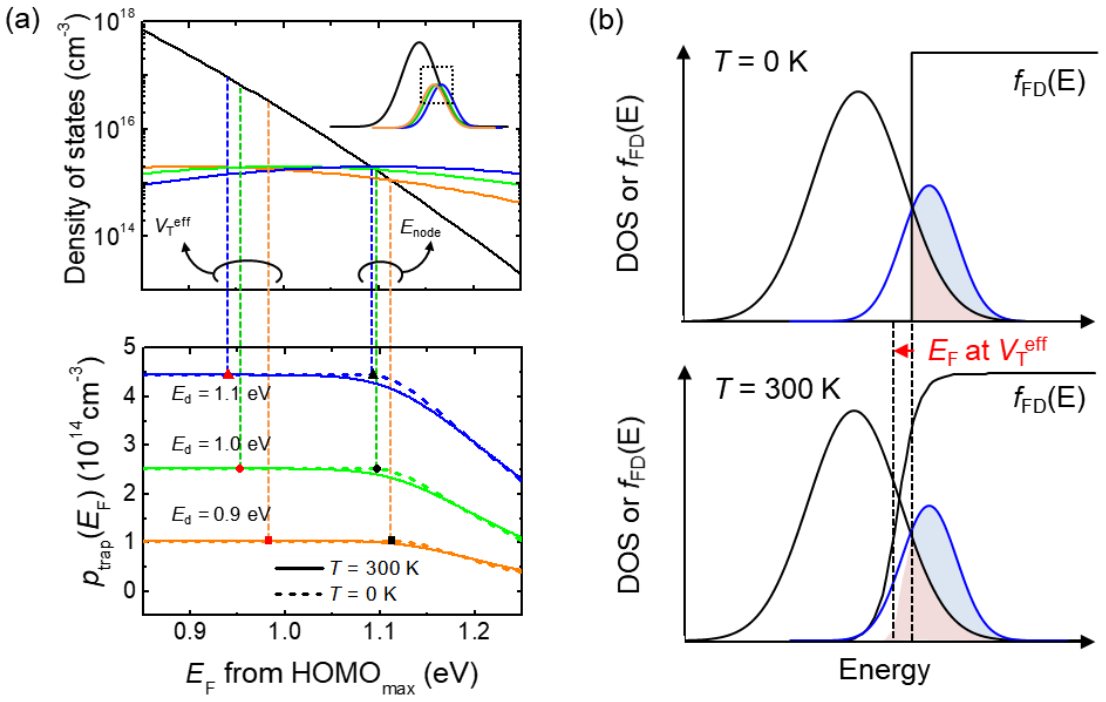

Fig. 4.8. (a) Calculated double Gaussian DOS near the $V_{\mathrm{T}}^{\mathrm{eff}}$ and E_{node}. E_{F} at $V_{\mathrm{T}}^{\mathrm{eff}}$ for each E_{d} corresponded with E_{F} that trap states were totally filled ($p_{\mathrm{trap}}(E_{\mathrm{F}})$ was saturated) at T=300 K (red symbols). E_{node} corresponded with E_{F} that trap states were totally filled at T=0 K (black symbols). (b) Schematic of double Gaussian DOS and Fermi-dirac distribution for both T=0 K and 300 K.

4.2.2 Effects on the power-law mobility

It is more practical to extract mobility μ than Q_{S} and E_{F} to study the threshold behavior because the mobility can be easily extracted and reflected the behavior of Q_{S} and E_{F} (Fig. 4.9a). Especially, the entire shape of μ versus V_{GS} is similar with E_{F} versus V_{GS} because the field-effect mobility is highly depending on the mobile charge density. At the $|V_{\mathrm{GS}}| < |V_{\mathrm{T}}^{\mathrm{eff}}|$ the rise of mobility was delayed with deep trap states by large E_{d}; mobile charges were

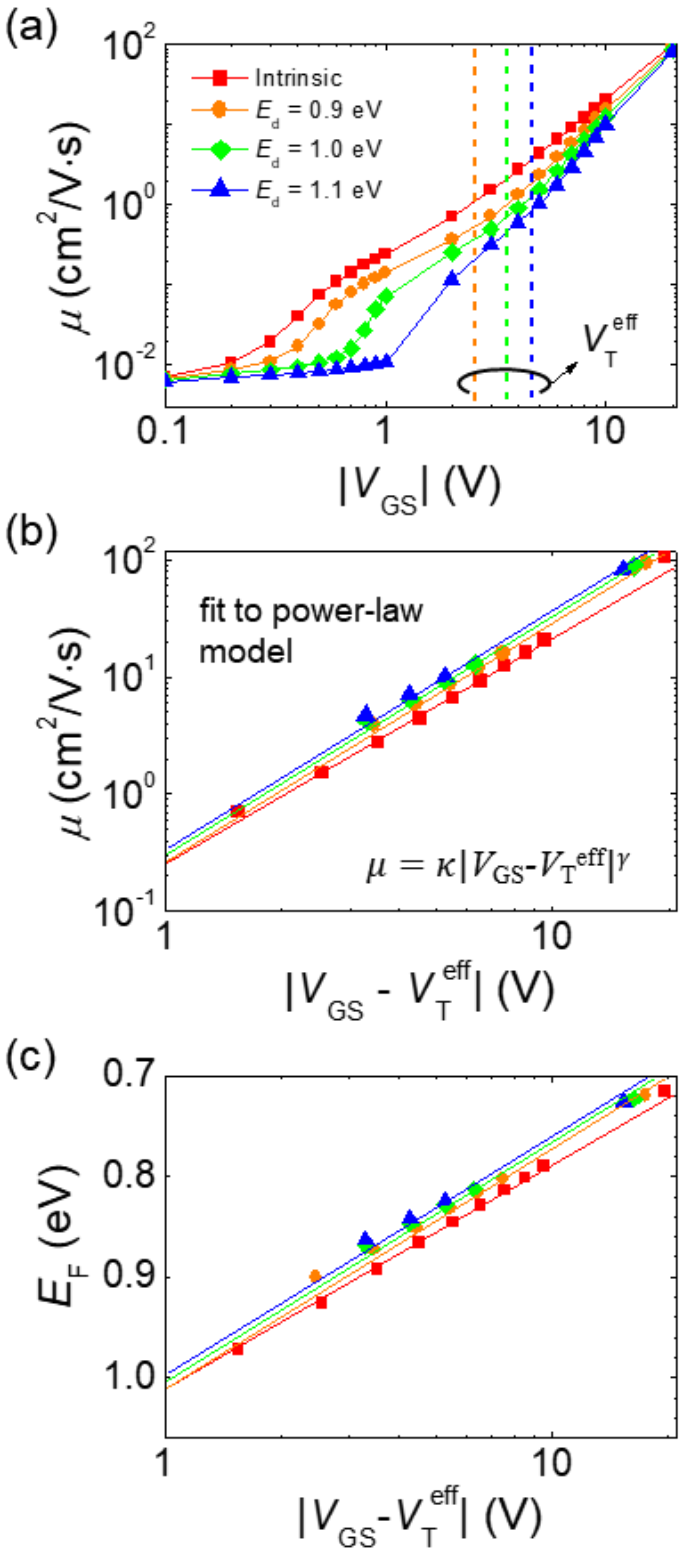

Fig. 4.9 Calculated field-effect mobility and Fermi level with respect to (a) V_{GS} and (b), (c) $\left|V_{\mathrm{GS}} - V_{\mathrm{T}}^{\mathrm{eff}}\right|$ with various E_{d} values. In (a), vertical dot lines illustrate $V_{\mathrm{T}}^{\mathrm{eff}}$.

almost depleted due to the charge trapping. At $|V_{GS}| \geq |V_T^{eff}|$, each mobility showed a power-law dependency; the channel was formed by charge carrier accumulation.

In addition, the magnitude of the mobility is an extractable evidence of the simultaneous charge filling mechanism into the double Gaussian DOS. When E_d increased, the power-law mobility plotted with respect to the $|V_{GS} - V_T^{eff}|$ exhibited high magnitude (Fig. 4.9b) consequent upon the same tendency of extracted E_F (Fig. 4.9c). This result originated from the position of $E_F(V_T^{eff})$ in the double Gaussian DOS (Fig. 4.10). Because the complete trap DOS filling is the physical origin of V_T^{eff} under the double Gaussian DOS, $E_F(V_T^{eff})$ is determined by a constant energetic shift from E_{node} to compensate the gradual curve of the Fermi- Dirac distribution at T=300 K. Therefore $E_F(V_T^{eff})$ moved toward $HOMO_{max}$ with increased E_d following the shift of E_{node}. If the carriers fill the trap DOS and the intrinsic DOS sequentially and separately, $E_F(V_T^{eff})$ for various E_d would be invariable because mobile charge carriers would not exist in the intrinsic DOS before trap DOS is completely filled at $V_{GS} = V_T^{eff}$. The overlapped transfer characteristics and power-law mobility plots with respect to $|V_{GS} - V_T^{eff}|$ for various Q_F can support this statement because Q_F did not affect on the charge accumulation in the intrinsic DOS (Fig 4.5).

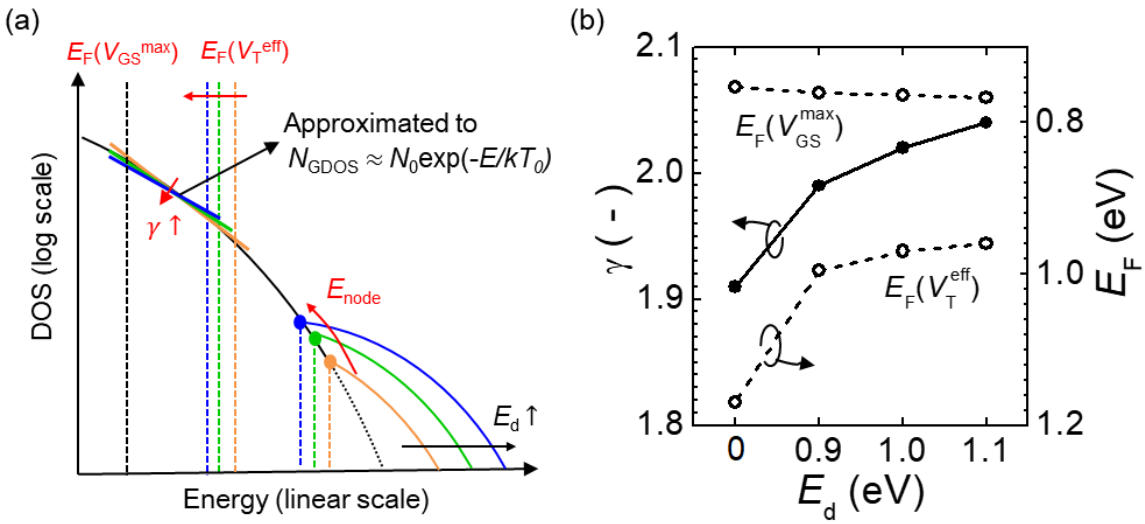

Fig. 4.10. (a) Schematic of double Gaussian DOS with various E_d. (b) Variation of γ, E_F at V_{GS}^{max} and E_F at V_T^{eff} with respect to E_d. Exponential DOS model can be approximated in Gaussian DOS model within V_{GS} operating regime.

The magnitude of mobility provides additional information on the effect of the secondary Gaussian trap DOS. At low gate voltage limit, the mobility asymptote is about $6 \times 10^{-3}\ \mathrm{cm^2/V \cdot s}$ that is slightly higher than the zero-carrier mobility $\mu_0(T = 300\ \mathrm{K}) = 3 \times 10^{-3}\ \mathrm{cm^2/V \cdot s}$ (Fig. 4.9a). This discrepancy accounts for a small amount of charges existing in the intrinsic DOS due to simultaneous charge filling. It can be inferred that, despite the simultaneous filling, a majority of carriers fills secondary Gaussian DOS and get trapped at very low gate voltage (0.1 ~ 1V for different E_d). At near-threshold voltage ($V_\mathrm{GS} \lesssim V_\mathrm{T}^\mathrm{eff}$), on the other hand a significant portion of carriers fill the intrinsic Gaussian DOSs and be subject to hopping transport.

The presence of the secondary Gaussian trap DOS alters the power-law exponent γ as well as the magnitude of mobility (Fig. 4.10b). The extracted γ by the ratio method increased when E_d increased. From a direct numerical calculation of E_F, as E_d increases, $E_\mathrm{F}(V_\mathrm{T}^\mathrm{eff})$ moves toward $\mathrm{HOMO_{max}}$ while $E_\mathrm{F}(V_\mathrm{GS}^\mathrm{max})$ was relatively invariable; Calculated $E_\mathrm{F}(V_\mathrm{T}^\mathrm{eff})$ were 1.17, 0.98, 0.953, 0.94 eV and calculated $\mathrm{E_F(V_{GS}^{max})}$ were almost identical as 0.715, 0.719, 0.722 and 0.725 eV for intrinsic, $E_\mathrm{d} = 0.9, 1.0$ and 1.1 eV, respectively. The operating range between $V_\mathrm{T}^\mathrm{eff}$ and $V_\mathrm{GS}^\mathrm{max}$ reduces in energy scale. Therefore, when E_d increased, the tangent of the approximated exponential DOS decreased and γ increased with T_0 because $\gamma = T_0/T - 1$ where T_0 is the characteristic temperature of the approximated exponential DOS to the intrinsic Gaussian DOS. (Fig. 4.10a)

4.2.3 Experimental validation

In this section, we validate the effect of charge trapping in the double Gaussian DOS on the threshold behavior by the numerical fitting to experimental data. We fabricated bottom-gate top-contact ink-jet printed OFETs with Tips-pentacene and 4 different soluble polyimides gate dielectric, DOCDA-DABC, DOCDA-MDA, 6FDA-DABC and 6FDA-MDA (Fig. 4.11 and more details on Appendix) [130]. We observed that chemical engineering of block copolymer gate insulators enables improvement of the characteristics of bottom gate transistors (symbols in Fig. 4.12 a and b). A plausible explanation was unsatisfactory in that, regardless of different dielectric conditions, we obtained an excellent smoothness from the

AFM image of the gate insulator layers as well as well-oriented millimeter-scale domains from polarized microscopy and no obvious difference in diffractogram peaks along the out-of-plane GIWAXS pattern of the Tips-pentacene layer [130]. A comparative analysis between the measured and simulated device characteristics could provide a more direct explanation on structure-performance relationship.

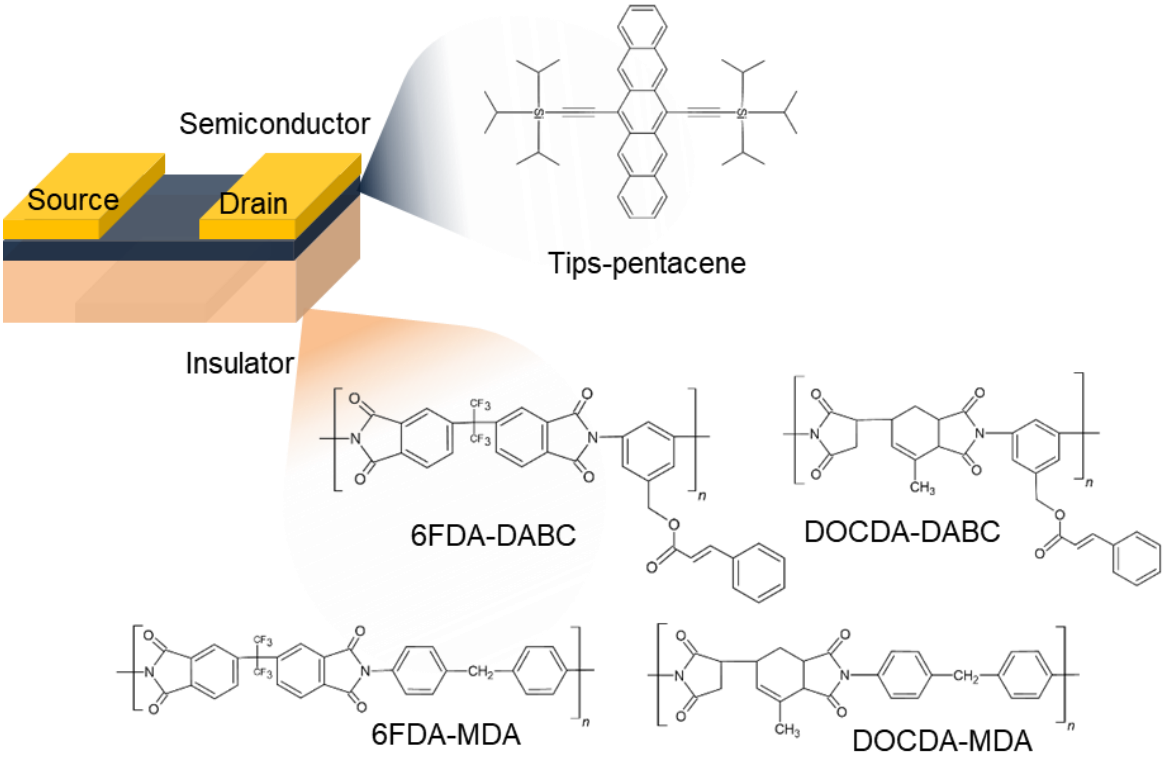

Fig. 4.11. Schematic of ink-jet fabricated OFETs with Tips-pentacene as a semiconductor layer and 4 soluble polyimide gate-dielectrics, 6FDA-DABC, 6FDA-MDA, DOCDA-DABC and DOCDA-MDA.

To fit the experimental data, we grouped four OFETs into two categories: two OFETs with 6FDA-based polyimides and two OFETs with DOCDA-based polyimides. The polyimides with MDA monomers in each group made $V_{\mathrm{T}}^{\mathrm{eff}}$ shift more negatively than those with DABC monomers while they maintained above-threshold behavior. Because the subthreshold swing changed in each group, the numerical fitting by the double Gaussian DOS is more adequate than by Q_{F} to analyze threshold behavior. Therefore, we assumed the OFETs with MDA-based gate insulator has the deep secondary Gaussian bulk trap DOS with large E_{d}.

Here, we did not consider the interface trap states because the surface roughness and the surface energy showed similar values regardless of materials [130] so that the effect semiconductor-insulator properties were weak. In addition, polyimides with MDA monomer showed a clear hysteresis in transfer curves [130] that commonly originated from the charge trapping in deep bulk trap states [102], [131]; This justifies OFETs with MDA-based polyimides has the deep bulk trap states.

Experimentally measured transfer curves were successfully fitted by simulated transfer curves by adjusting only E_{d} in the double Gaussian DOS (Fig. 4.12a, b). Parameters that used in the simulation are listed in Table 4.2 for OFETs with 6FDA-based gate insulators and in Table 4.3 for OFETs with DOCDA-based gate insulators. For each group, fitting parameters were identical except for the E_{d}. Because the gate insulator with MDA monomer induced more negative $\Delta V_{\mathrm{T}}^{\mathrm{eff}}$, fitted E_{d} increased from 0.34 eV (6FDA-DABC) to 0.5 eV (6FDA-MDA) for 6FDA-based OFETs and from 0.4 eV (DOCDA-DABC) to 0.43 eV (DOCDA-MDA) for DOCDA-based OFETs. Also, $V_{\mathrm{T}}^{\mathrm{eff}}$ and γ were extracted by the ratio method from measured transfer curves (Fig. 4.12c and d). For 6FDA-based gate insulators, $V_{\mathrm{T}}^{\mathrm{eff}}$=1.45 V / γ=1.71 (6FDA-DABC) and $V_{\mathrm{T}}^{\mathrm{eff}}$=0.53 V / γ=1.89 (6FDA-MDA) were extracted. For DOCDA-based gate insulators, $V_{\mathrm{T}}^{\mathrm{eff}}$=-0.1 V / γ=1.461 (DOCDA-DABC) and $V_{\mathrm{T}}^{\mathrm{eff}}$=-0.35 V / γ=1.561 (DOCDA-MDA) were extracted.

The simultaneous charge filling mechanism in the double Gaussian DOS can be experimentally validated. When fitted E_{d} increased, extracted $V_{\mathrm{T}}^{\mathrm{eff}}$ and γ increased. From the direct calculation of E_{F} by numerical fitting, $E_{\mathrm{F}}(V_{\mathrm{T}}^{\mathrm{eff}})$ moved toward $\mathrm{HOMO}_{\mathrm{max}}$ at large E_{d} while $E_{\mathrm{F}}(V_{\mathrm{GS}}^{\mathrm{max}})$ was relatively invariable (Fig. 4.12e and f). Therefore, the operating regime between $V_{\mathrm{T}}^{\mathrm{eff}}$ and $V_{\mathrm{GS}}^{\mathrm{max}}$ reduced with the deep trap DOS so that γ increased with E_{d}. This result is exactly corresponding with the aforementioned numerical prediction.

The variation of $V_{\mathrm{T}}^{\mathrm{eff}}$ and γ in each group was proportional to the variation of E_{d}; $\Delta E_{\mathrm{d}} = 0.16$ eV accounted for $\Delta V_{\mathrm{T}}^{\mathrm{eff}} = -0.92$ V and $\Delta\gamma = 0.19$ for 6FDA-based group and $\Delta E_{\mathrm{d}} = 0.03$ eV accounted for $\Delta V_{\mathrm{T}}^{\mathrm{eff}} = -0.25$ V $\Delta\gamma = 0.1$ for DOCDA-based group. That is to say, when the power-law exponent γ and $V_{\mathrm{T}}^{\mathrm{eff}}$ are increased, trap DOS becomes deeper. Also,

OFETs with 6FDA-based polyimides adopted relatively high $\mu_0(300\,\mathrm{K})$ than DOCDA-based polyimides and negative Q_F to shift overall transfer curves toward positive direction because fluorine atoms in the polyimides backbone increased the field-effect mobility and V_T^{eff} shift to positive voltage [132].

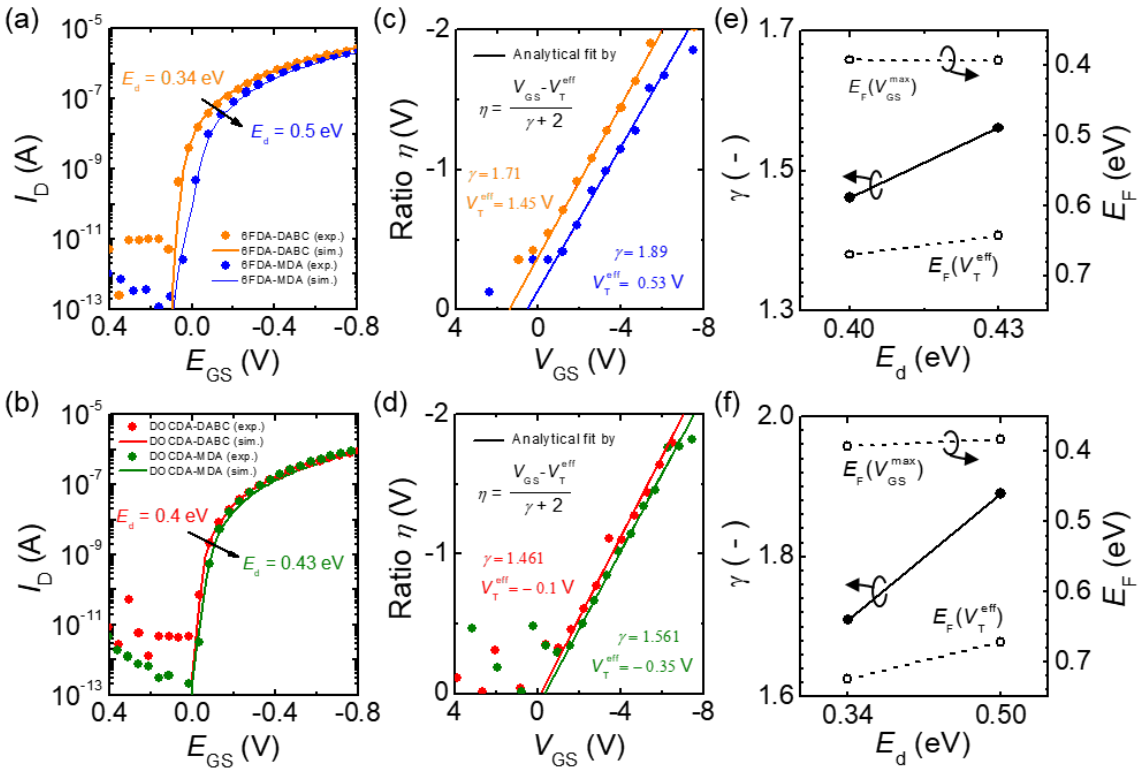

Fig. 4.12. Measured (dotted lines) and simulated (solid lines) transfer curves of Tips-pentacene based OFET with (a) 6FDA-DABC, 6FDA-MDA and (b) DOCDA-DABC, DOCDA-MDA as gate insulators. (c), (d) Calculated ratio with respect to V_{GS} from the measurements (dotted lines) and their analytical fits by Eq. (4.1) (solid lines) to extract γ and V_T^{eff}. (e) (f) Extracted γ from measurement and E_F at V_{GS}^{max} and V_T^{eff} from numerical simulation for E_d that used in the fitting in (a) and (b).

Table 4.2. List of parameters for the numerical fitting of 6FDA-based OFETs.

Categories	Parameters	Values
Source/Drain electrode	Work function $W_{S/D}$	4.9 eV
Organic semiconductor	Dielectric constant ε_s	3.6
	Total molecular density N_i	3×10^{21} cm^{-3}
	Gaussian disorder σ_i	0.1 eV
	Injection barrier E_b	0.3 eV
	Zero-carrier mobility $\mu_0(T = 300$ K)	4.56×10^{-2} cm^2/V · s
6FDA-DABC (Insulator)	Dielectric constant ε_i	3.16
	Dielectric thickness d_i	148 nm
	Fixed charge density Q_F	-1.5×10^{11} cm^{-2}
Bulk trap DOS	Total trap density N_d	1×10^{15} cm^{-3}
	Gaussian width σ_d	0.15 eV
	Energy difference E_d	0.34 eV
6FDA-MDA (Insulator)	Dielectric constant ε_i	2.88
	Dielectric thickness d_i	116 nm
	Fixed charge density Q_F	-1.5×10^{11} cm^{-2}
Bulk trap DOS	Total trap density N_d	1×10^{15} cm^{-3}
	Gaussian width σ_d	0.15 eV
	Energy difference E_d	0.5 eV

Table 4.3. List of parameters for the numerical fitting of DOCDA-based OFETs.

Categories	Parameters	Values
Source/Drain electrode	Work function $W_{S/D}$	4.9 eV
Organic semiconductor	Dielectric constant ε_s	3.6
	Total molecular density N_i	3×10^{21} cm^{-3}
	Gaussian disorder σ_i	0.1 eV
	Injection barrier E_b	0.3 eV
	Zero-carrier mobility $\mu_0(T = 300$ K)	2.15×10^{-2} cm^2/V · s
DOCDA-DABC (Insulator)	Dielectric constant ε_i	3.3
	Dielectric thickness d_i	126 nm
Bulk trap DOS	Total trap density N_d	1×10^{15} cm^{-3}
	Gaussian width σ_d	0.1 eV
	Energy difference E_d	0.4 eV
DOCDA-MDA (Insulator)	Dielectric constant ε_i	3.15
	Dielectric thickness d_i	120 nm
Bulk trap DOS	Total trap density N_d	1×10^{15} cm^{-3}
	Gaussian width σ_d	0.1 eV
	Energy difference E_d	0.43 eV

Chapter 5

Mobility modeling

In the device modelling, transport behavior of charge carriers in ODSs is the most important but challenging point because of different characteristics with the conventional inorganic counterpart; low mobility with dependency on the electric field, the temperature and the charge carrier concentration [82]. To understand this transport behavior, many researchers have developed the charge carrier mobility model based on Gaussian DOS. As an initial work, Bassler proposed the GDM [68]. The model stated that the charge carrier transport occurs via thermally-assisted hopping within randomly distributed localized states and it can explain the electric field and the temperature dependency of the hopping transport in ODSs. Pasveer and coworkers developed the GDM by adding additional charge carrier dependency of the mobility [84], so-called the EGDM. Today, the EGDM is the most widely accepted hopping transport model for ODSs and many commercial simulators provide this model for users [85], [86].

Although wide usage of the EGDM, several facts cannot guarantee an exact solution of the EGDM for transport behavior of ODSs. First, the initial parametrization of the EGDM yields too low mobility to describe transport of high mobility devices, i.e. organic field effect transistors (OFETs). For instance, the carrier mobility calculated by the EGDM shows $10^{-9} - 10^{-15}\ \mathrm{cm}^2/\mathrm{V}\cdot\mathrm{s}$ under typical parameters of the charge density, the Gaussian width and the electric field [84]. Such low mobility may be applicable for materials with low mobility and diode applications. In recent OFETs, however, the carrier mobility is very high because the material design has been remarkably improved [133] and OFETs exhibit commonly 3-4 orders of magnitude higher mobility than organic diodes thanks to the field effect [6]. Therefore, parameters in the model should be re-examined to describe proper transport behavior of OFETs.

Second, recent studies validated that EGDM cannot accurately describe the hopping transport of ODSs [134], [135]. They stated that localized states placed at the ordered lattice system (EGDM) and at the spatial disorder system (nature of ODSs) produce totally different transport behavior. While a Monte Carlo simulation proved that neglect of spatial disorder makes mobility increase, it can decrease in spatial disorder under the same parameter condition [134]. In addition, a critical parameter which determines electric field dependency of the carrier mobility is different between the lattice model and the spatial disorder model; An inter-site distance is responsible for the former, but a localization length is responsible for the latter.

Baranovskii and coworkers proposed a solution of the GDM in the spatial disorder by a transport energy [82], [87], [88] for any steeply energy-dependent DOS, i.e. the exponential DOS and the Gaussian DOS. At the low electric field, the mean time of upward hopping rate toward the transport energy from states below the transport energy determines the carrier mobility. At the high electric field, a concept of the effective temperature was adopted to describe charge transport [89], [90]. During the derivation of the GDM by Baranovskii, the model assumed consistently both spatial disorder and the variable-range hopping (VRH) that led a more precise result than previous GDMs.

In this study, we propose the physical parametrization of the GDM in the spatial disorder by Baranovskii for OFETs. The EGDM and the GDM by Baranovskii will be initially compared in terms of the parametrization method and their physical rigorousness at the low electric field. Then, we will examine two ambiguous physical parameters in GDMs, the localization length and the attempt-to-escape frequency as key parameters for the explicit parametrization. Finally, experimentally measured transfer curves of OFETs at various temperatures will validate the parametrization via a numerical simulation.

5.1 Gaussian disorder models

5.1.1 Limits of initial parametrization

Before elucidating on the parameterization of the GDM, let us review the experimental data on the gate-voltage V_{GS} dependence of mobility reported in the literature, which represents OFETs with various degree of disorder. In Fig.

5.1a, each symbol marks the maximum mobility ($\mu_{\max}$) and the order of μ-modulation by V_{GS} of a device. The former indicates μ at the maximum V_{GS} and the latter indicates how many times $\mu_{\max}$ increases from μ at the minimum V_{GS} within the on-state. The transistors made of single crystal (SC) molecules [75], [136], [137] and donor-acceptor (DA) copolymers [1]–[3] exhibited a negligible or very small μ-modulation between 1 to 2. On the other hand, the transistors consisting of polycrystalline (PC) molecules [9]–[17], semi-crystalline (semi-C) polymers [1], [4], [5] and disordered polymers [6]–[8] showed a large μ-modulation between 5 to 15. In essence, the gate-voltage V_{GS} dependence of mobility is strongly correlated with the type of semiconductor material in terms of both $\mu_{\max}$ and the order of μ-modulation by V_{GS}.

According to the GDM, the modulation by charge carrier concentration is larger when the disorder is higher. In addition, the μ-modulation by V_{GS} is equal to the same by charge carrier concentration because the application of V_{GS} increases the charge carrier concentration in the channel. This infers that a device exhibiting a large μ-modulation by V_{GS} has a higher disorder in the semiconductor thin film. In Fig. 5.1b, Gaussian width of representative material for each category in Fig. 5.1a was studied from literature. When the Gaussian width σ, which represents the energetic disorder, is small ($\sigma < 2kT$) such as rubrene [138]–[140] and IDTBT [1], [141], μ-modulation is arithmetic [84] [142]. When the Gaussian width σ becomes larger ($\sigma > 2kT$) such as PBTTT [1], [143], [144], Pentacene [145]–[148] and PPVs [6], [84], [149], μ-modulation is exponential, i.e. 1, 2, 3, and 4 orders of magnitude for $\sigma = 3kT, 4kT, 5kT$ and $6kT$.

Remarkably, the initial parameterization of the GDM took a small localization length a ($a \approx 0.1\,\mathrm{nm}$) [84], [150] in order to describe characteristics of the transistors with molecularly doped polymers [68] and chemically modified poly(p-phenylene vinylene)s (PPVs) [84] showing low mobility in the range of 10^{-5}~$10^{-4}\ \mathrm{cm^2/V \cdot s}$ with the μ-modulation by about an order [151], [152]. For this initial parametrization of the GDM, a small localization length a was determinant for the low mobility. In fact, most previous studies adopted very small values of a. For instance, $a = 0.2b$ was used in the work of Bassler [68] and $a = 0.1b$ was adopted by Pasveer [84]; Each value corresponds to $a \approx 0.14\,\mathrm{nm}$ for the Bassler's work and

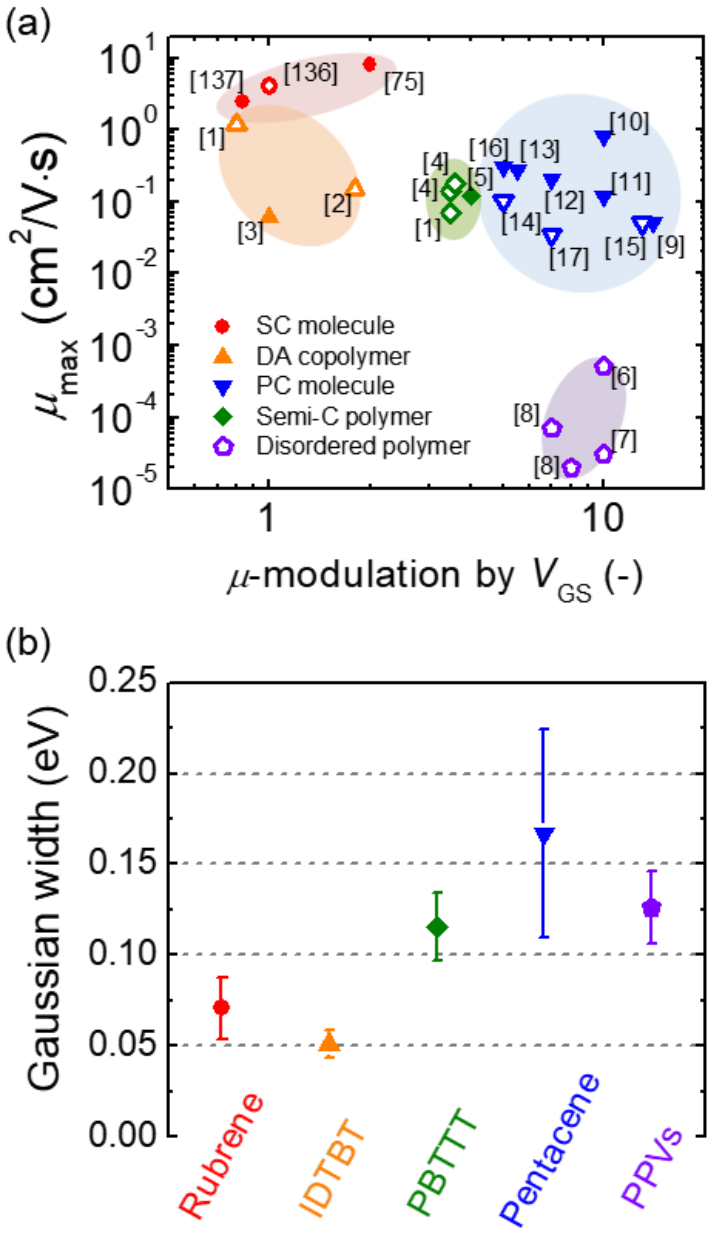

Fig.5.1. μ_{max} versus μ modulation by V_{GS} for various OFETs at room temperature. Donor-Acceptor (DA) copolymer for IDTBT [1] and DPP-DTT [2-3]; Semi crystalline (SemiC.) polymer for P3HT [4], PBTTT [1, 5]; Disordered polymer for chemically modified PPV [6-8]; Poly crystalline (PC) molecule for T6 [9], Pentacene [10-15], diF-TEG-ADT [16] and DH6T [17]; Single Crystal (SC) molecule for Rubrene [75,136,137]. Filled symbols represent contact resistance modulated μ and open symbols represent contact resistance unmodulated μ. (b) Extracted Gaussian width from literature for Rubrene [138-140], IDTBT [1, 141], PBTTT [1, 143, 144], Pentacene [145-148] and PPVs [6, 84, 149].

$a \approx 0.07$ nm for the Pasveer's work when $b \approx 0.7$ nm ($b = N_0^{-1/3}$ and $N_0 = 3 \times 10^{21}$ cm^{-3}).

On the other hand, this initial parameterization is not adequate to account for the high mobility in the range of 10^{-2}~10 cm^2/V·s with similar and/or large μ-modulation by about an order or larger observed recently from transistors with semi-crystalline polymers (e.g. P3HT, PBTTT…) and small molecules (e.g. pentacene, Tips-pentacene…). As will be demonstrated in the next sub-section, if the initial parameters were used, the calculated mobility results in several order of magnitude smaller compared to the measured mobility. This means that the charge carrier can hardly hop when the state is strongly localized, i. e. small a, so that the hopping transition rate decreases exponentially by Eq. (2.14). Recent Monte-Carlo simulation results also show that the modification of a significantly changes the mobility [134]. Therefore, the increase of a would be necessary to increase the mobility in a system with higher disorder to a reasonably high value.

In addition, the attempt-to-escape frequency ν_0, which is the pre-factor of the MA transition rate of Eq. (2), affects the mobility. The common values used in the initial parameterization of GDM [82], [84] were taken from phonon frequency 10^{12}~10^{13} s^{-1} [153], [154] in regards of the charge carrier transfer as the emission or the absorption of a phonon abiding by the conservation of energy [155]. This means that ν_0 could vary depending on the material properties such as the electron-phonon coupling strength, the density of states of phonon, and hence disorder [156]. Therefore, a further study on the relationship between ν_0 and mobility from a new perspective is also a timely subject to improve the consistency of a new parameterization.

5.1.2 Parametrization method of EGDM

The parametrization of the GDM starts from five physical parameters of the organic material, N_0, σ, a and ν_0 in Eq. (2.6) and (2.14), and the percolation constant B_c which represents the average number of connected sites within the hopping distance. Based on these five parmeters, the goal of parametrization in EGDM is to find c_1 and c_2 in Eq. (2.17). Initial parametrization of EGDM was $c_1 = 1.8 \times 10^{-9}$ and $c_2 = 0.42$ at $N_0 \cdot a^3 = 10^{-3}$ [84]. In this work, we

extracted c_1 and c_2 by direct fitting between the reduced mobility of the zero-carrier limit $\mu_0(T)/\mu_0$ from Eq. (2.17), i.e. $c_1\exp(-c_2\hat{\sigma}^2)$, and from the Vissenberg-Matters (VM) model with the Gaussian DOS [83]. We adopted the VM model to consider the VRH nature instead of the nearest-neighbor hopping (NNH) because the initial numerical solution by Eq. (2.20) only considered first and second nearest neighbor hopping [157]. In addition, the VM model provides an explicit result of $\mu_0(T)/\mu_0$ since the derivation of the analytical expression in Eq. (2.17) originated from the VM model. Here, the parametrization of the EGDM considered various $N_0 \cdot a^3$ values, 10^{-1}, $10^{-2}, 10^{-3}$ and 10^{-4}.

In Fig. 5.2, c_1 and c_2 were extracted by fitting of $\mu_0(T)/\mu_0$ from $1kT$ to $6kT$; $c_1 = 2.75 \times 10^{-17}$ and $c_2 = 0.511$ at $N_0 \cdot a^3 = 10^{-4}$; $c_1 = 1.62 \times 10^{-8}$ and $c_2 = 0.491$ at $N_0 \cdot a^3 = 10^{-3}$; $c_1 = 1.86 \times 10^{-4}$ and $c_2 = 0.443$ at $N_0 \cdot a^3 = 10^{-2}$; and $c_1 = 1.54 \times 10^{-2}$ and $c_2 = 0.351$ at $N_0 \cdot a^3 = 10^{-1}$. As $N_0 \cdot a^3$ enhanced 3 orders of magnitude, c_1 increased dramatically more than 15 orders of magnitude. This result indicates that variation of localization length gives a significantly effect on the magnitude of calculated mobility. In contrast, c_2 decreased slightly that illustrates the deviation among different σ in the same condition of $N_0 \cdot a^3$ is reduced. In $N_0 \cdot a^3 = 10^{-1}$, calculated mobility for $\sigma = 0.1$ and 0.15 eV were overlapped at large $p/N_0 = 10^{-1}$, whereas there was a huge deviation in $N_0 \cdot a^3 = 10^{-4}$. Because c_2 included in the exponential term with Gaussian width and temperature, c_2 modulates the mobility gap between different Gaussian width.

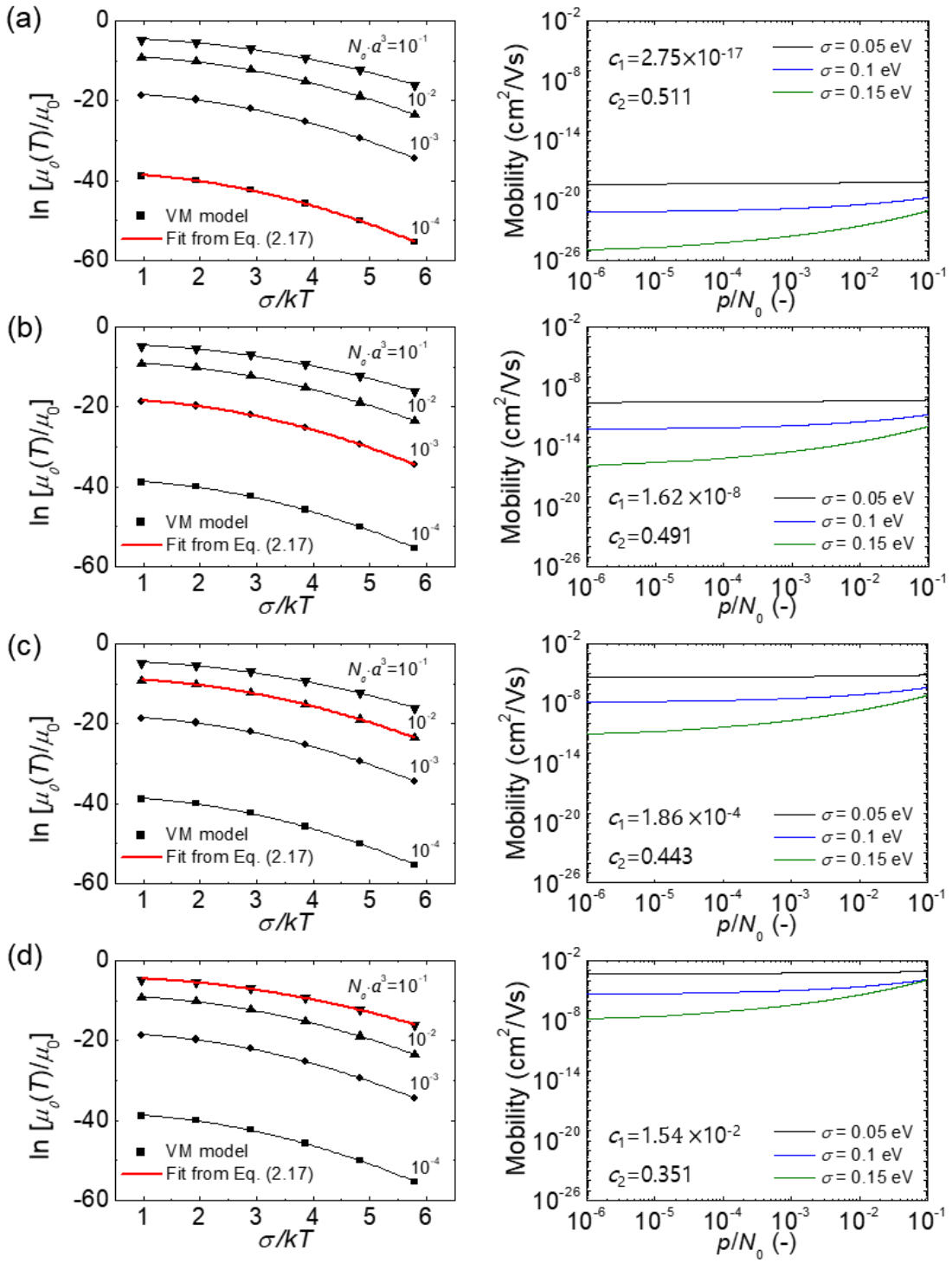

Fig.5.2. Fitting between $\mu_0(T)/\mu_0$ from Eq. (2.17) and VM model to extract c_1 and c_2 (left) and calculated mobility with parametrized c_1 and c_2 (right) with various Gaussian width σ for various $N_0 \cdot a^3$ values (a) 10^{-4}, (b) 10^{-3}, (c) 10^{-2} and (d) 10^{-1}. $\nu_0 = 10^{12}\ 1/s$ was assumed for all calculations.

5.1.3 Parametrization method of GDM by Baranovskii

Different with the EGDM, initial physical parameters determine directly all the parameters in GDM by Baranovskii without fitting process (Fig. 5.3). From N_0, σ, a, ν_0 and B_c, the dimensionless function for generalized Einstein relation F_{ER}, Fermi level ε_F, transport energy ε_t and hopping distance $r(\varepsilon_t)$ are calculated. Then, final mobility can be obtained. Because additional fitting process is not necessary for parametrization of GDM by Baranovskii, this model is more simple and straightforward. However, selection of initial physical parameters is more importance because they determined final mobiliy directly.

For parametrization of the GDM by Baranovskii, the model transport energy ε_t and hopping distance $r(\varepsilon_t)$ and final mobility were successively calculated with variation of the a from 0.1 nm to 1nm. The calculation considered $\sigma = 0.05, 0.1$ and 0.15 eV with fixed $p/N_0 = 3 \times 10^{-4}$ at which the channel is formed. When a was low, ε_t values were close to $HOMO_{max}$ (0 meV) and $r(\varepsilon_t)$ is very small (Fig. 5.4a and b). As a increased one order of magnitude, both parameters increased rapidly with respect a; ε_t increased as much as 97, 214 and 414 meV and $r(\varepsilon_t)$ increased 0.59, 1.12 and 1.58 nm for $\sigma = 0.05, 0.1$ and 0.15 eV, respectively from 0.1nm to 1 nm. The increment of parameters is remarkable at the large Gaussian width because behaviors of charge

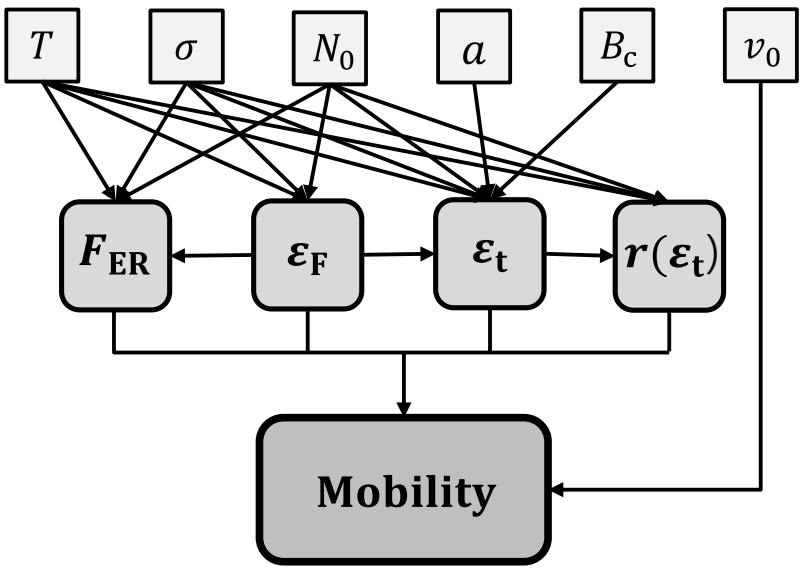

Fig.5.3. The parametrization process of GDM by Baranovskii

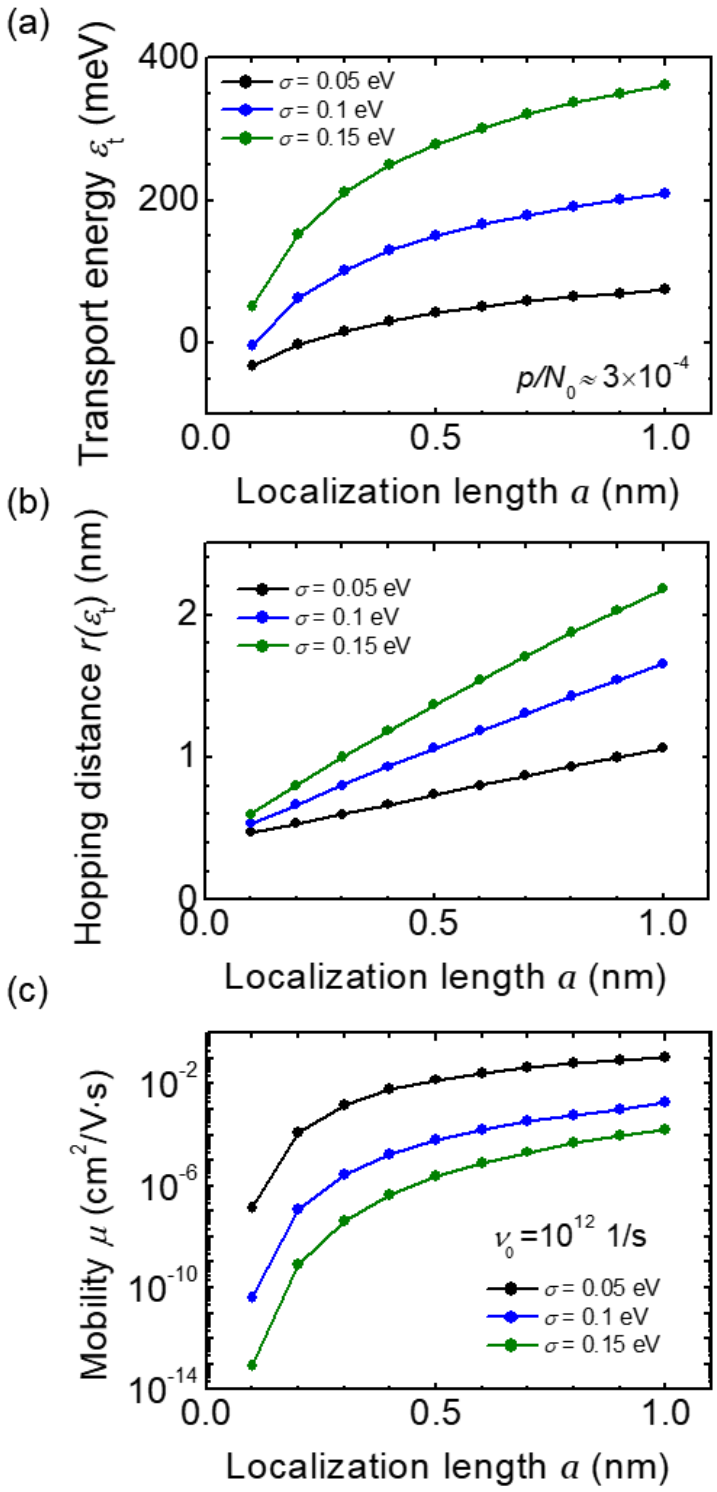

Fig.5.4. Calculated results of (a) transport energy ε_t, (b) hopping distance $r(\varepsilon_t)$ and (c) final charge carrier mobility of GDM by Baranovskii with respect to the a. Various $\sigma = 0.05, 0.1$ and 0.15 eV, $\upsilon_0 = 1 \times 10^{12}$ 1/s and $p/N_0 \approx 3 \times 10^{-4}$ are used for calculation.

carriers change easily in the broad Gaussian width. As a consequence, the mobility dramatically increased nearly 6, 8 and 10 orders of magnitude from $a = 0.1$ to $1\,\text{nm}$ for $\sigma = 0.05, 0.1$ and $0.15\,\text{eV}$, respectively (Fig. 5.4c). Similar with the parametrization of EGDM, the variation of a affects significant effect on the magnitude of mobility. Physical mechanism of mobility modulation by a will be studied in next sections.

5.1.4 Advantages of the GDM on spatially random sites

We calculated the mobility and hopping distance by the GDM on a cubic lattice and the GDM on spatially random sites in order to support the needs to consider higher localization length claimed in the Sec. 5.1.1 and to support the use of the

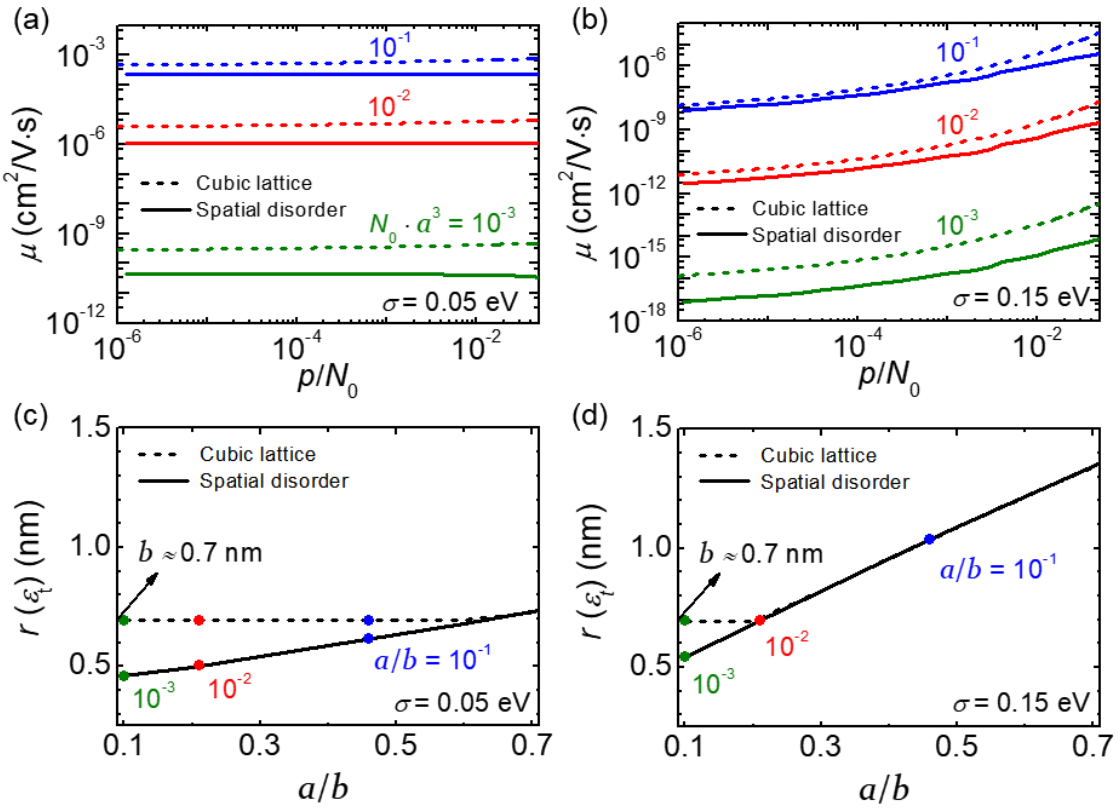

Fig.5.5. Calculated mobility by the EGDM (solid line) and the GDM by Baranovskii (dotted line) with various $N_0 \cdot a^3$ and calculated $r(\varepsilon_t)$ in the cubic lattice and the spatial disorder for (a), (c) $\sigma = 0.05\,\text{eV}$ and (b), (d) $\sigma = 0.15\,\text{eV}$. In the calculation, $\nu_0 = 10^{12}\,\text{s}^{-1}$ and $B_c = 2.735$ were used.

GDM on spatially random sites. For the calculation, we varied the localization length as $N_0 \cdot a^3 = 10^{-3}, 10^{-2}$ and 10^{-1} assuming fixed N_0 and the Gaussian width as $\sigma = 0.05$ eV and 0.15 eV (Fig. 5.5). The difference between two GDMs at the high electric field condition was analyzed already by Baranovskii and coworkers [134], [135]. The comparison of two GDMs in this study is to emphasize that difference exists even at low electric field so that that the GDM on spatially disorder sites is in general a better theoretical framework, and that a reparameterization is required more for the GDM on spatially random sites.

Regarding the effect of Gaussian width, the μ-modulation with relative hole density p/N_0 was negligible for $\sigma = 0.05$ eV whereas it amounted to about 10^3 for $\sigma = 0.15$ eV for all localization conditions. In addition, the mobility decreased significantly by order of 10^{-4}, 10^{-5} and 10^{-6} for each localization condition when the Gaussian disorder is varied from $\sigma = 0.05$ eV to $\sigma = 0.15$ eV. Regarding the effect of localization length, the mobility increased significantly by 10^7 for $\sigma = 0.05$ eV and by 10^{10} for $\sigma = 0.15$ eV when $N_0 \cdot a^3$ increased from 10^{-3} to 10^{-1}. This means that the magnitude of μ changes more significantly by a at higher σ. On the contrary, how μ is modulated by hole concentration was not affected by a.

Remarkably, the mobility calculated by the GDM on a cubic lattice was higher, at least 2.5 times to about an order, than that by the GDM on spatially random sites and this tendency was greater for small localization length (Fig. 5.6). Concomitantly, the aforementioned variation by Gaussian width or localization length was even more pronounced in the GDM on spatially random sites. The variation of a represents two different hopping mechanisms: the charge carriers tend to hop to adjacent states when a is small (NNH), whereas they tend to hop to farther states when a is large (VRH). The discrepancy in mobility between two GDMs (Fig. 5.5a and b) results dominantly from the overestimation of hopping distance $r(\varepsilon_t)$ on a cubic lattice which is limited to the inter-site distance b [83] (Fig. 5.5 (c) and (d)).

For this reason, a reparameterization for the GDM is necessary and becomes even more important for the GDM on spatially random sites in order to correctly describe the charge transport through both VRH and NNH. It is now clear that the modulation of mobility by hole concentration is determined by the Gaussian width and that the magnitude of mobility is determined by the

localization length. In particular, the localization length must be increased greater than the conventional values ($N_0 \cdot a^3 = 10^{-1}$) in order to explain the high mobility of disordered transistors from recently reports.

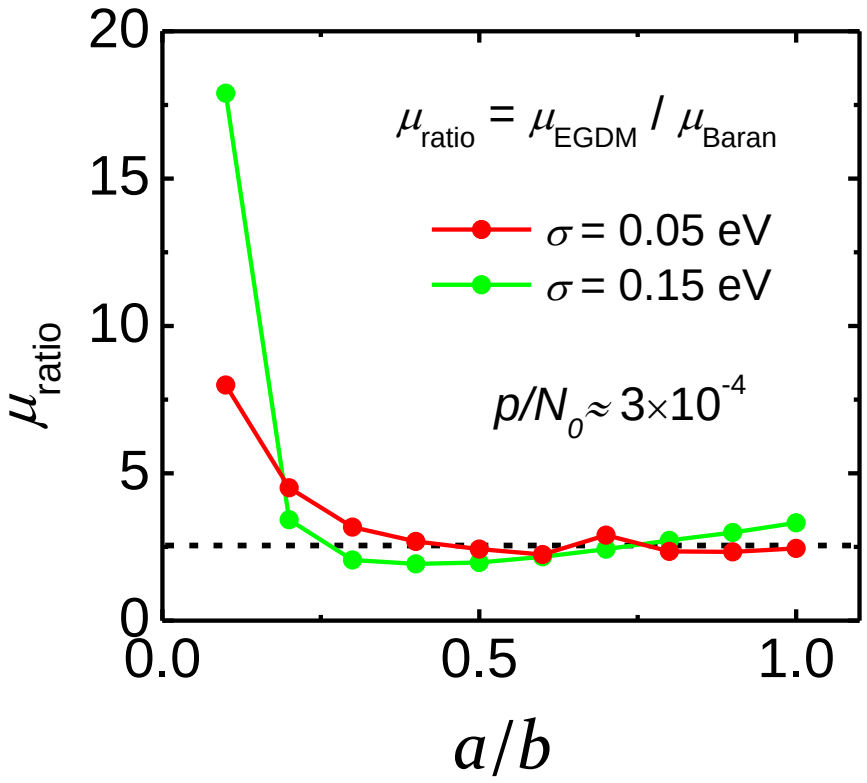

Fig.5.6. Ratio of calculated mobility by the EGDM and the GDM by Baranovskii for both $\sigma = 0.05$ eV and $\sigma = 0.15$ eV. Dotted line indicates $\mu_{\text{ratio}} = 2.5$. In the calculation, $p/N_0 = 3 \times 10^{-4}$ was used.

5.2 Parametrization

5.2.1 Localization length

Compared to the mobility measured from OFETs made of DA copolymers, semi-crystalline polymers, and polycrystalline small molecules (Fig. 5.1), the mobility calculated by the GDM on spatially random sites using initial parameterization were still very low (Fig. 5.5a and b). In order to address this discrepancy, a needs to be enlarged greater than values in Fig. 5.5. The exact value of a could be determined by the Arrhenius plot because a slope Δ with respect to

temperature, i.e. the activation energy ε_a, depends on the a. By referring to the parameterization scheme in Fig. 5.3 and Eq. (2.21), which is a major benefit of the GDM on spatially random site, a affects directly on ε_t. If the Arrhenius plot is numerically plotted by Eq. (2.26), the slope Δ would vary with a, considering that ε_a is the energy for a charge carrier should overcome to hop upwards from ε_F to ε_t ($\varepsilon_a = \varepsilon_t - \varepsilon_F$).

By the GDM on spatially random sites, we compared Arrhenius plot that was experimentally measured and that was numerically calculated with respect to a for various Gaussian widths corresponding to polycrystalline molecule (pentacene), semi-crystalline polymer (PBTTT, data from [1]), and D-A copolymer (IDTBT, data from [1]) (Fig. 5.7). The calculation considered a from

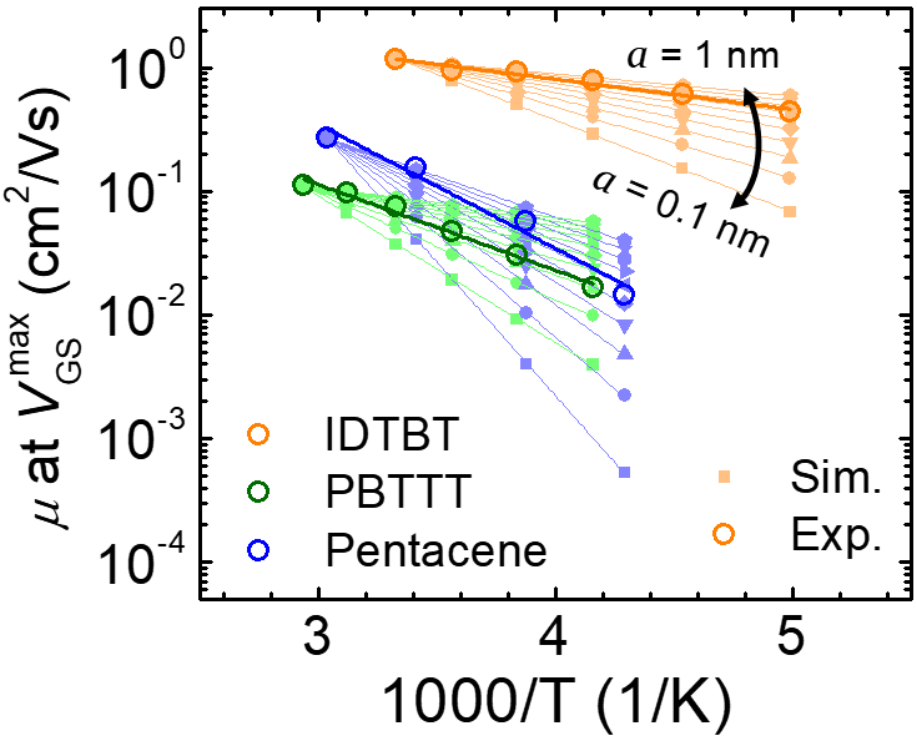

Fig.5.7. Experimentally measured and numerically calculated Arrhenius plots for IDTBT, PBTTT and pentacene. Calculation considered $\sigma = 0.059$ eV, $N_0 = 7.4 \times 10^{20}$ cm^{-3} and $p/N_0 = 0.0126$ for IDTBT, $\sigma = 0.11$ eV, $N_0 = 8.9 \times 10^{20}$ cm^{-3} and $p/N_0 = 0.0243$ for PBTTT and $\sigma = 0.15$ eV, $N_0 = 3 \times 10^{21}$ cm^{-3} and $p/N_0 = 3 \times 10^{-4}$ for pentacene.

0.1 nm to 1nm and the mobility at the highest temperature was fitted to the experimental order by varying ν_0 for each a. Slopes became smaller as a increased for all materials (Fig. 5.8(a)). From experimentally measured slopes Δ_{exp}, we obtained $a = 0.75$ nm (Δ_{exp}= 20.9 meV) for IDTBT, $a = 0.29$ nm (Δ_{exp}= 59.7 meV) for PBTTT and $a = 0.56$ nm (Δ_{exp}= 86.6 meV) for pentacene. Interestingly, calculated slopes of Arrhenius plot that has been regarded as ε_{a}, were smaller that directly calculated ε_{a} by $\varepsilon_{\mathrm{a}} = \varepsilon_{\mathrm{t}} - \varepsilon_{\mathrm{F}}$ using Eq. (2.21) (Fig. 5.8b). This indicates that $\Delta \neq \varepsilon_a$ in the empirical Arrhenius form $\mu(T) \simeq \mu_0 \exp(-\Delta/kT)$ [68], [82] in the GDM on spatially random sites because prefactor in Eq. (2.26) is not independent to *T*. In our calculation, ε_{t} (Fig. 5.9a) varied between *T* = 300 K and 200 K as well as $r(\varepsilon_{\mathrm{t}})$ (Fig. 5.9b) that belong to the prefactor μ_0.

According to one-dimensional (1-D) model by Nenashev and coworkers, the effective localization length a_{eff} is similar to the molecular diameter *D* rather than the bare localization length a_0 (of the order of several Ångströms) [158]. It conforms to the VRH transport that the wavefunction penetrates not only into the adjacent molecules but also into the more remote ones. In 3-D system, direct estimation of *D* is difficult because molecular orientation stacks with planar plane due to the pi-pi staking. In this case, a intermolecular distance (*ID*) along the pi-pi staking can replace *D*. The calculated a is very

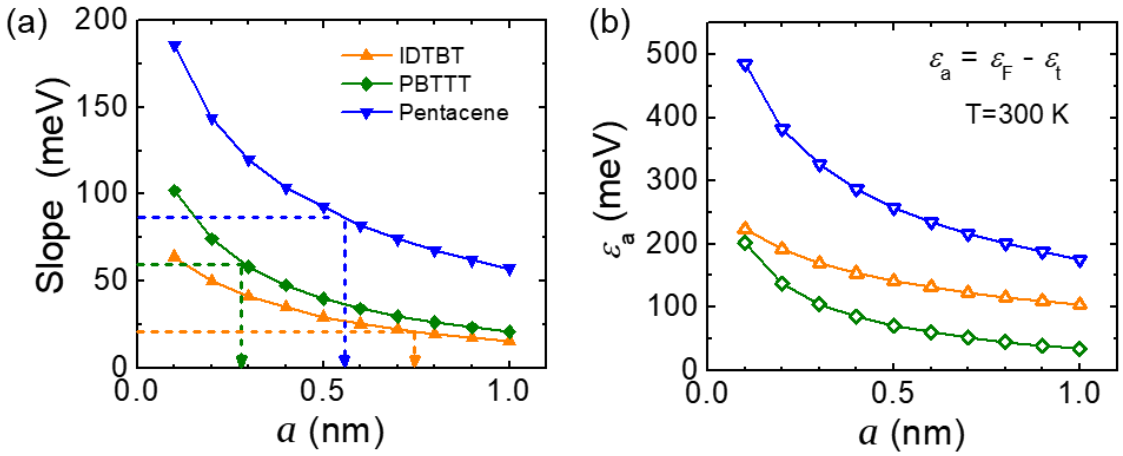

Fig.5.8. (a) Slopes of Arrhenius plot Δ with respect to a from Fig. 5.7. Horizontal and vertical dotted lines indicate Δ_{exp} and extracted a, respectively. (b) Direct calculation of $\varepsilon_{\mathrm{a}} = \varepsilon_{\mathrm{t}} - \varepsilon_{\mathrm{F}}$ using Eq. (2.21).

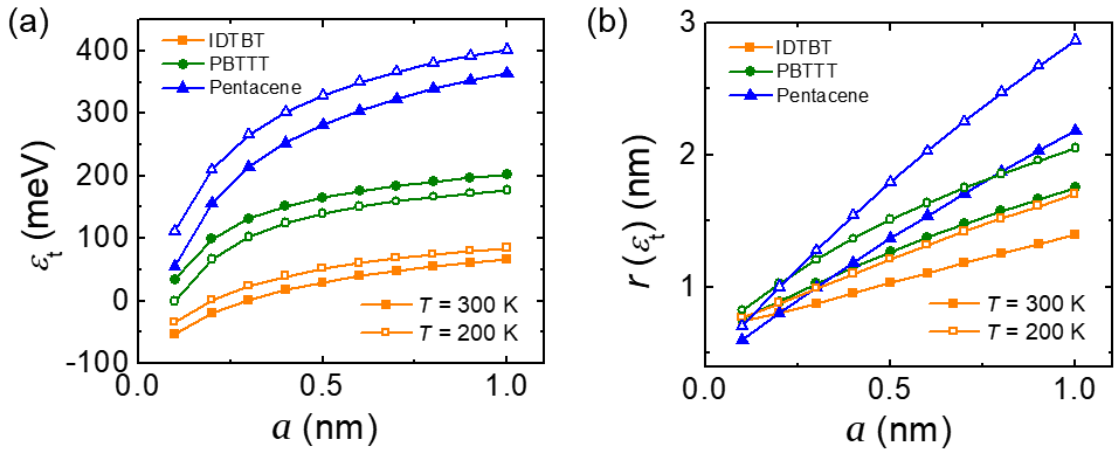

Fig.5.9. (a) Calculated ε_t and (b) $r(\varepsilon_t)$ with respect to a for T = 200 K and 300 K.

close to *ID* reported in the literature: 0.41 v.s. 0.75 nm for IDTBT [49]; 0.38 v.s. 0.29 nm for PBTTT [159]; and 0.4 v.s. 0.56 nm for pentacene [160] .

For IDTBT, quasi-1D transport with occasional intermolecular hopping though short pi-pi bridges occurs [50] so that vertial *ID* (0.41 nm from Grazing incidence X-ray scattering (GIXS) measurement of *d*-spacing) is a determinant for a because intramolecular transport is faster than intermolecular hopping (Fig. 5.10(a)) [49]. For PBTTT, polymers stand edge on the substrate and 2D transport takes place in the pi-pi staking direction so that the backbone's shortest length (0.38 nm from density functional theory (DFT) calculation) corresponds to the *ID* (Fig. 5.10b) [159]. For pentacene OFETs (Fig. 5.10c), molecules stand vertically on the insulator so that charge carriers hop along the in-plane pi-pi stacking direction [161]. Therefore, assuming a 3-D cuboid, the *ID* is around 0.4 nm [160].

We will describe how a affects the mobility via ε_t that manipulates ε_a and $r(\varepsilon_t)$ on the disordered system (Fig. 5.11). For all disorder conditions, ε_t became smaller as a increased (Fig. 5.11a), whereas $r(\varepsilon_t)$ increased with the increase of a (Fig. 5.11b). In this context, an origin of ε_t variation can be explainable by a physical definition of ε_t, the energy that offers the fastest hopping transition rate for charge carrier [82]. When a is small, and hence ε_t is close to $\mathrm{HOMO_{max}}$ (0 eV), a charge carrier does not have sufficient states to hop for in the spatial domain due to the small $r(\varepsilon_t)$. Therefore, an energy which

possesses a large number of states in the energetic domain is likely to be selected as ε_t to get a fastest upward hopping transition rate. This mechanism can illustrate that ε_t is close to the center of Gaussian DOS at small a. When the a is large, ε_t prefers to be an energy which possesses small amounts of states because the system has enough states to hop in the spatial domain by large $r(\varepsilon_t)$. Consequently, ε_t moves towards ε_F and mobility increased by decreased ε_a.

We now depend on the localization length to parametrize GDM by Baranovskii. In the next section, we will cover another obscure parameter, the attempt-to-escape frequency to fit the mobility.

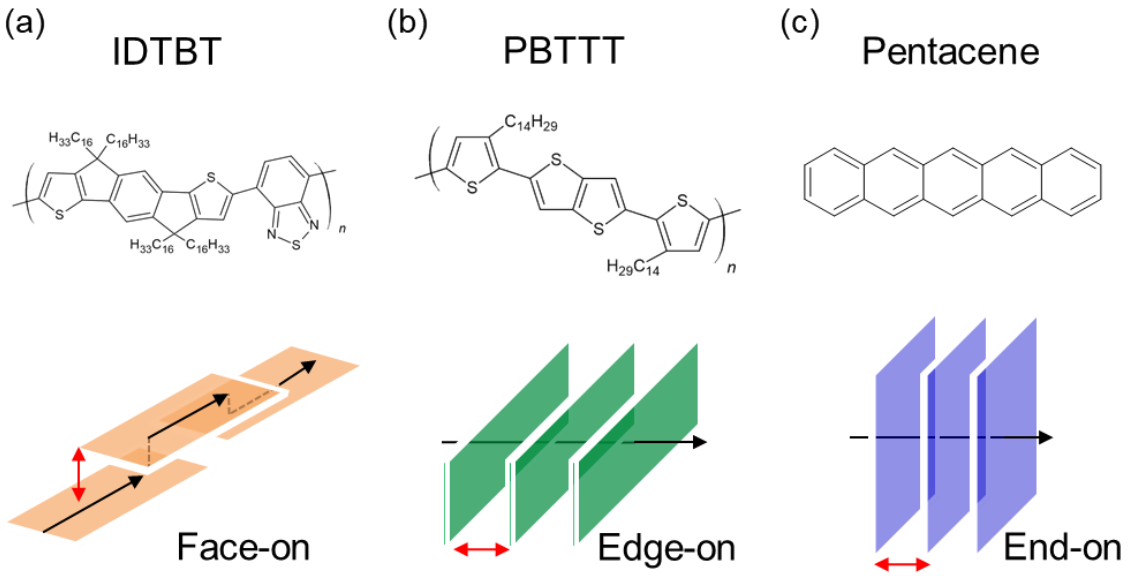

Fig.5.10. Molecules and molecular orientation in thin-film of (a) IDTBT, (b) PBTTT and (c) pentacene Black arrows indicate the direction of charge transport and red double arrows indicate intermolecular distance of pi-pi stacking.

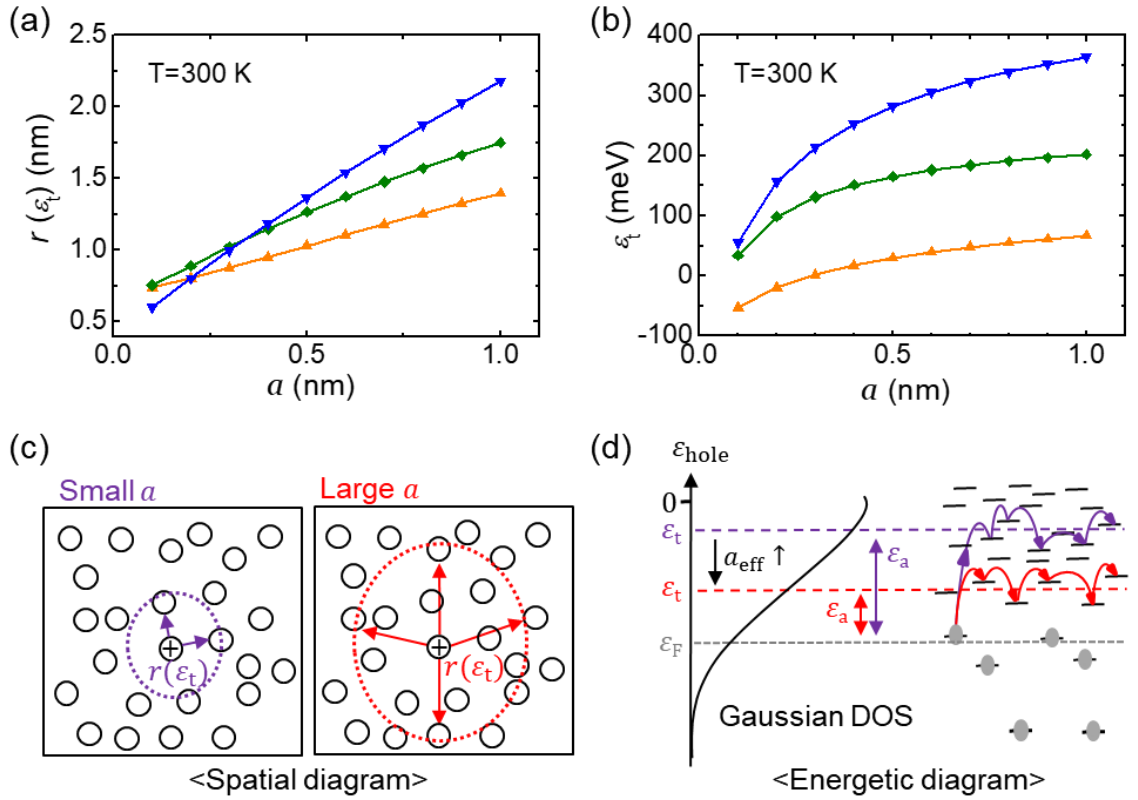

Fig.5.11. Calculated results of (a) $r(\varepsilon_t)$ and (b) ε_t with respect to the localization length a. Schematic illustration of the hopping range in (c) the spatial and (d) energy diagram for different localization length a: small a in violet color; large a in red color.

5.2.2. Attempt-to-escape frequency

In Fig. 5.7, direct fitting of numerically calculated Arrhenius plots to the experimentally measured one at the highest temperature determined ν_0 for each material; $\nu_0 = 7.05 \times 10^{14}\ \mathrm{s}^{-1}$ for IDTBT ($a = 0.75$ nm); $\nu_0 = 2.9 \times 10^{17}\ \mathrm{s}^{-1}$ for PBTTT ($a = 0.29$ nm); and $\nu_0 = 5.27 \times 10^{16}\ \mathrm{s}^{-1}$ for pentacene ($a = 0.56$ nm) (Fig. 5.12a). When a is small, ν_0 tends to increase because small a produce low magnitude of mobility. Thus large ν_0 needs to fit experimental order. Noted that extracted ν_0 values are one to even four orders of magnitude higher than conventional values $\nu_0 = 10^{12}$ and $10^{13}\ \mathrm{s}^{-1}$ [82], [84].

We examined these extracted ν_0 from Fig. 5.7 by a comparison between a direct calculation of the charge transition rate ν_{ij} by Eq. (2.14) and its theoretical estimation in the literature. If a calculated result of ν_{ij} by Eq. (2.14)

with a obtained ν_0 was in the order of theoretical estimations of ν_{ij}, then this ν_0 would have the physical rigorousness. The ν_{ij} was calculated by the right-hand side of Eq. (2.14) with extracted ν_0 values. The calculation considered $r(\varepsilon_t)$ in Eq. (2.22) as r_{ij} and $\varepsilon_j = \varepsilon_t$ as well as $\varepsilon_i = \varepsilon_F$ for upward hopping. Direct calculation of upward and downward transition rates ν_{ij} by Eq. (2.14) were $\nu_\uparrow = 2.76 \times 10^{11}\ s^{-1}$ $\nu_\downarrow = 2.73 \times 10^{13}\ s^{-1}$ for IDTBT, $\nu_\uparrow = 3.42 \times 10^{11}\ s^{-1}$ $\nu_\downarrow = 2.69 \times 10^{14}\ s^{-1}$ for PBTTT and $\nu_\uparrow = 2.01 \times 10^{10}\ s^{-1}$ $\nu_\downarrow = 2.74 \times 10^{14}\ s^{-1}$ for IDTBT. Globally, $\nu_\downarrow$ are higher than $\nu_\uparrow$ because downward hops are independent to the energetic distribution of states so that they are faster than upward hops.

To compare with the directly calculated ν_{ij}, theoretical estimations of ν_{ij} were studied via MA and Marcus charge transfer models [162]. Based on the MA transition rate, Bassler [153] stated that the small interaction energy between molecules induced by the weak intermolecular coupling leads to hopping transition rates between 10^{11} and $10^{13}\ s^{-1}$. More recently, Brédas and coworkers calculated similar orders of energy transfer rate in the donor-acceptor pairs [154]. Marcus model is another charge transfer model in localized states that is compatible with the MA transition rate. In this model, the reorganization energy from geometric relaxation during charge transfer and electronic coupling matrix element are key parameters to describe hopping transport. Based on this theory, hole and electron transfer rates were calculated in the range between 10^{12} and $10^{13}\ s^{-1}$ in various organic disorder materials [163], [164]. Remarkably, Nan and coworkers proved that the hole transfer rate of rubrene, tetracene and pentacene could reach up to $10^{14}\ s^{-1}$ with considering the quantum nuclear tunneling effect [165].

Interestingly, direct calculations of ν_{ij} with extracted ν_0 belonged to the range of theoretical estimations of ν_{ij} in spite of abnormally high values. This result illustrates that ν_0 can have the order upto $10^{17}\ s^{-1}$ depending on materials and this value is four orders of magnitude higher than conventionally accepted values for GDMs.

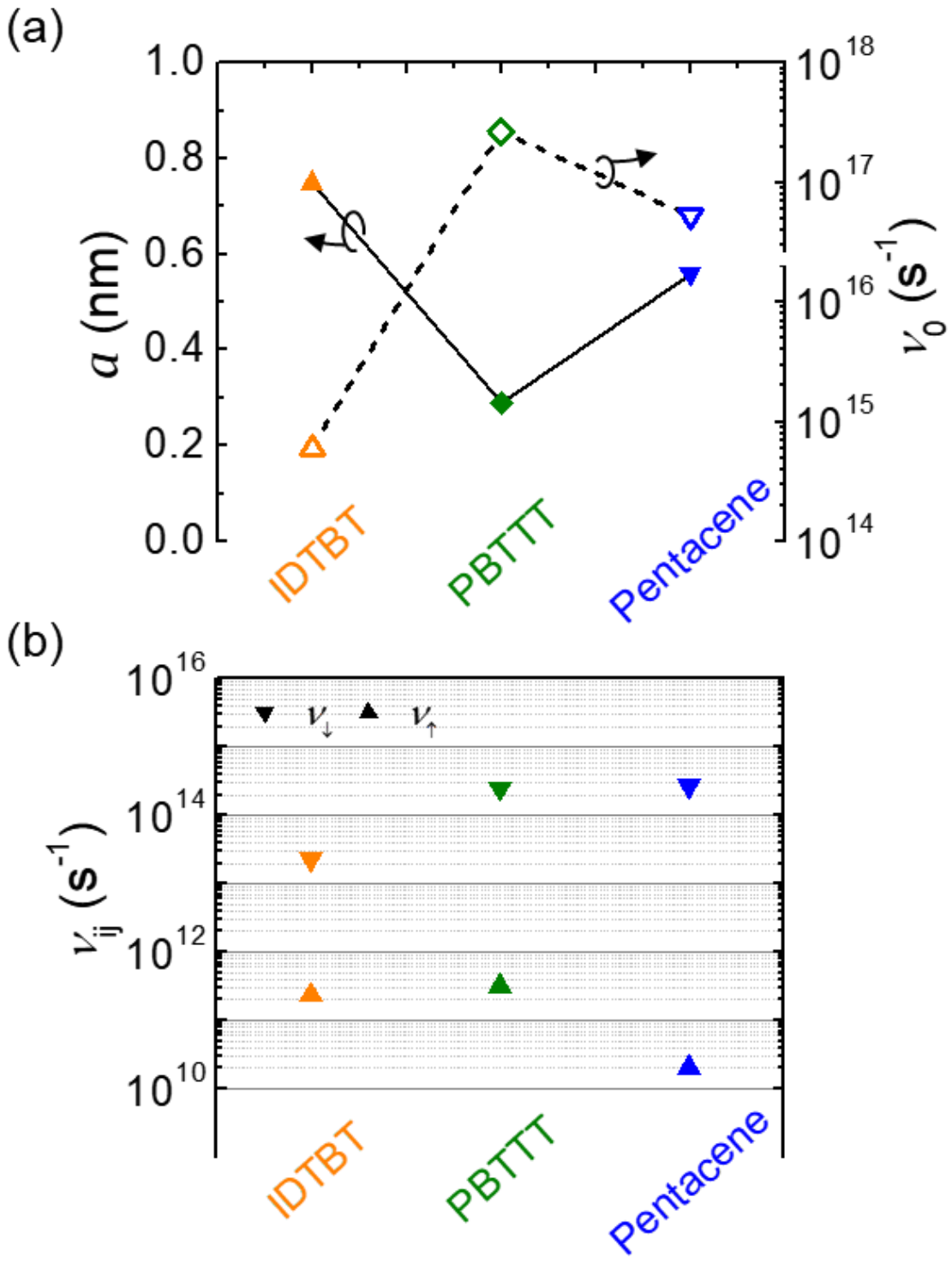

Fig. 5.12. (a) Extracted a and ν_0 from Fig. 5.7 for three different matrials, IDTBT, PBTTT and pentacene. (b) Direct calculation of MA upward $\nu_\uparrow$ and downward $\nu_\downarrow$ transition rates by Eq. (2) with extracted ν_0.

5.3 Experimental validation

5.3.1 Experimental data of OFETs

In this section, we validated the parametrization of the GDM by Baranovskii via a comparison between the experimental result of IDTBT, PBTTT and pentacene OFETs and the numerical TCAD simulation. Temperature evolution of transfer characteristics of IDTBT and PBTTT (Fig. 5.13a and b, symbols) based top-gate staggered OFETs were taken from Venkateshvaran et al. [1]. Temperature varied 300 K to 200 K for IDTBT and 340 K to 240 K for PBTTT at intervals of 20 K. For pentacene, bottom-gate staggered OFET was fabricated. Details of fabrication method is summarized in Appendix. Temperature evolution of transfer curves were measured by an Agilent 5270B analyzer under vacuum (Fig. 5.13c, symbols). Janis cryostat allows to vary temperatures, T = 330 K, 300 K, 260 K and 230 K. Experimentally obtained drain current increased gradually as temperature increased for all OFETs because the hopping transport was promoted by temperature.

5.3.2. Numerical simulation of OFETs

For the numerical simulation, we implemented the GDM on random sites in Sec. 2.4.3 into the SILVACO, Atlas, which is a commercial TCAD numerical simulator based on the finite-element method. It calculates self-consistently the Poisson's, the continuity and the drift-diffusion equations with physical characteristics of ODSs such as the Gaussian DOS, the generalized Einstein's relation and the GDM by Baranovskii. The simulator calculated transfer characteristics with same conditions of fabricated devices such as geometrical structure and temperatures.

Numerically calculated temperature evolution of transfer curves (Fig. 5.13, solid lines) showed almost accurate fits to the experimental results with a single set of parameters (Table 5.1). Parameter set contains five physical parameters in the GDM by Baranovskii (Fig. 5.3), device parameters and secondary Gaussian trap states. Considering μ-modulation and Gaussian width in Fig. 5.1, proper Gaussian width σ were adopted. Also, we used values of localization length and attempt-to-escape frequency discussed in Sec. 5.2. Parameters such as N_0 [1],

[166], the dielectric constant of semiconductor ε_s [125], [167], [168], and the percolation constant B_c [82], [169] were determined from literature. Simulation of IDTBT and pentacene based OFETs adopt Gaussian-distributed donor-like bulk trap states via the double Gaussian DOS model [96] to make a better numerical fit. $\sigma_{\mathrm{d.bulk}}$ were identical with σ_{i} and the volumetric bulk trap density $N_{\mathrm{d.bulk}}$ adopted typical order of the unintentional doping level [125]. Lastly, $E_{\mathrm{d.bulk}}$ were determined by systematic simulations. Noted that we assumed Gaussian bulk trap states are invariable to temperatures.

At low temperature of pentacene OFETs, numerical fit was not successful to measured transfer curves despite the presence of bulk trap states (Fig. 5.13c, solid lines). This deviation attributed to the additional interface trap states between semiconductor and gate insulator. Basically, weak intermolecular bonding of ODS merely induces interface trap states at surface termination [97]. However, the mismatch of thermal strain between semiconductor and gate insulator can cause trap states in the interface at low temperature [170]. According to the universal scaling between ε_a and interfacial thermal expansion mismatch (ITEM) by Mei *et al*, $\Delta_{\mathrm{exp}} = 86.6$ meV (Pentacene in this study, Δ_{exp} corresponds to ε_a in Mei *et al*) indicates ITEM ≈ 50, whereas $\Delta_{\mathrm{exp}} = 59.7$ meV (PBTTT) and $\Delta_{\mathrm{exp}} = 20.9$ meV (IDTBT) indicate ITEM ≈ 20 and 5, respectively. Because interface trap density is proportional to ITEM, the effect of interface trap states is particularly appeared in pentacene-based OFET. For numerical simulation, the order of areal interface trap density $N_{\mathrm{d.it}}$ was determined from the areal molecular density $4.8 \times 10^{14}\ \mathrm{cm}^{-2}$ and the ratio between N_0 and $N_{\mathrm{d.bulk}}$, i.e. $3 \times 10^{21} : 10^{15}\ [\mathrm{cm}^{-3}] = 4.8 \times 10^{14} : N_{\mathrm{d.it}}\ [\mathrm{cm}^{-2}]$ to keep the ratio between molecule and trap density. Then, $\sigma_{\mathrm{d.it}}$ and $E_{\mathrm{d.it}}$ were similarly determined with bulk trap states. Finally, numerical calculation showed good fit with measured data of pentacene-based OFET even at the low temperature (Fig. 5.13c, dotted lines)

Table 5.2. The set of parameters used in the numerical simulation.

Categories	Parameters[a]	IDTBT	PBTTT	Pentacene	Unit
Device parameters	W_{G}	4.3	4.3	4.3	eV
	$W_{\mathrm{S/D}}$	4.9	4.9	4.9	eV
	ε_{i}	2.1	2.2	2.5	-
	ε_{s}	3.5	1.55	4	-
	E_{b}	0.25	0.2	0.8	eV
GDM on random sites	N_0	7.4×10^{20}	8.9×10^{20}	3×10^{21}	cm^{-3}
	σ_{i}	0.059	0.11	0.15	eV
	a	0.75	0.29	0.56	nm
	ν_0	7.05×10^{14}	2.9×10^{17}	6.76×10^{16}	s^{-1}
	B_{c}	2.735	2.735	2.735	-
Donor-like bulk trap states	$N_{\mathrm{d.bulk}}$	4×10^{14}	-	1×10^{15}	cm^{-3}
	$\sigma_{\mathrm{d.bulk}}$	0.059	-	0.15	eV
	$E_{\mathrm{d.bulk}}$	0.28	-	0.8	eV
Donor-like Interface trap states	$N_{\mathrm{d.it}}$ 258 K	-	-	8×10^{8}	cm^{-2}
	$N_{\mathrm{d.it}}$ 233 K	-	-	1.8×10^{9}	cm^{-2}
	$\sigma_{\mathrm{d.it}}$	-	-	0.15	eV
	$E_{\mathrm{d.it}}$	-	-	1.1	eV

[a] W_{G}: Work function of gate electrode, $W_{\mathrm{S/D}}$: Work function of source/drain electode, ε_{i}: dielectric constant of gate insulator, ε_{s}: dielectric constant of semiconductor, E_{b}: injection barrier from $W_{\mathrm{S/D}}$ to $\mathrm{HOMO_{max}}$, N_{d}: trap density, σ_{d}: Gaussian width of trap Gaussian DOS and E_{d}: energetic distance between intrinsic DOS and trap DOS.

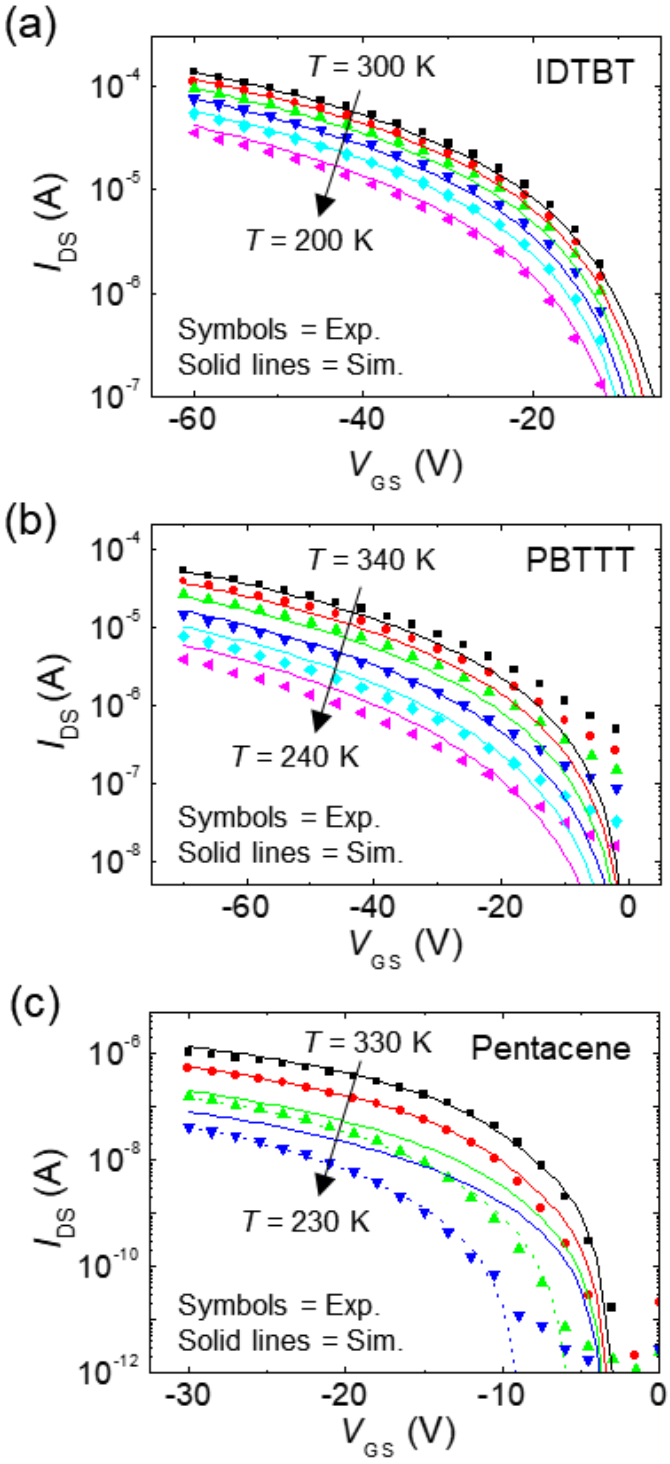

Fig. 5.13. Transfer curves of (a) IDTBT (V_{DS}= -60 V), (b) PBTTT (V_{DS}= -70 V) and (c) pentacene (V_{DS}= -2 V) based OFETs. Symbols illustrate measured data and solid lines show simulated results without interface trap states. For pentacene OFET, dotted lines for low temperatures T = 260, 230 K represent simulated results with interface trap states.

Chapter 6

Injection barrier modeling

The injection barrier E_b at metal-semiconductor junction has been widely studied as a key parameter of the charge injection in electronic devices [71]. In the ideal junction, the Schottky-Mott rule [171], [172] determine E_b by the difference between a work function of the metal electrode and the ionization energy or electron affinity of the semiconductor depending on the polarity of injected carrier. However, non-ideal factors such as the interface dipole and energetical disorder result in difficulty to extract E_b in a realistic case.

In ODSs, non-ideal factors are more remarkable at the junction with metal than inorganic crystalline semiconductors. At the metal/ODSs (M/O) junction, the interface dipole is clearly detected by photoemission spectroscopy [173]. In addition, the ambiguity of a band edge in the fully localized energetic state, i.e. Gaussian DOS leads to unclear solution of E_b [174] because the Gauss-Fermi integral cannot be solved analytically [175]. Therefore, many researchers used the onset of Gaussian DOS [174] as an alternative solution to define band edge. However, Horowitz recently proved that there are many states beyond the onset and this concept is not accurate [40].

In this chapter, we study recently developed charge-based injection barrier model at M/O junction, so-called ‘effective injection barrier’ and validated this model via numerical simulation. Also, we propose new transport-based injection barrier by using transport energy level within the GDM on random sites.

6.1 Charge-based injection barrier model

6.1.1 Effective injection barrier

To clarify E_b at M/O junction with Gaussian DOS, Jung et al. proposed the charge-based effective injection barrier E_b^{eff} by analytical solution of the hole concentration via integrating Gaussian DOS and Boltzmann distribution [41]. The analytical charge carrier density can be expressed as,

$$p = N_0 \exp\left[-\frac{1}{kT}\left\{E_F - \left(\mathrm{HOMO_{max}} + \frac{\sigma^2}{2kT}\right)\right\}\right]. \quad (6.1)$$

At the M/O junction, Fermi level E_F is aligned between metal and ODSs so that E_F in the ODSs is equivalent to E_F in the metal electrode. Then, the numerator of the exponent can be regarded as the effective injection barrier,

$$E_b^{eff} = E_F - \left(\mathrm{HOMO_{max}} + \frac{\sigma^2}{2kT}\right). \quad (6.2)$$

When Eq. (6.1) and (6.2) are combined, $p = N_0 \exp(-E_b^{eff}/kT)$ is similar with Eq. (2.4) for ideal M/O junction for inorganic semiconductors. By the E_b^{eff} we can define $\mathrm{HOMO_{edge}}$ clearly as $\mathrm{HOMO_{edge}} = \mathrm{HOMO_{max}} + \sigma^2/2kT$ that the band edge of Gaussian DOS is situated $\sigma^2/2kT$ from the maximum of Gaussian DOS. Although $\mathrm{HOMO_{onset}}$ is a common concept for $\mathrm{HOMO_{edge}} = \mathrm{HOMO_{max}} + 2\sigma$, this method does not originates from the rigorousness method. Therefore, $\mathrm{HOMO_{edge}}$ should adopt E_b^{eff} concept to calculate exact charge carrier density at the M/O junction.

6.1.2 Numerical validation by contact resistance

The role of E_b in OFETs is very important to understand contact resistance R_C that has been regarded as the biggest problem of OFETs community [24]. There were several attempt to correlate E_b and R_C of OFETs based on the device physics of conventional inorganic MOSFET e.g. schottky barrier model [176], [177]. In addition, Kim and coworkers successfully developed semi-analytical [13] and fully-analytical [119] R_C model for coplanar OFETs. They proved that R_C is a function of E_b and V_{GS}. The aim of this section is to validate E_b^{eff} in the OFETs

via comparing the semi-analytical R_C model and numerically calculated R_C by 2-D numerical simulation with E_b^{eff}.

C. –H. Kim [13] developed a semi-analytical R_C model for coplanar OFETs. He demonstrated that an origin of R_C in coplanar structure is a distinctive carrier transition zone between source and channel region and R_C can be analytically derived by the charge carrier distribution model. The hole distribution in the source p_s and the channel p_{ch} along the thickness of organic layer are derived as,

$$p_{s0} = N_v \exp\left(-\frac{E_b}{kT}\right), \tag{6.3}$$

$$p_s(y) = p_{s0}\frac{\cos^2\left(\frac{d}{y_{s0}}\right)}{\cos^2\left(\frac{d-y}{y_{s0}}\right)}, \tag{6.4}$$

$$p_{ch0} = \frac{C_i^2|V_{GS} - V_T|^2}{2\varepsilon_s kT}, \tag{6.5}$$

$$p_{ch}(y) = p_{ch0}\frac{\sin^2\left(\frac{\pi}{2}\frac{y_{ch0}}{d}\right)}{\sin^2\left(\frac{\pi}{2}\frac{y_{ch0}+y}{d}\right)}, \tag{6.6}$$

where, N_V is total density of states, E_b the injection barrier, d the thickness of the semiconductor, y the distance from organic-insulator interface along the thickness of organic layer, C_i the insulator capacitance per unit area, V_{GS} gate voltage, V_T the threshold voltage and $y_{s0} = \sqrt{2\varepsilon_s kT/q^2 p_{s0}}$ and $y_{ch0} = \sqrt{2\varepsilon_s kT/q^2 p_{ch0}}$ are characteristic distribution length for the source and the channel, respectively. A geometrical structure of analytical modeling is shown in Fig. 6.1a for coplanar structure. While p_{ch} is induced by the effect of V_{GS}, p_s is mainly determined by E_b because the source electrode screens the V_{GS} effect and the only injection can contribute to hole density in the source region. Then, the semi-analytical equation for R_C is developed as,

$$R_c = \frac{\sqrt{\varepsilon_s kT}}{q^2\mu T}\left[\int_0^d \frac{p_{ch}(y)\sqrt{p_s(y)}}{\left[\ln\left(\frac{p_{ch}(y)}{p_s(y)}\right)\right]^2}dy\right]^{-1}, \tag{6.7}$$

where ε_s is the dielectric constant of semiconductor, q is the elementary charge and μ the hole mobility. It is derived by the integral of local conductivity in the transition zone with respect to y, calculated by the average hole density. Although the E_b in Eq. (6.3) was initially defined by the onset of exponential DOS, we adopt the E_b^{eff} to consider ODSs.

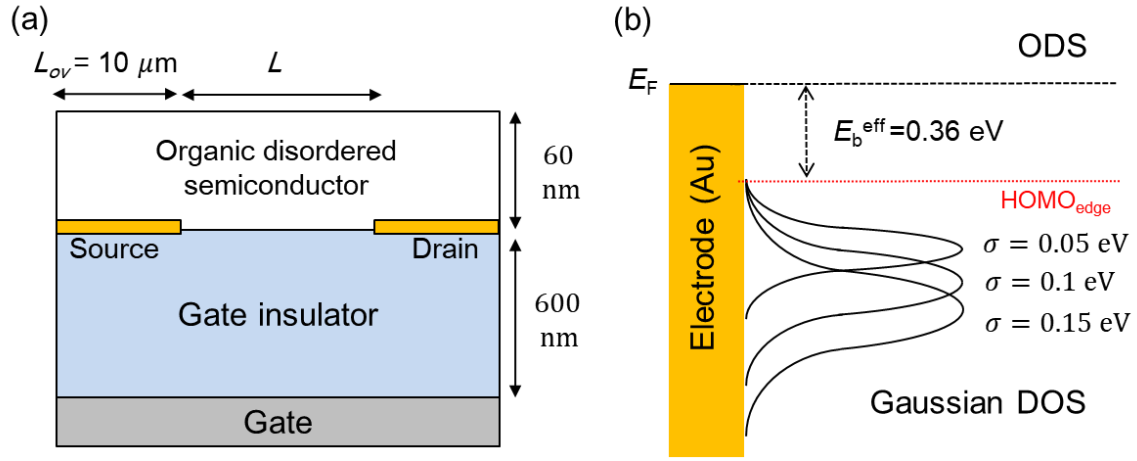

Fig.6.1. (a) Geometrical structure and (b) energetic structure at M/O junction in the numerical calculation.

The numerical modeling was conducted to validate the analytical R_C model. The TCAD modeling followed the method in Chapter 3 and the configurational and energetic structures of the simulated device are coincidence with the analytical simulation as described in Fig. 6.1. The calculation was carried out with three Gaussian widths, σ=0.05, 0.1 and 0.15 eV while E_b^{eff} keeps constant as 0.36 eV. As the band edge of Gaussian DOS was decided by $\sigma^2/2kT$ from $HOMO_{max}$, it should be lower depending on the σ (Fig. 6.1b). Although different disorders result in changing position and shape of the HOMO, the constant E_b^{eff} in numerical simulation allows the direct comparison with analytical R_C model. For the mobility in the numerical simulation, EGDM was adopted with parametrized parameters $c_1 = 7.35 \times 10^{-2}$ and $c_2 = 0.351$ in Eq. (2.17).

Transfer characteristics were initially calculated with various channel length $L = 30, 50, 60$ and $80\ \mu m$ (only $60\ \mu m$ in Fig. 6.2a). Then, R_C and charge carrier mobility μ (Fig. 6.2b and c) were extracted by transmission line method (TLM) from simulated transfer curves. Simulated transfer curves and R_C

were significantly depending on the Gaussian width; they varied 1-2 orders of magnitude with $\Delta\sigma = 0.05$ eV. This deviation originated from the mobility calculated by EGDM that increase of $\Delta\sigma = 0.05$ eV reduced mobility as much as 1-2 orders of magnitude [84]. Noted that extracted R_C is coupled with mobility [63].

Due to the σ dependent mobility, direct comparison of R_C between semi-analytical model and numerical simulation is impossible because constant mobility was considered in semi-analytical model in Eq. (6.7). To compare two models, we multiplied μ to R_C so as to exclude the effect of mobility on the contact resistance. For semi-analytical model, $\mu \times R_C$ enables to delete μ in right-hand side of Eq. (6.7). For numerical model, we can expect similar result. Interestingly, the $\mu \times R_C$ from semi-analytical model was well fitted with that from numerical simulation for low Gaussian widths, $\sigma = 0.05$ and 0.1 eV. In contrast, numerical result was highly deviated from the semi-analytical fit for $\sigma = 0.15$ eV (Fig. 6.3). This result signifies that E_b^{eff} is valid for M/O junction with low Gaussian width that is corresponding with previous result of the organic rectifying diodes [41].

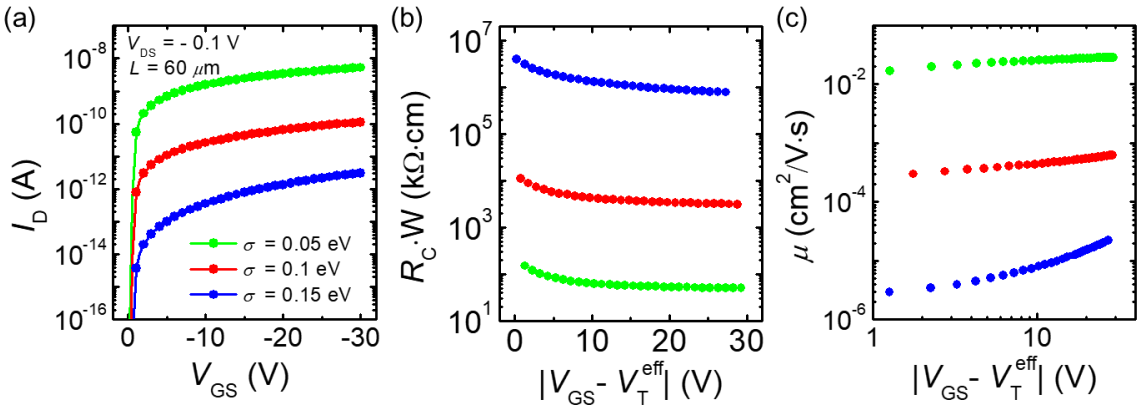

Fig.6.2. Numerically calculated (a) transfer curves, (b) width-normalized contact resistance R_C and (c) mobility for various Gaussian widths σ. Here, $\nu_0 = 1 \times 10^{13}$ 1/s was used.

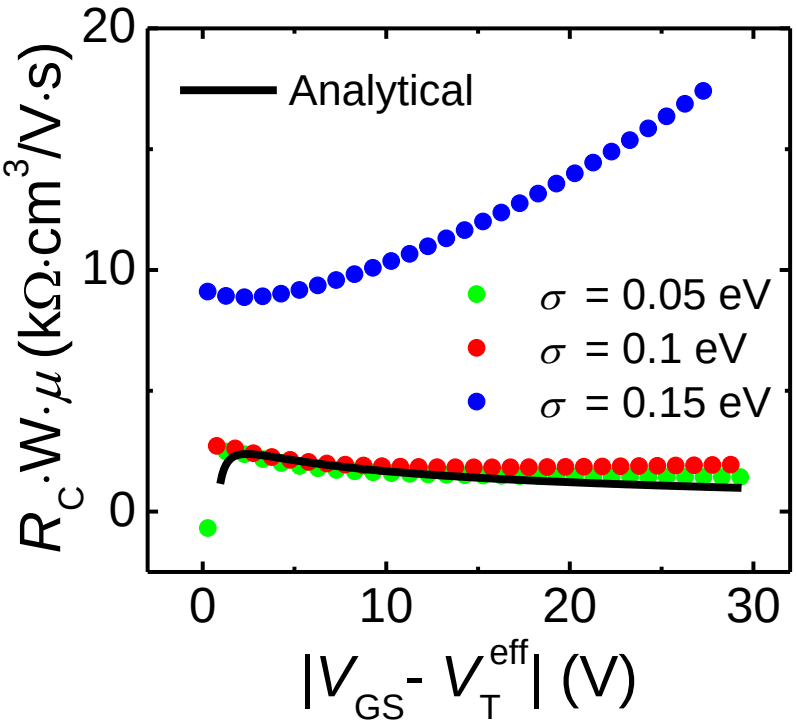

Fig.6.3. Result of multiplying $\mu \times R_C W$ of (a) numerical simulations in Fig. 6.2b and c (dotted line) and (b) semi-analytical equation in Eq. (6.7) (solid line).

6.1.3 Degenerate and non-degenerate condition.

The deviation at $\sigma = 0.15$ eV is attributed to the degenerate condition (DC) of ODS. As Horowitz [40] verified that ODS can act as a degenerate semiconductor even very low charge carrier density, the separation of non-degenerate condition (N-DC) and DC in ODSs is totally different with the inorganic crystalline semiconductors. In fact, the degree of disorder mainly determines whether ODS includes in the N-DC or DC, not by concentration of charge carrier or position of Fermi level. This phenomenon is originated from the deep band tail of Gaussian DOS with large Gaussian width. When the Gaussian broadening is significant at large σ, tail states penetrate deeply toward E_F. In this case, the Fermi-Dirac distribution (FD) function cannot be approximated by the Boltzmann distribution (BD) function (Fig. 6.4a). Therefore, ODSs belongs to DC by large σ even

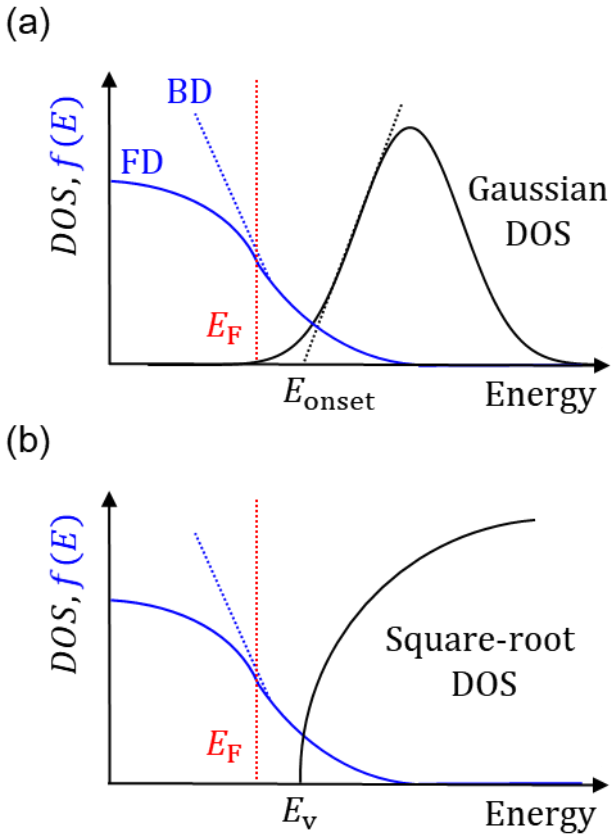

Fig.6.4. Schematic of Fermi-Dirac distribution (FD) and Boltzmann distribution (BD) functions with (a) the square-root DOS and (b) the Gaussian DOS with respect to the energy.

under low E_F. This behavior is at variance with the inorganic crystalline semiconductors that belong to the N-DC unless the E_F is very close to (few kT) or passes the band edge due to the clearly defined band edge by the valence band or conduction band (Fig. 6.4b). The analytical derivation of E_b^{eff} by charge carrier density at M/O junction (Eq. (6.1)) assumed Boltzmann distribution as well as Gaussian DOS. Therefore, E_b^{eff} is valid for the N-DC. In contrast, the DC that is strictly necessary the Fermi-Dirac distribution cannot guarantee an exact solution of the band edge by E_b^{eff}.

To visualize effective range for each DC and N-DC, the position of Fermi level with respect to the Gaussian width is mapped (Fig. 6.5). From the assumption in Fig. 6.1b, the E_F illustrates the energetic distance between the work function of electrode and $HOMO_{max}$; 0.408 eV for $\sigma = 0.05$ eV, 0.553 eV for $\sigma = 0.1$ eV and 0.794 eV for $\sigma = 0.15$ eV. Interestingly, the E_F of low Gaussian widths $\sigma = 0.05$ and 0.1 eV were larger than the equilibrium energy $E_\infty =$

σ^2/kT, whereas the E_F of large Gaussian widths $\sigma = 0.15$eV was smaller than E_∞. That is to say, $E_F > E_\infty$ indicates N-DC regime and $E_F < E_\infty$ indicates DC regime, respectively. This result is corresponding with DC and N-DC separation via the position of the occupied charge distribution with respect to the E_F [178]. The visualization of the E_F with respect to σ offers an intuitive insight of DC and N-DC via the ultra-violet photoemission spectroscopy (UPS) spectra that includes both information of E_F and σ.

We now confirmed the validity of E_b^{eff} in OFETs for N-DC condition. Although ones have believed common ODSs behaves as DC due to the large σ from UPS spectra [40], [179], the E_b^{eff} is still important to define contact property at M/O junction because of low-disordered materials. Single crystal organic semiconductor such as Rubrene exhibit small degree of disorder lower than 0.1 eV [138]. Also, recent studies in terms on the material design of donor-acceptor copolymer [1] and the fabrication process with self-assembled monolayer that increases the crystallinity of semiconductor film [63], [64] are expected to reduce Gaussian width significantly and belong to the N-DC.

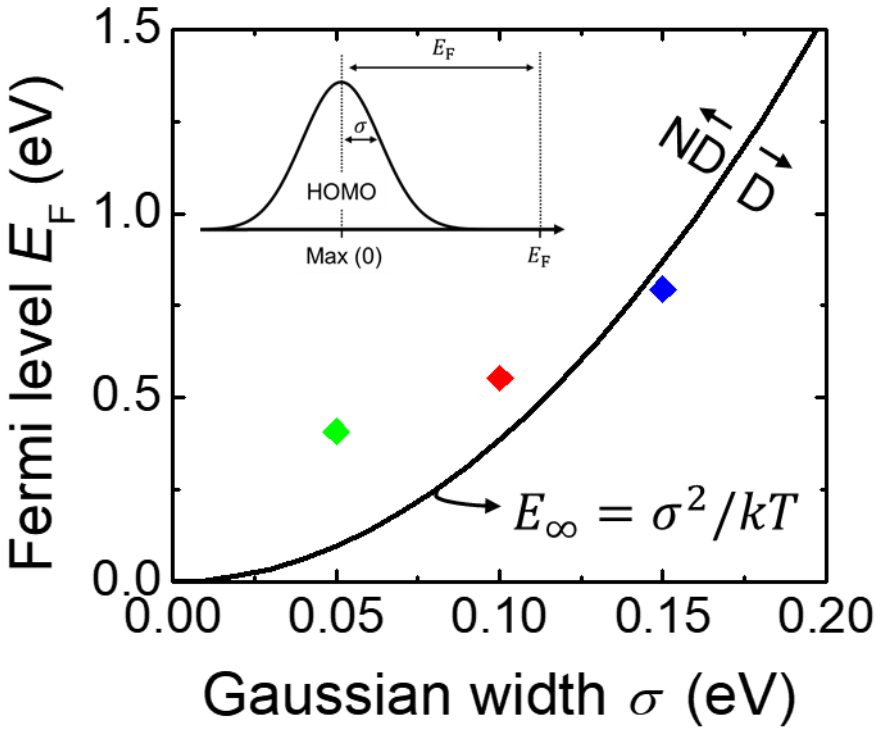

Fig.6.5. Position of Fermi level for each Gaussian width condition. Solid line illustrates the equilibrium energy that divides non-degenerate (ND) regime and degenerate (D) regime.

6.2 Transport-based injection barrier model

6.2.1 Mobility edge and transport energy

The transport-based injection barrier is mainly determined by the energy that the most charge transport takes place. For example, 'mobility edge' (ME) is a reference energy for the transport within the multiple trapping and release (MTR) model in the exponential DOS [25], [67]. The mobility edge is the transition energy from localized states to the delocalized states. According to the MTR model, trapped charge carriers in localized states can be released into the delocalized state and they contribute to the charge transport. Therefore, the transport-based injection barrier can be defined as $E_b^t = E_F$-ME.

Recently, the Gaussian DOS and GDM are regarded more appropriate physical model for ODSs than the exponential DOS and MTR model [82]. In GDM, 'transport energy' (TE, ε_t) is a reference energy that is responsible for the charge transport. TE in GDM is a similar concept with ME in MTR model so that ones can replace ME with TE [180]. The TE can be numerically calculated by Eq. (2.21). As following the parametrization process of GDM by Baranovskii in Fig. 5.3, TE is depending on various physical parameters, such as σ, N_0, a, B_C and

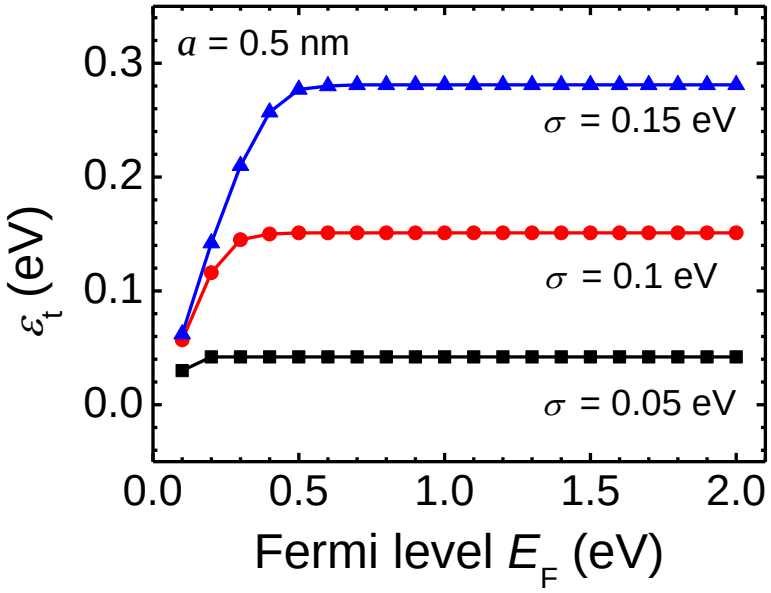

Fig.6.6. Calculated transport energy with various Gaussian width, 0.05, 0.1 and 0.15 eV via Eq. (2.21). Localization length was used 0.5 nm in the calculation.

E_F. When E_F situated far from $HOMO_{max}$, TE is constant; 0.042 eV for σ = 0.05 eV, 0.151 eV for σ = 0.1 eV and 0.281 eV for σ = 0.15 eV under a = 0.5 nm (Fig. 6.6). As TE is simply calculated, we can estimate transport-based injection barrier in Gaussian DOS by $E_b^t = E_F$-TE.

6.2.2 Dependency on the localization length

The transport-based injection barrier via TE in Gaussian DOS was regarded as an inappropriate concept to account for the injection property because of large amounts of gap states. In the initial calculation of TE with very small localization length, its position was close to the $HOMO_{max,}$ thus a lot of gap states exist between TE and E_F. However, as we described in Chapter 5, the localization length should significantly increase in order to explain high mobility of ODSs. In Fig. 6.7, we calculated both TE (ε_t) and E_b^t with respect to a based on the energetic structures of different Gaussian widths in Fig. 6.1b. As we expected, TE situates very close to the $HOMO_{max}$ when a is very low. In contrast, the position of TE shifts towards E_F (far from $HOMO_{max}$) and E_b^t reduces rapidly when large a was used. When a = 1 nm, E_b^t reaches to near 0.3 eV that is commonly used order of injection barrier in OFETs [181].

6.2.3 Dependency on the Gaussian width

The Gaussian width gives a significant effect on the E_b^t as well as the localization length. In the previous study of charge-based injection barrier via E_b^{eff} [41], the large Gaussian width can induce lowering of injection barrier due to the Gaussian broadening. This result illustrate that large Gaussian width can improve the performance in terms of the charge injection although the large Gaussian width degrades the mobility in the framework of GDM.

In this study, transport-based injection barrier with TE show similar tendency with the Gaussian width (Fig. 6.8). When σ increased from 0.025 eV to 0.3 eV, ε_t increased rapidly from 0.004 to 0.716 eV and therefore E_b^t decreased significantly from 0.996 to 0.284 eV when E_F = 1 eV and a = 0.5 nm. This results confirms that Gaussian broadening can reduce the transport-based injection barrier similar with E_b^{eff}.

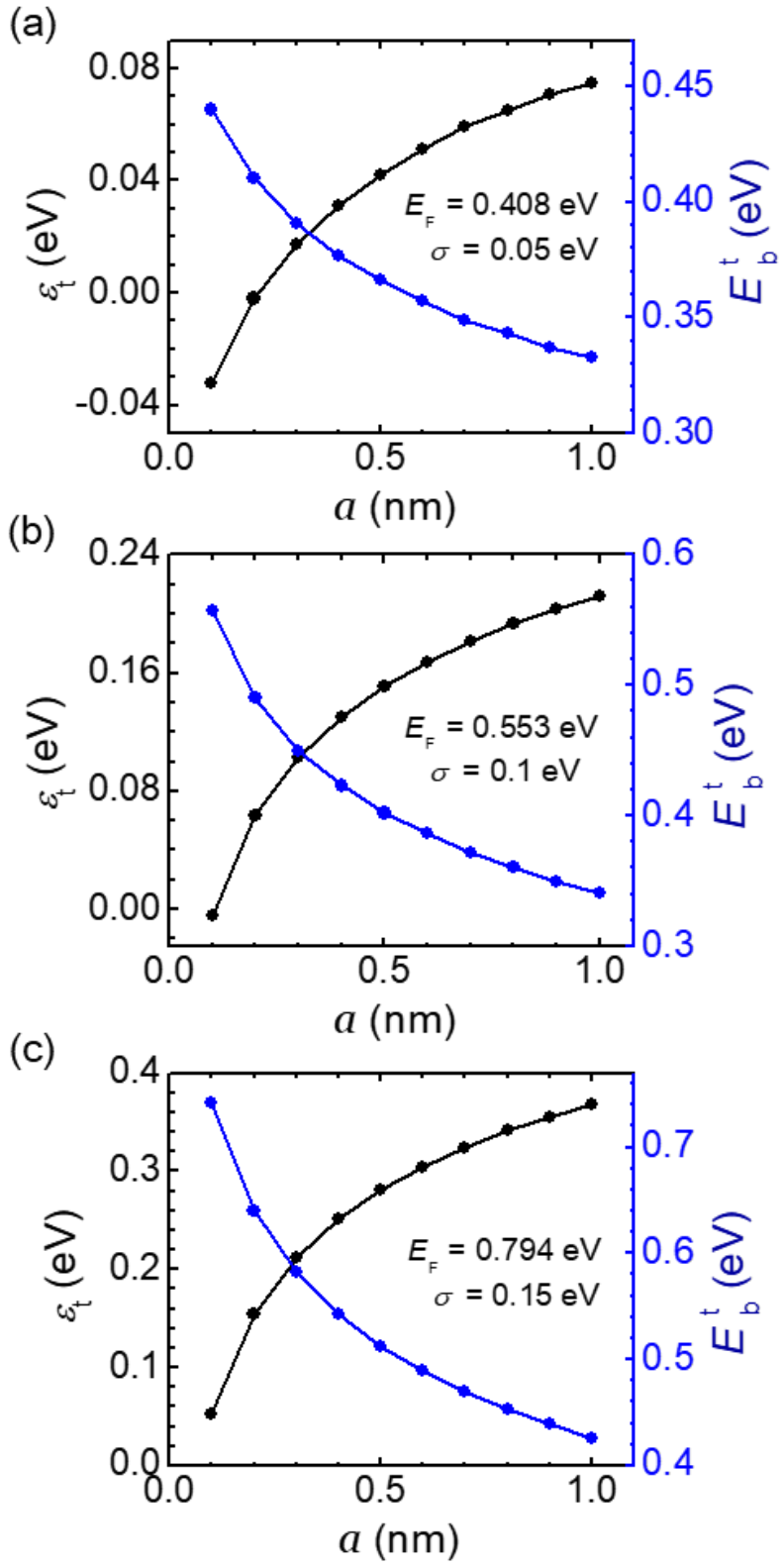

Fig.6.7. Calculated transport energy ε_t and transport-based injection barrier E_b^t with respect to a for various Gaussian width, 0.05, 0.1 and 0.15 eV. The Fermi level E_F used the energetic structures of Fig. 6.1b.

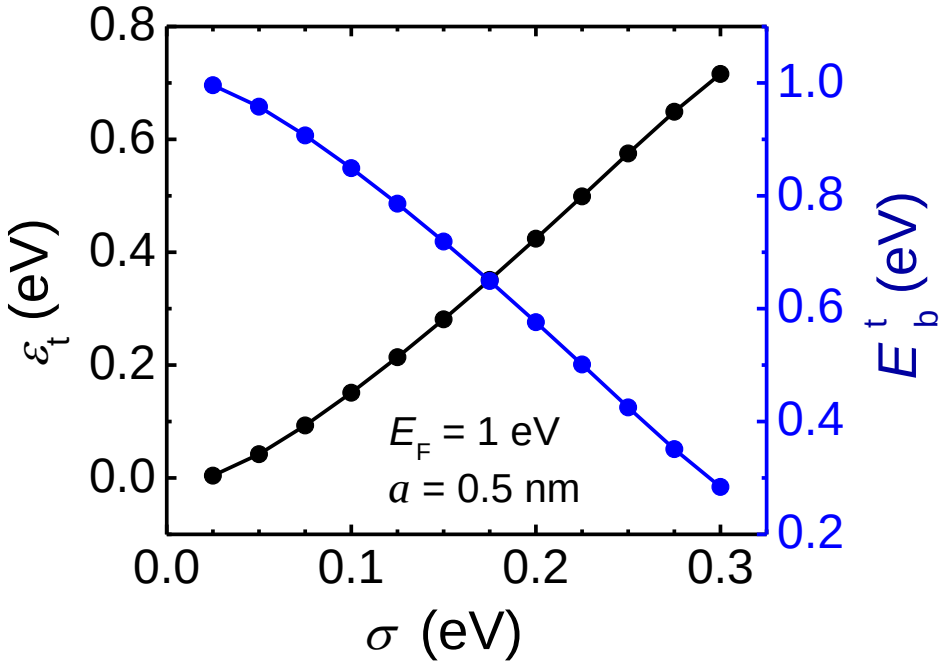

Fig.6.8. Calculated transport energy ε_t and transport-based injection barrier E_b^t with respect to σ. The calculation considered E_F = 1 eV and a = 0.5 nm.

6.3 Experimental extraction

6.3.1 Ultraviolet photoelectron spectroscopy spectra

To evaluate the injection barrier of ODSs, the energetical structure of HOMO (or LUMO) is necessary. Photoelectron spectroscopy (PS) is one of the experimental techniques to measure the shape and position of HOMO by direct observing photoelectrons that are emitted from HOMO upon irradiation [182]. Ultraviolet PS (UPS) probes the filled states, HOMO and inverse PS (IPES) probes the empty states (LUMO). In PS spectra, the quantitative evaluation of the DOS (eV^{-1} cm^{-3}) is difficult due to the complex origins of photoelectron intensity, e.g. wave function of the electronic state, photon energy, polarization direction of photon and molecular orientation [183]. However, ones can simply extract Gaussian widths and position of E_F that are essential parameters to estimate the injection barrier in Gaussian DOS.

We measured UPS spectra for the pentacene/Au thin film to evaluate the injection barrier (Fig. 6.9). Here, Au and pentacene were thermally-evaporated

on the glass substrate for 100 nm and 10 nm, respectively. As the secondary electron cutoff of bare Au and pentacene/Au films were identical, we can infer that the work function of metal and semiconductor were same. This result illustrates that the interface dipole at M/O junction was not effectively formed. If the organic semiconductor is deposited on the clean Au surface, the interface dipole induces the variation of the work function and the mismatch of vacuum-level [173]. However, if the semiconductor film deposited on the contaminated Au surface, the contamination disturbs the formation of interface dipole [179], [184]. Therefore, the equal work function of two films in Fig. 6.9a illustrates that the contamination element existed between Au and pentacene.

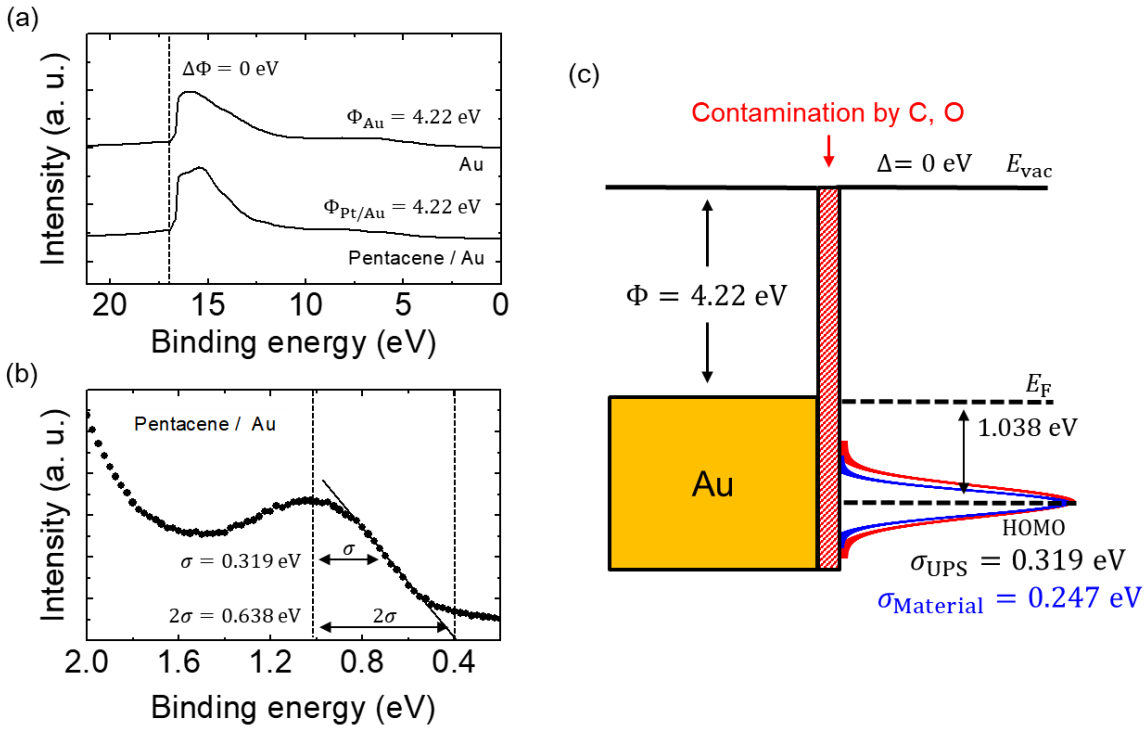

Fig.6.9. UPS spectra of (a) pentacene/Au thin film and bare Au in entire binding energy regime and (b) HOMO region of pentacene/Au thin film. Vertical dotted line in (a) represents the secondary electron cutoff and in (b) $HOMO_{max}$ and E_F of thin film. (c) Schematic of energetic structure of Au/pentacene M/O structure.

For HOMO region with low binding energy, Gaussian peak was clearly detected. The most common method to extract Gaussian width σ is finding the inflection point where the tangent at this energy meets the onset ($2\,\sigma$) at the base line. In our result, the Gaussian width σ = 0.319 eV and the tangent at this energy meets the onset 2σ = 0.638 eV precisely. Hwang and Kahn stated that the σ value directly observed from UPS must be corrected for broadening effect by UPS measurement, surface vs. bulk polarization and phonon coupling in order to extract a representative value of the hole state [179]. The width of Gaussian width can be expressed as the root mean square of each effect as follows,

$$\sigma_{\mathrm{UPS}} = \sqrt{\sigma_{\mathrm{material}}^2 + \sigma_{\mathrm{measurement}}^2} = \sqrt{\sigma_{\mathrm{material}}^2 + \left(\sigma_{\mathrm{inst}}^2 + \sigma_{\mathrm{surf}}^2 + \sigma_{\mathrm{vib}}^2\right)} \quad (6.1)$$

where σ_{UPS} is the observed width by UPS, $\sigma_{\mathrm{material}}$ the intrinsic width, σ_{inst} the broadening by instrument resolution, σ_{surf} the broadening by surface polarization and σ_{vib} the broadening by the vibrational coupling. When we adopted σ_{inst} = 0.128 eV, σ_{surf} = 0.12 eV and σ_{vib} = 0.1 eV that are common value for ODSs, we can obtain $\sigma_{\mathrm{material}}$ = 0.247 eV that is smaller than σ_{UPS}.

Based on extracted values from UPS measurement, the schematic of energetic structure at M/O junction was depicted (Fig. 6.9c). The vacuum-level is well aligned between Au and pentacene layer by the contamination. X-ray photoelectron spectroscopy (XPS) confirms that the Au surface for UPS measurement includes Fluorine F 1s at 688 eV, oxygen O 1s at 532 eV and carbon C 1s at 284 eV as the contamination, whereas the contamination was not detected in the clean Au surface (Fig. 6.10). Finally, we obtained σ = 0.247 eV and E_F from $HOMO_{max}$ = 1.038 eV that are essential information to evaluate the injection barrier at M/O junction.

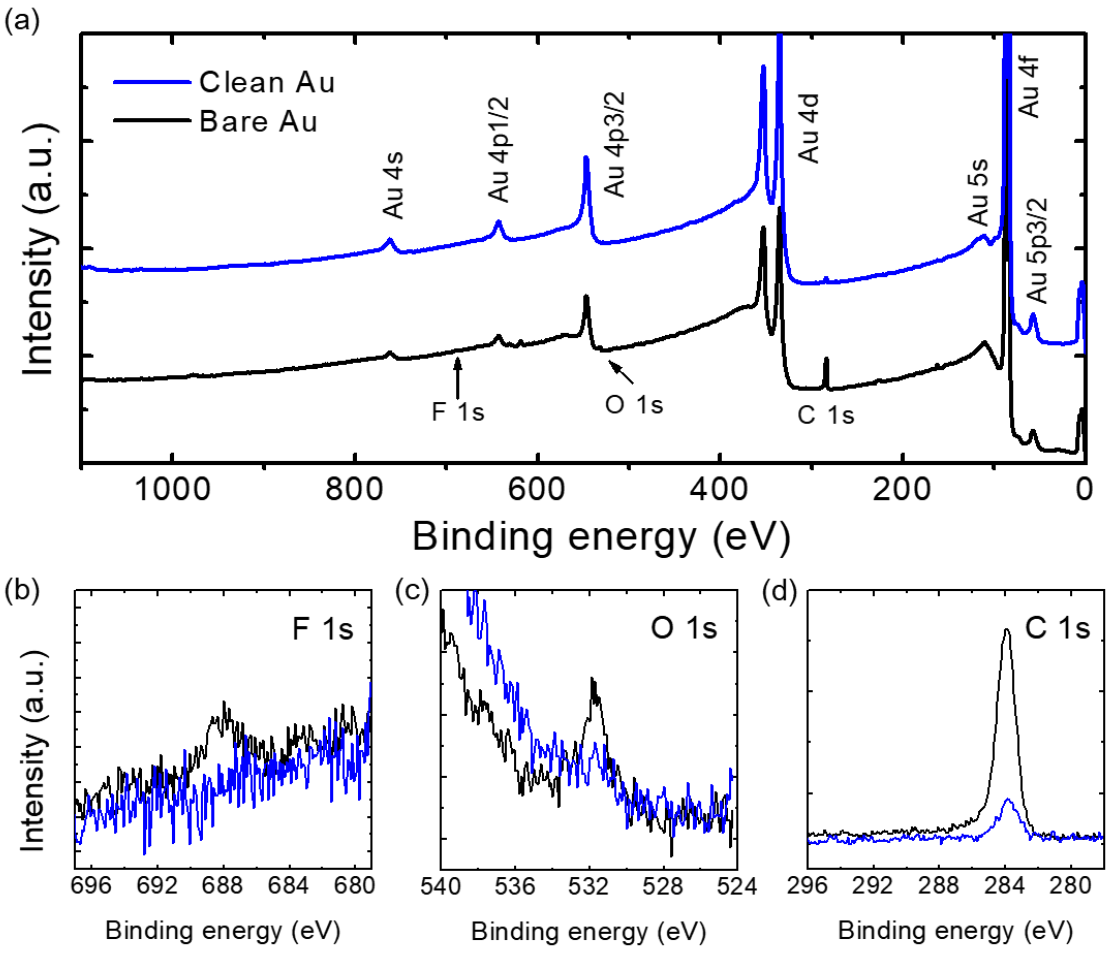

Fig.6.10. XPS spectra of (a) clean Au and bare Au in the entire binding energy regime, (b) F 1s atom, (c) O 1s atom and (d) C 1s atom. Here, bare Au denotes the equal Au surface that used for UPS measurement in Fig. 6.9.

6.3.2 Extraction of injection barriers

The transport energy was firstly calculated to get the E_b^t (Fig. 6.11). In the calculation, the parametrized parameters in Chapter 5 were adopted in Eq. (2.21) with parameters from UPS; $N_0 = 3 \times 10^{21}$ cm^{-3}, $a = 0.56$ m, $B_c = 2.735$, $\sigma = 0.247$ eV and $E_F = 1.038$ eV. At large energy, the ε_t was constant as 0.59 eV and it started to decrease from the E_F.

We compared three different E_b concepts with Gaussian DOS with variation of E_F, transport-based E_b^t, charge-based E_b^{eff} and onset-based E_b^{onset} (Fig.

6.12a). Each E_b can be calculated as $E_b^t = E_F - TE$, $E_b^{eff} = E_F - \sigma^2/2kT$ and $E_b^{onset} = E_F - 2\sigma$. Calculated results were E_b^t = 0.449 eV, E_b^{eff} = -0.178 eV and E_b^{onset} = 0.544 eV (Fig. 6.12b). Among three injection barriers, E_b^{eff} is the negative value due to the overestimated $HOMO_{edge}$. As described in Sec. 6.1.3, this Au/pentacene film belongs to the degenerate condition by $E_F < E_\infty$. Therefore, $HOMO_{edge}$ that is only effective in non-degenerate condition cannot be adopted in this large σ condition. It should be $E_F > E_\infty$ to use $HOMO_{edge}$ and E_b^{eff}, whereas E_F larger than 2.35 eV (E_∞) from $HOMO_{max}$ is too large for realistic value. E_b^t and E_b^{onset} values were quite similar but the physical basis of E_b^{onset} is lacking. Thus, E_b^t is the most appropriate way to define injection barrier in the Gaussian DOS.

Three E_b were examined with variation of E_F (Fig. 6.12c). E_b^{eff} and E_b^{onset} decreased monotonically in the all E_F regime because the band edge of these two concepts were invariable regardless of the position of E_F. However, as TE rapidly decreased with E_F in Fig. 6.11, E_b^t showed asymptotic behavior with positive values. Interestingly, only E_b^t remained positive injection barrier in all E_F regime. This illustrates that transport-based injection barrier always exist regardless of the position of E_F.

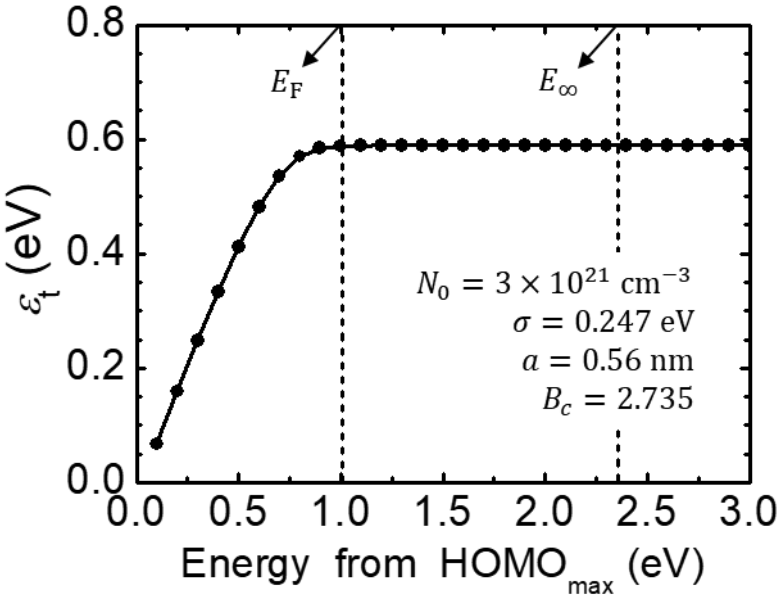

Fig.6.11. Calculated the transport energy with respect to the energy from $HOMO_{max}$. Parameters in the calculation were adopted parametrized ones for pentacene film from Chapter. 5. Vertical dotted lines illustrate the Fermi level and equilibrium energy of pentacene/Au film, respectively.

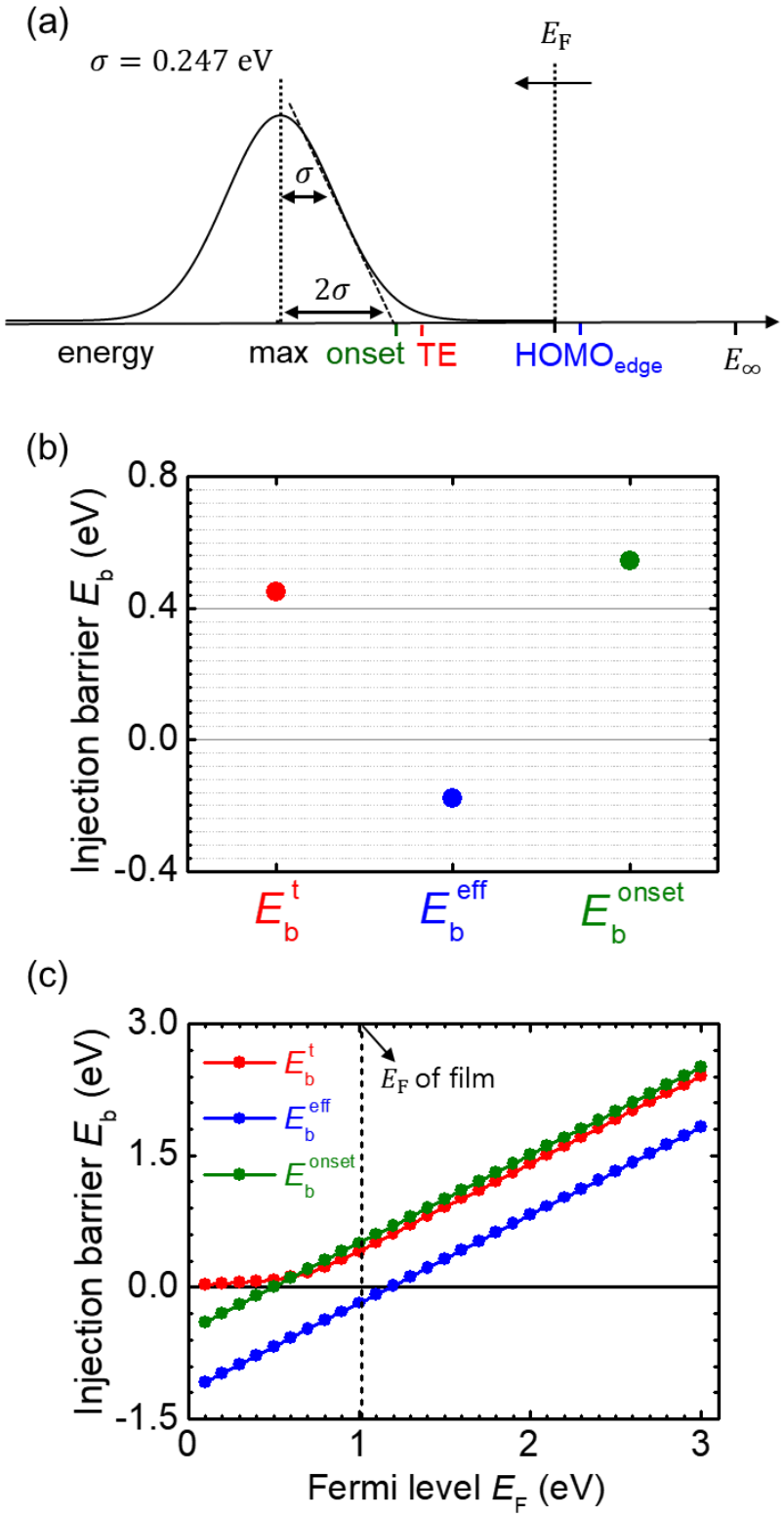

Fig.6.12. (a) Schematic of Gaussian DOS with various band edges. Calculated result of injection barriers, transport-based E_b^t, charge-based E_b^{eff} and onset-based E_b^{onset} (b) at E_F=1.038 eV and (c) entire E_F regime.

Chapter 7

Conclusion and outlook

In this thesis, Gaussian density-of-states driven numerical modeling of organic field-effect transistors have been presented. Three device parameters, threshold voltage, mobility by hopping transport and injection barrier have been investigated with 2-D numerical simulation. In this chapter, the important findings and conclusions are summarized. Also, several perspectives for future research are suggested.

We have focused on the threshold behavior to elucidate the effect of Gaussian disorder. Initially, we demonstrated that the ratio method is reliable way to extract $V_{\mathrm{T}}^{\mathrm{eff}}$ for non-linear transfer characteristics whether secondary Gaussian trap DOS presents or not. $V_{\mathrm{T.Ratio}}^{\mathrm{eff}}$ indicates precisely the onset of channel through the charge accumulation. We also discussed the mechanism of simultaneously filling of the intrinsic and the secondary Gaussian DOS, demonstrating that this simultaneous filling leads to the 'hump' shape in the transfer curve as well as the shift of the threshold voltage. In presence of trap, the Fermi level at threshold voltage corresponds to the energy at which the secondary Gaussian DOS of the traps are completely filled. The shift of threshold voltage gets greater and the power-law exponent of mobility becomes larger when the trap states are deeper, thereby these transistor parameters extracted from a transfer curve could provide information on the energy structure of a semiconductor that complements the results of physical and optical thin-film analysis. We validated the effect of double Gaussian DOS on $V_{\mathrm{T}}^{\mathrm{eff}}$ with experimental results. We demonstrated the modelling of the change in static transfer characteristics due to different gate-insulators by employing a double Gaussian DOS model. It was found that donor-like bulk traps were present as well as negative fixed charges in printed TIPS-pentacene transistors and that the MDA monomer in polymer gate

dielectric induced deeper traps compared to the DABC monomer.

Also, we proposed a correct parametrization of GDM to enable the description of a wider range of both the spatial and the energetical disorder in OFETs. We demonstrated that the GDM with the spatial disorder and the energetical disorder describes the mobility of ODSs more accurately compared to the GDM with the cubic lattice that overestimates the mobility due to the overestimated lower limit of hopping distance amounting to the intersite distance. For the accurate description of the mobility of the ODSs, the localization length and the attempt-to-escape frequency were extracted from comparison between measured and calculated Arrhenius plot. To consider wide variety of Gaussian disorder of materials, we examined donor-acceptor copolymer (IDTBT), semi-crystalline polymer (PBTTT) and small molecules (Pentacene). The localization length must be elevated up to the order of the intermolecular distance along the pi-pi conjugation and the attempt-to-escape frequency up to the range of $10^{15} - 10^{17}\ s^{-1}$, respectively. In the meantime, we clarified the role of the localization length on the parametrization by transport energy, activation energy and hopping distance via correlating both the spatial and the energetical disorder.

For the injection barrier, we have studied the charge-based and transport-based injection barrier models with the Gaussian DOS. We demonstrated that the validity of the charge-based E_b^{eff} that was derived based on the Boltzmann statistics, was depending on the Gaussian width. When the Gaussian width is small $(\sigma \leq 0.1\ \text{eV})$, the ODSs belong to the non-degenerate so that E_b^{eff} is effective. In contrast, large Gaussian width $(\sigma > 0.1\ \text{eV})$ belong to the degenerate condition due to the deep tail states and therefore E_b^{eff} is not effective. In the meantime, the transport-based E_b^{t} was proposed by the transport energy in Gaussian DOS. Although E_b^{t} was regarded as inappropriate due to the position of transport energy near $HOMO_{max}$, the correct parametrization of the localization length enables to quantify E_b^{t} in the similar order with conventional E_b models. We extracted and compared three injection barriers, E_b^{eff}, E_b^{t} and E_b^{onset} from fabricated Au/pentacene junction by UPS and XPS measurements. Only E_b^{t} remained a positive value regardless of the position of E_F.

For threshold behavior, we infer that analysis of the electrostatic charge trapping effect with various origin can be analyzed in the framework of double Gaussian DOS model. For example, the threshold voltage shift by the drain

voltage has been examined through the bias-stress effect. However, some experimental results exhibited the threshold voltage shift between the linear and saturation regime although there was not bias-stress effect. Such phenomenon can be modelled with numerical calculation with double Gaussian DOS with different drain voltage. In addition, the threshold behavior in the flexible or bended devices can be studied by extending 2-D to 3-D numerical simulation. Because bending test can cause additional trap states, the double Gaussian DOS model in 3-D numerical TCAD simulation can quantify this problem.

In addition, a correct parametrization for organic diodes should be conducted because of the strong internal electric field. In OFETs, the effect of electric field on the hopping transport was overlooked due to the large channel length. The strong electric field in diodes will affect significantly on the parametrization in the GDM with spatial and energetic disorder such as the localization length and attempt-to-escape frequency. Also, in industrial aspect, we can expect that the electronic design automate (EDA) industry for organic circuit and system will be promoted by providing a proper transport model and its parameterization within the commercial TCAD simulator. The validation of simulation program with integrated circuit emphasis (SPICE) modeling should be necessary with our TCAD device model and parametrization for complex organic systems.

Lastly, the full analytical expression of charge-based injection barrier with Fermi-Dirac statistics should be developed because ODSs are more likely to belong to the degenerate condition than the non-degenerate condition. Without the analytical solution of Gauss-Fermi integral, charge-based injection barrier and the clear definition of band edge of broad Gaussian DOS is impossible. Also, the effectiveness of the transport-based E_b^t should be examined. Different with charge-based E_b^{eff} that is already validated by the contact resistance, E_b^t was not correlated with any device parameters yet. It is essential to study device physics via E_b^t.

Appendix A

Publications

Journal articles

1. **Yongjeong Lee**, Yunho Ahn, Gilles Horowitz, Hyunjin Park, Sungjune Jung, Sungyeop Jung, and Yvan Bonnassieux, "The effect of charge trapping in double Gaussian density-of-states on the threshold behaviour of organic transistors", **(In revision in Organic Electronics)**
2. **Yongjeong Lee**, Gilles Horowitz, Andrew Plews, Ahmed Nejim, Olivier Simonetti, Louis Giraudet, Sergei D. Baranovskii, Sungjune Jung, Sungyeop Jung, and Yvan Bonnassieux, "A correct parametrization of Gaussian disorder model to account for the high mobility and disordered organic transistors", **(In revision in Physical Review Applied)**
3. **Yongjeong Lee**, Gilles Horowitz, Sungjune Jung, Sungyeop Jung, and Yvan Bonnassieux, "Validity of the effective injection barrier in organic transistors", **(In revision in Journal of Physics D: Applied Physics)**
4. Sungyeop Jung, **Yonjeong Lee**, Andrew Plews, Ahmed Nejim, Yvan Bonnassieux and Gilles Horowitz, "Effect of Gaussian Disorder on Power-Law Contact Resistance and Mobility in Organic Field-Effect Transistors" **(Accepted in IEEE Transactions of Electron Devices)**

Conference presentations

1. **Yongjeong Lee**, Gilles Horowitz, Andrew Plews, Ahmed Nejim, Olivier Simonetti, Louis Giraudet, Sergei D. Baranovskii, Sungjune Jung, Sungyeop

Jung, and Yvan Bonnassieux, ″Parametrization of Gaussian Disordered Model with Fully Spatial and Energetic Disorder for Organic Thin Film Transistors", ECS PRiME, Hawaii, USA 2020 **Invited**

2. **Yongjeong Lee**, Sungyeop Jung, Gilles Horowitz, Sungjune Jung and Yvan Bonnassieux, "Validity of the extended Gaussian disorder model for OFETs application", CAD-TFT 2019, Tarragona, Spain 2019 **Oral**
3. **Yongjeong Lee**, Yunho Ahn, Sungyeop Jung, Gilles Horowitz and Yvan Bonnassieux, "The origin of threshold voltage in OFETs", International conference of organic electronics (ICOE), Hasselt, Belgium 2019 **Poster**
4. **Yongjeong Lee,** Sungyeop Jung, Sungjune Jung, Gilles Horowitz and Yvan Bonnassieux, "Analysis of organic field effect transistor: degenerate and non-degenerate", International thin-film Transistor Conference (ITC), Naha, Okinawa, Japan 2019 **Oral**
5. **Yongjeong Lee**, Sungyeop Jung, Sungjune Jung, Gilles Horowitz and Yvan Bonnassieux, "Drain current model for coplanar OFETs with power-law mobility and contact resistance", International Meeting on Information Display (IMID), Busan, Korea 2018 **Oral**
6. **Yongjeong Lee**, Sungyeop Jung, Gilles Horowitz and Yvan Bonnassieux, "Relationship between effective injection barrier and contact resistance/field-effect mobility in coplanar organic transistor", International conference of organic electronics (ICOE), Bordeaux, France 2018 **Poster**
7. **Yongjeong Lee**, Sungyeop Jung, Gilles Horowitz and Yvan Bonnassieux, "Physically-based contact resistance modelling for coplanar organic field-effect transistors", International thin-film Transistor Conference (ITC), Guangzhou, China 2018 **Oral**
8. **Yongjeong Lee**, Sungyeop Jung, Gilles Horowitz and Yvan Bonnassieux, "Charge distribution and contact resistance model for coplanar organic field-effect transistors with Gaussian density of state", Workshop on Flexible Electronics (WFE), Tarragona, Spain 2016 **Oral**

Appendix B

Activities

Research visit

1. **Silvaco Europe Ltd., St Ives, UK, July 2019**

Hosting advisor : Dr. Ahmed Nejim and Dr. Andrew Plews

Training

1. 8th SiNANO Modelling Summer School, September 2018, Taragonna, Spain

Teaching

1. Tutoring lecture at École polytechnique, PHY559A, Analog and numerical integrated circuits, Spring 2019
2. Tutoring lecture at École polytechnique, PHY567A, Physics of semiconductor components, Spring 2018

Appendix C

Experimental details

Thermally evaporated pentacene OFETs

The device was fabricated in a bottom-gate staggered structure with various channel lengths L=30, 40, 50, 60 and 80 μm and the channel width W=1 mm. Initially, the glass substrate was cleaned by acetone, isopropanol and UV-ozone treatment and then, Al (100 nm) was thermally evaporated for the gate electrode. As for the gate insulator, polymethyl methacrylate (PMMA, MW = 120 000) solution (200mg of PMMA dissolved in 3ml of toluene for 24 hours) was spin-coated at 3000RPM/5s/60s for 600 nm on the Al/glass substrate. Lastly, pentacene (60nm) and Au (30 nm) were thermally-evaporated for the organic active layer and the source/drain electrode, successively; Evaporation rates of both pentacene and Au were globally kept at 0.01 nm/s under 1.9 e-7 mbar. All processes except the cleaning were carried out in a nitrogen glovebox.

Ink-jet printed Tips-pentacene OFETs with soluble polyimides gate insulators

Soluble polyimides gate dielectric were combinations of 5-(2,5-Dioxotetrahydrofuryl)-3-methyl-3-cyclohexene-1,2-dicar-boxylicanhydrid (DOCDA), 4,4'-(Hexafluoroisopropy-lidene)diphthalic anhydride (6FDA) monomers that contain a methyl group and a trifluoromethyl group in the backbone and 3,5-Diamino benzyl cinnamate (DABC) and 4,4'-

Methylenedibenzenamine (MDA) that contain a cinnamate group and a methylene group in the backbone. The 40 nm thick aluminum was thermally-evaporated on the glass as the gate electrode. As for the gate dielectric, soluble polyimides were spin-coated at a 3000 rpm for 1 minute and then annealed at 100 ℃ for 30 minutes. 6,13-Bis(triisopropylsilylethynyl)pentacene (TIPS-pentacene) semiconductor ink was printed into the printed bank solution ($1120\ \mu m \times 1830\ \mu m$) using the dispenser at a 50ms dispensing duration and a 5kPa discharge pressure. All printing processes were performed in the air. To crystallize TIPS-pentacene film and remove residual solvent, the sample was annealed at 70 ℃ for 10 minutes. Lastly, 40nm thick gold was thermally-evaporated for source and drain electrodes with a channel length $L = 50\ \mu m$ and width $W = 1\ mm$.

Bibliography

[1] D. Venkateshvaran *et al.*, “Approaching disorder-free transport in high-mobility conjugated polymers,” *Nature*, vol. 515, p. 384, 2014.

[2] Y. Hu, G. Li, W. Peng, and Z. Chen, “Comparing the Gate Dependence of Contact Resistance and Channel Resistance in Organic Field-Effect Transistors for Understanding the Mobility Overestimation Issue,” *IEEE Electron Device Lett.*, vol. 39, no. 3, p. 421, 2018.

[3] Y. Lee, J. Kwon, S. Jung, W. Kim, S. Baek, and S. Jung, “Reliable Inkjet Contact Metallization on Printed Polymer Semiconductors for the Fabrication of Staggered TFTs,” pp. 1–8.

[4] G. Wang, J. Swensen, D. Moses, and A. J. Heeger, “Increased mobility from regioregular poly(3-hexylthiophene) field-effect transistors,” *J. Appl. Phys.*, vol. 93, p. 6137, 2003.

[5] D. Boudinet *et al.*, “Modification of gold source and drain electrodes by self-assembled monolayer in staggered n- and p-channel organic thin film transistors,” *Org. Electron.*, vol. 11, no. 2, p. 227, 2010.

[6] C. Tanase, P. W. M. Blom, D. M. De Leeuw, and E. J. Meijer, “Charge carrier density dependence of the hole mobility in poly(p-phenylene vinylene),” *Phys. Status Solidi*, vol. 201, no. 6, p. 1236, 2004.

[7] C. A. Amorim, M. R. Cavallari, G. Santos, F. J. Fonseca, A. M. Andrade, and S. Mergulhão, “Determination of carrier mobility in MEH-PPV thin-films by stationary and transient current techniques,” *J. Non. Cryst. Solids*, vol. 358, no. 3, pp. 484–491, 2012.

[8] S. Shaked *et al.*, “Charge density and film morphology dependence of charge mobility in polymer field-effect transistors,” *Adv. Mater.*, vol. 15, no. 11, p. 913, 2003.

[9] G. Horowitz and M. E. Hajlaoui, “Grain size dependent mobility in polycrystalline organic field-effect transistors,” *Synth. Met.*, vol. 122, no. 1, p. 185, 2001.

[10] B. Stadlober, M. Zirkl, M. Beutl, G. Leising, S. Bauer-Gogonea, and S. Bauer, “High-mobility pentacene organic field-effect transistors with a high-dielectric-constant fluorinated polymer film gate dielectric,” *Appl. Phys. Lett.*, vol. 86, p. 242902, 2005.

[11] G. Horowitz, P. Lang, M. Mottaghi, and H. Aubin, “Extracting parameters from the current-voltage characteristics of organic field-effect transistors,” *Adv. Funct. Mater.*, vol. 14, no. 11, p. 1069, 2004.

[12] S. Jung, J. W. Jin, V. Mosser, Y. Bonnassieux, and G. Horowitz, “A Compact Model and Parameter Extraction Method for a Staggered OFET with Power-Law Contact Resistance and Mobility,” *IEEE Trans. Electron Devices*, vol. 66, no. 11, p. 4894, 2019.

[13] C. H. Kim, Y. Bonnassieux, G. Horowitz, and S. Member, “Charge Distribution and Contact Resistance Model for Coplanar Organic Field-Effect Transistors,” *IEEE Trans. Electron Devices*, vol. 60, no. 1, p. 280, 2013.

[14] L. Dunn and A. Dodabalapur, “Temperature dependent transient velocity and mobility studies in an organic field effect transistor,” *J. Appl. Phys.*, vol. 107, p. 113714, 2010.

[15] K. Ryu, I. Kymissis, V. Bulović, and C. G. Sodini, “Direct extraction of mobility in pentacene OFETs using C-V and I-V measurements,” *IEEE Electron Device Lett.*, vol. 26, no. 10, p. 716, 2005.

[16] C. H. Kim *et al.*, “Strongly Correlated Alignment of Fluorinated 5,11-Bis(triethylgermylethynyl)anthradithiophene Crystallites in Solution-Processed Field-Effect Transistors,” *ChemPhysChem*, vol. 15, no. 14, p. 2913, 2014.

[17] G. Horowitz, R. Hajlaoui, H. Bouchriha, R. Bourguiga, and M. Hajlaoui, “Concept of `threshold voltage’ in organic field-effect transistors,” *Adv. Mater.*, vol. 10, no. 12, p. 923, 1998.

[18] H. Shirakawa, E. J. Louis, A. G. MacDiarmid, C. K. Chiang, and A. J. Heeger, “Synthesis of electrically conducting organic polymers: Halogen derivatives of polyacetylene, (CH)x,” *J. Chem. Soc. Chem. Commun.*, no. 16, pp. 578–580, 1977.

[19] C. W. Tang, “Two-layer organic photovoltaic cell,” *Appl. Phys. Lett.*, vol.

48, no. 2, pp. 183–185, 1986.

[20] A. Tsumura, H. Koezuka, and T. Ando, “Macromolecular electronic device: Field-effect transistor with a polythiophene thin film,” *Appl. Phys. Lett.*, vol. 49, no. 18, pp. 1210–1212, 1986.

[21] C. W. Tang and S. A. Vanslyke, “Organic electroluminescent diodes,” *Appl. Phys. Lett.*, vol. 51, no. 12, pp. 913–915, 1987.

[22] The National Renewable Energy Laboratory (NREL), “Best Research-Cell Efficiency Chart,” 2020.

[23] H. Klauk, “Organic thin-film transistors,” *Chem. Soc. Rev.*, vol. 39, p. 2643, 2010.

[24] M. Waldrip, O. D. Jurchescu, D. J. Gundlach, and E. G. Bittle, “Contact Resistance in Organic Field-Effect Transistors: Conquering the Barrier,” *Adv. Funct. Mater.*, vol. 1904576, pp. 1–31, 2019.

[25] G. Horowitz, M. E. Hajlaoui, and R. Hajlaoui, “Temperature and gate voltage dependence of hole mobility in polycrystalline oligothiophene thin film transistors,” *J. Appl. Phys.*, vol. 87, no. 9, pp. 4456–4463, 2000.

[26] H. Klauk, “Will We See Gigahertz Organic Transistors?,” *Adv. Electron. Mater.*, vol. 4, no. 10, pp. 1–8, 2018.

[27] J. W. Borchert *et al.*, “Small contact resistance and high-frequency operation of flexible low-voltage inverted coplanar organic transistors,” *Nat. Commun.*, vol. 10, no. 1, pp. 1–11, 2019.

[28] M. G. Kane *et al.*, “Analog and digital circuits using organic thin-film transistors on polyester substrates,” *IEEE Electron Device Lett.*, vol. 21, no. 11, pp. 534–536, 2000.

[29] K. Myny, E. Van Veenendaal, G. H. Gelinck, J. Genoe, W. Dehaene, and P. Heremans, “An 8-bit, 40-instructions-per-second organic microprocessor on plastic foil,” *IEEE J. Solid-State Circuits*, vol. 47, no. 1, pp. 284–291, 2012.

[30] Y. Takeda *et al.*, “Fabrication of Ultra-Thin printed organic TFT CMOS logic circuits optimized for low-voltage wearable sensor applications,” *Sci. Rep.*, vol. 6, no. April, pp. 1–9, 2016.

[31] E. C. P. Smits *et al.*, “Bottom-up organic integrated circuits,” *Nature*, vol. 455, no. 7215, pp. 956–959, 2008.

[32] E. Cantatore, T. C. T. Geuns, A. F. A. Gruijthuijsen, G. H. Gelinck, S. Drews, and D. M. De Leeuw, “A 13.56MHz RFID system based on

organic transponders," *Dig. Tech. Pap. - IEEE Int. Solid-State Circuits Conf.*, vol. 42, no. 1, pp. 84–92, 2006.

[33] Plasticlogic, "Product brief, available at https://www.plasticlogic.com/," 2020. [Online]. Available: https://www.plasticlogic.com/.

[34] T. Someya, T. Sekitani, S. Iba, Y. Kato, H. Kawaguchi, and T. Sakurai, "A large-area, flexible pressure sensor matrix with organic field-effect transistors for artificial skin applications," *Proc. Natl. Acad. Sci. U. S. A.*, vol. 101, no. 27, pp. 9966–9970, 2004.

[35] T. Someya *et al.*, "Conformable, flexible, large-area networks of pressure and thermal sensors with organic transistor active matrixes," *Proc. Natl. Acad. Sci. U. S. A.*, vol. 102, no. 35, pp. 12321–12325, 2005.

[36] T. Yokotaa *et al.*, "Ultraflexible, large-area, physiological temperature sensors for multipoint measurements," *Proc. Natl. Acad. Sci. U. S. A.*, vol. 112, no. 47, pp. 14533–14538, 2015.

[37] Y. Van De Burgt, A. Melianas, S. T. Keene, G. Malliaras, and A. Salleo, "Organic electronics for neuromorphic computing," *Nat. Electron.*, vol. 1, p. 386, 2018.

[38] D. Khodagholy *et al.*, "In vivo recordings of brain activity using organic transistors," *Nat. Commun.*, vol. 4, p. 1575, 2013.

[39] Y. Kim *et al.*, "A bioinspired flexible organic artificial afferent nerve," *Science (80-.).*, vol. 360, p. 998, 2018.

[40] G. Horowitz, "Validity of the concept of band edge in organic semiconductors," *J. Appl. Phys.*, vol. 118, no. 11, p. 115502, 2015.

[41] S. Jung, C.-H. Kim, Y. Bonnassieux, and G. Horowitz, "Injection barrier at metal/organic semiconductor junctions with a Gaussian density-of-states," *J. Phys. D. Appl. Phys.*, vol. 48, no. 39, p. 395103, 2015.

[42] S. Jung, J. Kwon, S. Tokito, G. Horowitz, Y. Bonnassieux, and S. Jung, "Compact modelling and SPICE simulation for three-dimensional, inkjet-printed organic transistors, inverters and ring oscillators," *J. Phys. D. Appl. Phys.*, vol. 52, p. 444005, 2019.

[43] A. Assadi, C. Svensson, M. Wiilander, and O. Inganas, "Field-effect mobility of poly (3- hexylthiophene)," *Appl. Phys. Lett.*, vol. 53, no. 18, p. 195, 1988.

[44] H. Sirringhaus *et al.*, "Two-dimensional charge transport in conjugated polymers," *Nature*, vol. 401, pp. 685–688, 1999.

[45] I. McCulloch *et al.*, “Liquid-crystalline semiconducting polymers with high charge-carrier mobility,” *Nat. Mater.*, vol. 5, no. 4, pp. 328–333, 2006.

[46] I. Mcculloch *et al.*, “Semiconducting thienothiophene copolymers: Design, synthesis, morphology, and performance in thin-film Organic transistors,” *Adv. Mater.*, vol. 21, no. 10–11, pp. 1091–1109, 2009.

[47] J. Mei, D. H. Kim, A. L. Ayzner, M. F. Toney, and Z. Bao, “Siloxane-terminated solubilizing side chains: Bringing conjugated polymer backbones closer and boosting hole mobilities in thin-film transistors,” *J. Am. Chem. Soc.*, vol. 133, no. 50, pp. 20130–20133, 2011.

[48] H. Bronstein *et al.*, “Thieno[3,2- b]thiophene-diketopyrrolopyrrole-containing polymers for high-performance organic field-effect transistors and organic photovoltaic devices,” *J. Am. Chem. Soc.*, vol. 133, no. 10, pp. 3272–3275, 2011.

[49] W. Zhang *et al.*, “Indacenodithiophene Semiconducting Polymers for High-Performance, Air-Stable Transistors,” *J. Am. Chem. Soc.*, vol. 132, no. 1, pp. 11437–11439, 2010.

[50] X. Zhang *et al.*, “Molecular origin of high field-effect mobility in an indacenodithiophene- benzothiadiazole copolymer,” *Nat. Commun.*, vol. 4, 2013.

[51] S. Lee, B. Koo, J. Shin, E. Lee, H. Park, and H. Kim, “Effects of hydroxyl groups in polymeric dielectrics on organic transistor performance,” *Appl. Phys. Lett.*, vol. 88, no. 16, 2006.

[52] H. S. Tan, N. Mathews, T. Cahyadi, F. R. Zhu, and S. G. Mhaisalkar, “The effect of dielectric constant on device mobilities of high-performance, flexible organic field effect transistors,” *Appl. Phys. Lett.*, vol. 94, no. 26, pp. 85–88, 2009.

[53] U. Zschieschang *et al.*, “Flexible low-voltage organic transistors and circuits based on a high-mobility organic semiconductor with good air stability,” *Adv. Mater.*, vol. 22, no. 9, pp. 982–985, 2010.

[54] T. Yamamoto and K. Takimiya, “Facile synthesis of highly π-extended heteroarenes, dinaphtho[2,3-b: 2′,3′-f]chalcogenopheno[3,2-b]chalcogenophenes, and their application to field-effect transistors,” *J. Am. Chem. Soc.*, vol. 129, no. 8, pp. 2224–2225, 2007.

[55] H. Meng *et al.*, “2,6-Bis[2-(4-pentylphenyl)vinyl]anthracene: A stable and high charge mobility organic semiconductor with densely packed crystal

structure," *J. Am. Chem. Soc.*, vol. 128, no. 29, pp. 9304–9305, 2006.

[56] J. E. Anthony, J. S. Brooks, D. L. Eaton, and S. R. Parkin, "Functionalized pentacene: Improved electronic properties from control of solid-state order [20]," *J. Am. Chem. Soc.*, vol. 123, no. 38, pp. 9482–9483, 2001.

[57] C. D. Sheraw, T. N. Jackson, D. L. Eaton, and J. E. Anthony, "Functionalized pentacene active layer organic thin-film transistors," *Adv. Mater.*, vol. 15, no. 23, pp. 2009–2011, 2003.

[58] M. M. Payne, S. A. Odom, S. R. Parkin, and J. E. Anthony, "Stable, crystalline acenedithiophenes with up to seven linearly fused rings," *Org. Lett.*, vol. 6, no. 19, pp. 3325–3328, 2004.

[59] S. Subramanian, K. P. Sung, S. R. Parkin, V. Podzorov, T. N. Jackson, and J. E. Anthony, "Chromophore fluorination enhances crystallization and stability of soluble anthradithiophene semiconductors," *J. Am. Chem. Soc.*, vol. 130, no. 9, pp. 2706–2707, 2008.

[60] W. Kalb, P. Lang, M. Mottaghi, H. Aubin, G. Horowitz, and M. Wuttig, "Structure-performance relationship in pentacene/Al2O3 thin-film transistors," *Synth. Met.*, vol. 146, no. 3, pp. 279–282, 2004.

[61] S. Y. Yang, K. Shin, and C. E. Park, "The effect of gate-dielectric surface energy on pentacene morphology and organic field-effect transistor characteristics," *Adv. Funct. Mater.*, vol. 15, no. 11, pp. 1806–1814, 2005.

[62] C. M. Kang *et al.*, "1 GHz Pentacene Diode Rectifiers Enabled by Controlled Film Deposition on SAM-Treated Au Anodes," *Adv. Electron. Mater.*, vol. 2, no. 2, pp. 1–7, 2016.

[63] C. H. Kim *et al.*, "Decoupling the Effects of Self-Assembled Monolayers on Gold, Silver, and Copper Organic Transistor Contacts," *Adv. Mater. Interfaces*, vol. 2, no. 2, pp. 1–9, 2015.

[64] J. W. Ward *et al.*, "Tailored interfaces for self-patterning organic thin-film transistors," *J. Mater. Chem.*, vol. 22, no. 36, pp. 19047–19053, 2012.

[65] P. W. Anderson, "Absence of diffusion in certain random lattices," *Phys. Rev.*, vol. 109, no. 5, pp. 1492–1505, 1958.

[66] M. C. J. M. Vissenberg and M. Matters, "Theory of the field-effect mobility in amorphous organic transistors," *Phys. Rev. B*, vol. 57, no. 20, p. 12964, 1998.

[67] G. Horowitz, R. Hajlaoui, and P. Delannoy, "Temperature Dependence of the Field-Effect Mobility of Sexithiophene. Determination of the Density

of Traps," *J. Phys. III Fr.*, vol. 5, p. 3555, 1995.

[68] H. Bässler, "Charge Transport in Disordered Organic Photoconductors a Monte Carlo Simulation Study," *Phys. Status Solidi B*, vol. 175, no. 1, p. 15, 1993.

[69] C. Tanase, E. J. Meijer, P. W. M. Blom, and D. M. de Leeuw, "Unification of the hole transport in polymeric field-effect transistors and light-emitting diodes," *Phys. Rev. Lett.*, vol. 91, no. 21, pp. 1–4, 2003.

[70] N. Tessler and Y. Roichman, "Amorphous organic molecule/polymer diodes and transistors - Comparison between predictions based on Gaussian or exponential density of states," *Org. Electron. physics, Mater. Appl.*, vol. 6, no. 5–6, pp. 200–210, 2005.

[71] S. M. SZE and K. K. Ng, *Physics of Semiconductor Devices*. Wiley-Interscience, 2006.

[72] A. Ortiz-Conde, F. J. García Sánchez, J. J. Liou, A. Cerdeira, M. Estrada, and Y. Yue, "A review of recent MOSFET threshold voltage extraction methods," *Microelectron. Reliab.*, vol. 42, no. 4–5, pp. 583–596, 2002.

[73] V. Mosser, "Threshold Voltage Extraction Method in Field- Effect Devices with Power-Law Dependence of Mobility on Carrier Density," no. May, 2016.

[74] L. Giraudet and O. Simonetti, "Threshold voltage and turn-on voltage in organic transistors: Sensitivity to contact parasitics," *Org. Electron.*, vol. 12, no. 1, pp. 219–225, 2011.

[75] C. Reese and Z. Bao, "Detailed characterization of contact resistance, gate-bias-dependent field-effect mobility, and short-channel effects with microscale elastomeric single-crystal field-effect transistors," *Adv. Funct. Mater.*, vol. 19, no. 5, p. 763, 2009.

[76] M. Tsuno, M. Suga, M. Tanaka, K. Shibahara, M. Miura-Mattausch, and M. Hirose, "Physically-based threshold voltage determination for MOSFET's of all gate lengths," *IEEE Trans. Electron Devices*, vol. 46, no. 7, pp. 1429–1434, 1999.

[77] S. Jung, C. H. Kim, Y. Bonnassieux, and G. Horowitz, "Fundamental insights into the threshold characteristics of organic field-effect transistors," *J. Phys. D. Appl. Phys.*, vol. 48, no. 3, pp. 2–5, 2015.

[78] D. Braga and G. Horowitz, "Subthreshold regime in rubrene single-crystal organic transistors," no. November 2008, pp. 193–201, 2009.

[79] S. Jung, C.-H. Kim, Y. Bonnassieux, and G. Horowitz, “Fundamental insights into the threshold characteristics of organic field-effect transistors,” *J. Phys. D. Appl. Phys.*, vol. 48, no. 3, p. 035106, 2015.

[80] M. S. Shur, H. C. Slade, M. D. Jacunski, A. A. Owusu, and T. Ytterdal, “SPICE models for amorphous silicon and polysilicon thin film transistors,” *J. Electrochem. Soc.*, vol. 144, no. 8, pp. 2833–2839, 1997.

[81] P. G. Le Comber and E. Spear, “Electronic transport in amorphous silicon films,” *Phys. Rev. Lett.*, vol. 25, no. 8, pp. 509–511, 1970.

[82] S. D. Baranovskii, “Theoretical description of charge transport in disordered organic semiconductors,” *Phys. Status Solidi*, vol. 251, no. 3, p. 487, 2014.

[83] R. Coehoorn, W. F. Pasveer, P. A. Bobbert, and M. A. J. Michels, “Charge-carrier concentration dependence of the hopping mobility in organic materials with Gaussian disorder,” *Phys. Rev. B - Condens. Matter Mater. Phys.*, vol. 72, no. 15, p. 155206, 2005.

[84] W. F. Pasveer *et al.*, “Unified description of charge-carrier mobilities in disordered semiconducting polymers,” *Phys. Rev. Lett.*, vol. 94, no. 20, p. 206601, 2005.

[85] “Atlas User’s Manual,” SILVACO International, Santa Clara, CA, 2016.

[86] “SETFOS Simulation software Setfos version 4,” Fluxim AG, Switzerland, 2019.

[87] J. O. Oelerich, D. Huemmer, and S. D. Baranovskii, “How to find out the density of states in disordered organic semiconductors,” *Phys. Rev. Lett.*, vol. 108, no. 22, pp. 1–5, 2012.

[88] S. D. Baranovskii, “Mott Lecture: Description of Charge Transport in Disordered Organic Semiconductors: Analytical Theories and Computer Simulations,” *Phys. Status Solidi Appl. Mater. Sci.*, vol. 215, no. 12, p. 1700676, 2018.

[89] B. I. Shklovskii, “Hopping Conduction in Semiconductors Subjected To a Strong Electric Field.,” *Sov Phys Semicond*, vol. 6, no. 12, p. 1964, 1973.

[90] S. Marianer and B. I. Shklovskii, “Effective temperature ofhopping electrons in a strong electric field S.,” *Phys. Rev. B*, vol. 46, no. 20, p. 13100, 1992.

[91] S. D. Baranovskii, T. Faber, F. Hensel, and P. Thomas, “The applicability of the transport-energy concept to various disordered materials,” *J. Phys.*

Condens. Matter, vol. 9, no. 13, p. 2699, 1997.

[92] J. O. Oelerich, F. Jansson, A. V. Nenashev, F. Gebhard, and S. D. Baranovskii, "Energy position of the transport path in disordered organic semiconductors," *J. Phys. Condens. Matter*, vol. 26, no. 25, p. 255801, 2014.

[93] Y. Roichman and N. Tessler, "Generalized Einstein relation for disordered semiconductors - Implications for device performance," *Appl. Phys. Lett.*, vol. 80, no. 11, p. 1948, 2002.

[94] S. D. Baranovskii, H. Cordes, F. Hensel, and G. Leising, "Charge-carrier transport in disordered organic solids," *Phys. Rev. B*, vol. 62, no. 12, p. 7934, 2000.

[95] O. Rubel, S. D. Baranovskii, P. Thomas, and S. Yamasaki, "Concentration dependence of the hopping mobility in disordered organic solids," *Phys. Rev. B*, vol. 69, no. 1, p. 014206, 2004.

[96] V. I. Arkhipov, P. Heremans, E. V. Emelianova, G. J. Adriaenssens, and H. Bässler, "Charge carrier mobility in doped disordered organic semiconductors," *J. Non. Cryst. Solids*, vol. 338–340, no. 1 SPEC. ISS., p. 603, 2004.

[97] H. Sirringhaus, "Reliability of organic field-effect transistors," *Adv. Mater.*, vol. 21, no. 38–39, pp. 3859–3873, 2009.

[98] B. J. Veres, S. D. Ogier, S. W. Leeming, and D. C. Cupertino, "Low- k Insulators as the Choice of Dielectrics in Organic Field-Effect Transistors," *Adv. Funct. Mater.*, no. 3, pp. 199–204, 2003.

[99] S. J. Zilker, C. Detcheverry, E. Cantatore, and D. M. De Leeuw, "Bias stress in organic thin-film transistors and logic gates," *Appl. Phys. Lett.*, vol. 79, no. 8, pp. 1124–1126, 2001.

[100] H. W. Zan and S. C. Kao, "The effects of drain-bias on the threshold voltage instability in organic TFTs," *IEEE Electron Device Lett.*, vol. 29, no. 2, pp. 155–157, 2008.

[101] A. R. Brown, C. P. Jarrett, D. M. de Leeuw, and M. Matters, "Field-effect transistors made from solution-processed organic semiconductors," *Synth. Met.*, vol. 88, no. 1, pp. 37–55, 1997.

[102] J. B. Chang and V. Subramanian, "Effect of active layer thickness on bias stress effect in pentacene thin-film transistors," *Appl. Phys. Lett.*, vol. 88, no. 23, p. 233513, 2006.

[103] S. Scheinert and G. Paasch, “Influence of the carrier density in disordered organics with Gaussian density of states on organic field-effect transistors,” *J. Appl. Phys.*, vol. 115, no. 4, 2014.

[104] F. Hain, M. Graef, B. Iñíguez, and A. Kloes, “Charge based, continuous compact model for the channel current in organic thin-film transistors for all regions of operation,” *Solid. State. Electron.*, vol. 133, pp. 17–24, 2017.

[105] G. Horowitz and P. Delannoy, “An analytical model for organic-based thin-film transistors,” *J. Appl. Phys.*, vol. 70, pp. 469–475, 1991.

[106] C. Erlen and P. Lugli, “Analytical model of trapping effects in organic thin-film transistors,” *IEEE Trans. Electron Devices*, vol. 56, no. 4, pp. 546–552, 2009.

[107] S. Scheinert, G. Paasch, M. Schrödner, H. K. Roth, S. Sensfuß, and T. Doll, “Subthreshold characteristics of field effect transistors based on poly(3-dodecylthiophene) and an organic insulator,” *J. Appl. Phys.*, vol. 92, no. 1, pp. 330–337, 2002.

[108] S. Scheinert, K. P. Pernstich, B. Batlogg, and G. Paasch, “Determination of trap distributions from current characteristics of pentacene field- effect transistors with surface modified gate oxide,” *J. Appl. Phys.*, vol. 102, p. 104503, 2007.

[109] A. R. Völkel, R. A. Street, and D. Knipp, “Carrier transport and density of state distributions in pentacene transistors,” *Phys. Rev. B*, vol. 66, no. 19, p. 195336, 2002.

[110] R. A. Street, D. Knipp, and A. R. Völkel, “Hole transport in polycrystalline pentacene transistors,” *Appl. Phys. Lett.*, vol. 80, no. 9, pp. 1658–1660, 2002.

[111] L. Li, M. Debucquoy, J. Genoe, and P. Heremans, “A compact model for polycrystalline pentacene thin-film transistor,” *J. Appl. Phys.*, vol. 107, no. 2, pp. 2–5, 2010.

[112] S. Olthof *et al.*, “Ultralow doping in organic semiconductors: Evidence of trap filling,” *Phys. Rev. Lett.*, vol. 109, no. 17, pp. 1–5, 2012.

[113] Y. Y. Yimer, P. A. Bobbert, and R. Coehoorn, “Charge transport in disordered organic host-guest systems: Effects of carrier density and electric field,” *J. Phys. Condens. Matter*, vol. 20, no. 33, 2008.

[114] G. Zuo, Z. Li, O. Andersson, H. Abdalla, E. Wang, and M. Kemerink, “Molecular Doping and Trap Filling in Organic Semiconductor Host-

Guest Systems," *J. Phys. Chem. C*, vol. 121, no. 14, pp. 7767–7775, 2017.

[115] M. Schwarze *et al.*, "Molecular parameters responsible for thermally activated transport in doped organic semiconductors," *Nat. Mater.*, vol. 18, no. 3, pp. 242–248, 2019.

[116] V. Mosser, D. Seron, and Y. Haddab, "Threshold voltage extraction method in field-effect devices with power-law dependence of mobility on carrier density," *IEEE Int. Conf. Microelectron. Test Struct.*, vol. 2015-May, pp. 122–125, 2015.

[117] S. Jung, J. W. Jin, V. Mosser, Y. Bonnassieux, and G. Horowitz, "A Compact Model and Parameter Extraction Method for a Staggered OFET With Power-Law Contact Resistance and Mobility," *IEEE Trans. Electron Devices*, vol. 66, no. 11, p. 4894, 2019.

[118] C. Liu *et al.*, "A unified understanding of charge transport in organic semiconductors: The importance of attenuated delocalization for the carriers," *Mater. Horizons*, vol. 4, no. 4, pp. 608–618, 2017.

[119] C. H. Kim and G. Horowitz, "Toward a fully analytical contact resistance expression in organic transistors," *Materials (Basel).*, vol. 12, p. 1169, 2019.

[120] N. Björklund, F. S. Pettersson, D. Tobjörk, and R. Österbacka, "Controlling the turn-on-voltage in low-voltage Al2O3 organic transistors with mixed self-assembled monolayers," *Synth. Met.*, vol. 161, no. 9–10, pp. 743–747, 2011.

[121] S. Hong, J. Choi, and Y. Kim, "Degraded OFF-state current of organic thin-film transistor and annealing effect," *IEEE Trans. Electron Devices*, vol. 55, no. 12, pp. 3602–3604, 2008.

[122] A. Wang, I. Kymissis, V. Bulović, and A. I. Akinwande, "Tunable threshold voltage and flatband voltage in pentacene field effect transistors," *Appl. Phys. Lett.*, vol. 89, no. 11, p. 112109, 2006.

[123] A. Wang, I. Kymissis, V. Bulović, and A. I. Akinwande, "Engineering density of semiconductor-dielectric interface states to modulate threshold voltage in OFETs," *IEEE Trans. Electron Devices*, vol. 53, no. 1, pp. 9–13, 2006.

[124] L. Kergoat *et al.*, "Tuning the threshold voltage in electrolyte-gated organic field-effect transistors," *Proc. Natl. Acad. Sci.*, vol. 109, no. 22, pp. 8394–8399, 2012.

[125] C. H. Kim, O. Yaghmazadeh, D. Tondelier, Y. Bin Jeong, Y.

Bonnassieux, and G. Horowitz, “Capacitive behavior of pentacene-based diodes: Quasistatic dielectric constant and dielectric strength,” *J. Appl. Phys.*, vol. 109, no. 8, p. 083710, 2011.

[126] R. C. Powell and R. G. Kepler, “Evidence for long-range exciton-impurity interaction in tetracene-doped anthracene crystals,” *Phys. Rev. Lett.*, vol. 22, no. 13, pp. 636–639, 1969.

[127] J. Northrup and M. Chabinyc, “Gap states in organic semiconductors: Hydrogen- and oxygen-induced states in pentacene,” *Phys. Rev. B*, vol. 68, no. 4, p. 041202, 2003.

[128] L. Tsetseris and S. T. Pantelides, “Intercalation of oxygen and water molecules in pentacene crystals: First-principles calculations,” *Phys. Rev. B*, vol. 75, no. 15, p. 153202, 2007.

[129] Y. Xu *et al.*, “Modeling of static electrical properties in organic field-effect transistors,” *J. Appl. Phys.*, vol. 110, p. 014510, 2011.

[130] H. Park *et al.*, “Low-Temperature Solution-Processed Soluble Polyimide Gate Dielectrics: From Molecular-Level Design to Electrically Stable and Flexible Organic Transistors,” *ACS Appl. Mater. Interfaces*, vol. 11, no. 49, pp. 45949–45958, 2019.

[131] C. Ucurum, H. Goebel, F. A. Yildirim, W. Bauhofer, and W. Krautschneider, “Hole trap related hysteresis in pentacene field-effect transistors,” *J. Appl. Phys.*, vol. 104, no. 8, p. 084501, 2008.

[132] Y. Baek *et al.*, “Fluorinated polyimide gate dielectrics for the advancing the electrical stability of organic field-effect transistors,” *ACS Appl. Mater. Interfaces*, vol. 6, no. 17, pp. 15209–15216, 2014.

[133] X. Gao and Z. Zhao, “High mobility organic semiconductors for field-effect transistors,” *Sci. China Chem.*, vol. 58, no. 6, p. 947, 2015.

[134] J. O. Oelerich, A. V. Nenashev, A. V. Dvurechenskii, F. Gebhard, and S. D. Baranovskii, “Field dependence of hopping mobility: Lattice models against spatial disorder,” *Phys. Rev. B*, vol. 96, no. 19, p. 195208, 2017.

[135] A. V. Nenashev, J. O. Oelerich, A. V. Dvurechenskii, F. Gebhard, and S. D. Baranovskii, “Fundamental characteristic length scale for the field dependence of hopping charge transport in disordered organic semiconductors,” *Phys. Rev. B*, vol. 96, no. 3, p. 035204, 2017.

[136] V. Podzorov, S. E. Sysoev, E. Loginova, V. M. Pudalov, and M. E. Gershenson, “Single-crystal organic field effect transistors with the hole

mobility ~8 cm2/Vs," *Appl. Phys. Lett.*, vol. 83, no. 17, p. 3504, 2003.

[137] E. G. Bittle, J. I. Basham, T. N. Jackson, O. D. Jurchescu, and D. J. Gundlach, "Mobility overestimation due to gated contacts in organic field-effect transistors," *Nat. Commun.*, vol. 7, p. 10908, 2016.

[138] Y. Hu, "Direct Observation of the Dipole-Induced Energetic Disorder in Rubrene Single-Crystal Transistors by Scanning Kelvin Probe Microscopy," *J. Phys. chmeistry Lett.*, vol. 9, p. 2869, 2018.

[139] S. Machida *et al.*, "Highest-Occupied-Molecular-Orbital Band Dispersion of Rubrene Single Crystals as Observed by Angle-Resolved Ultraviolet Photoelectron Spectroscopy," *Phys. Rev. Lett.*, vol. 104, p. 156401, 2010.

[140] H. H. Fong and S. K. So, "Effects of tertiary butyl substitution on the charge transporting properties of rubrene-based films," *Chem. Phys.*, vol. 298, p. 119, 2004.

[141] V. Lemaur, J. Cornil, R. Lazzaroni, H. Sirringhaus, D. Beljonne, and Y. Olivier, "Resilience to Conformational Fluctuations Controls Energetic Disorder in Conjugated Polymer Materials: Insights from Atomistic Simulations," *Chem. Mater.*, vol. 31, p. 6889, 2019.

[142] J. Zhou, Y. C. Zhou, J. M. Zhao, C. Q. Wu, X. M. Ding, and X. Y. Hou, "Carrier density dependence of mobility in organic solids: A Monte Carlo simulation," *Phys. Rev. B - Condens. Matter Mater. Phys.*, vol. 75, no. 15, p. 153201, 2007.

[143] N. Lu, L. Li, and M. Liu, "Polaron effect and energetic disorder dependence of Seebeck coefficient in organic transistors," *Org. Electron.*, vol. 16, pp. 113–117, 2015.

[144] S. Barard, "Time-of-Flight Charge Transport Studies on Triarylamine and Thiophene Based Polymers," 2009.

[145] A. Vollmer *et al.*, "The effect of oxygen exposure on pentacene electronic structure," vol. 343, pp. 339–343, 2005.

[146] S. Yogev, E. Halpern, R. Matsubara, M. Nakamura, and Y. Rosenwaks, "Direct measurement of density of states in pentacene thin film transistors," *Phys. Rev. B - Condens. Matter Mater. Phys.*, vol. 84, no. 16, pp. 1–8, 2011.

[147] H. L. Kwok, "Hole Mobility in Structurally-Different Pentacene Field-Sffect Transistors," *ECS Trans.*, vol. 3, p. 263, 2006.

[148] I. G. Hill, J. Hwang, A. Kahn, C. Huang, J. E. McDermott, and J.

Schwartz, “Energy level alignment between 9-phosphonoanthracene self-assembled monolayers and pentacene,” *Appl. Phys. Lett.*, vol. 90, no. 1, pp. 9–11, 2007.

[149] S. Hood, N. Zarrabi, P. Meredith, I. Kassal, and A. Armin, “Measuring Energetic Disorder in Organic Semiconductors Using the,” *J. Phys. chmeistry Lett.*, vol. 10, p. 3863, 2019.

[150] W. D. Gill, “Drift mobilities in amorphous charge-transfer complexes of trinitrofluorenone and poly-n-vinylcarbazole,” *J. Appl. Phys.*, vol. 43, no. 12, p. 5033, 1972.

[151] P. M. Borsenberger, E. H. Magin, M. Der Van Auweraer, and F. C. De Schryver, “The role of disorder on charge transport in molecularly doped polymers and related materials,” *Phys. Status Solidi*, vol. 140, no. 1, p. 9, 1993.

[152] C. Tanase, P. W. M. Blom, D. M. De Leeuw, and E. J. Meijer, “Charge carrier density dependence of the hole mobility in poly(p-phenylene vinylene),” *Phys. Status Solidi Appl. Res.*, vol. 201, no. 6, p. 1236, 2004.

[153] H. Bässler, “Localized states and electronic transport in single component organic solids with diagonal disorder,” *Phys. Status Solidi*, vol. 107, no. 1, p. 9, 1981.

[154] J.-L. Bredas, D. Beljonne, V. Coropceanu, and J. Cornil, “Charge-Transfer and Energy-Transfer Processes in π-Conjugated Oligomers and Polymers: A Molecular Picture Jean-Luc,” *Chem. Rev.*, vol. 104, p. 4971, 2004.

[155] A. Miller and E. Abrahams, “Impurity conduction at low concentrations,” *Phys. Rev.*, vol. 120, no. 3, pp. 745–755, 1960.

[156] V. Ambegaokar, B. I. Halperin, and J. S. Langer, “Hopping conductivity in disordered systems,” *Phys. Rev. B*, vol. 4, no. 8, p. 2612, 1971.

[157] Z. G. Yu, D. L. Smith, A. Saxena, R. L. Martin, and A. R. Bishop, “Molecular geometry fluctuation model for the mobility of conjugated polymers,” *Phys. Rev. Lett.*, vol. 84, no. 4, p. 721, 2000.

[158] A. V Nenashev, J. O. Oelerich, and S. D. Baranovskii, “Theoretical tools for the description of charge transport in disordered organic semiconductors.,” *J. Phys. Condens. Matter*, vol. 27, no. 9, p. 093201, 2015.

[159] D. M. DeLongchamp *et al.*, “High carrier mobility polythiophene thin films: Structure determination by experiment and theory,” *Adv. Mater.*, vol. 19, no. 6, pp. 833–837, 2007.

[160] R. B. Campbell, J. Monteath Robertson, and J. Trotter, “The crystal and molecular structure of pentacene,” *Acta cryst.*, vol. 14, p. 705, 1961.

[161] W. H. Lee *et al.*, “Surface-Directed Molecular Assembly of Pentacene on Monolayer Graphene for High-Performance Organic Transistors,” *J. Am. Chem. Soc.*, vol. 133, p. 4447, 2011.

[162] R. A. Marcus, “Electron transfer reactions in chemistry. Theory and experiment The use of chemically modified,” *Rev. Mod. Phys.*, vol. 65, no. 3, 1993.

[163] G. R. Hutchison, M. A. Ratner, and T. J. Marks, “Intermolecular charge transfer between heterocyclic oligomers. Effects of heteroatom and molecular packing on hopping transport in organic semiconductors,” *J. Am. Chem. Soc.*, vol. 127, no. 48, p. 16866, 2005.

[164] G. R. Hutchison, M. A. Ratner, and T. J. Marks, “Hopping transport in conductive heterocyclic oligomers: Reorganization energies and substituent effects,” *J. Am. Chem. Soc.*, vol. 127, no. 7, p. 2339, 2005.

[165] G. Nan, X. Yang, L. Wang, Z. Shuai, and Y. Zhao, “Nuclear tunneling effects of charge transport in rubrene, tetracene, and pentacene,” *Phys. Rev. B - Condens. Matter Mater. Phys.*, vol. 79, no. 11, pp. 1–9, 2009.

[166] D. V. Lang, X. Chi, T. Siegrist, A. M. Sergent, and A. P. Ramirez, “Amorphouslike density of gap states in single-crystal pentacene,” *Phys. Rev. Lett.*, vol. 93, no. 8, p. 086802, 2004.

[167] M. Nikolka *et al.*, “High operational and environmental stability of high-mobility conjugated polymer field-effect transistors through the use of molecular additives,” *Nat. Mater.*, vol. 16, no. 3, pp. 356–362, 2017.

[168] R. Porrazzo *et al.*, “Field-effect and capacitive properties of water-gated transistors based on polythiophene derivatives,” *APL Mater.*, vol. 3, no. 1, 2015.

[169] C. D. Lorenz and R. M. Ziff, “Precise determination of the critical percolation threshold for the three-dimensional ‘Swiss cheese’ model using a growth algorithm,” *J. Chem. Phys.*, vol. 114, no. 8, p. 3659, 2001.

[170] Y. Mei *et al.*, “Crossover from band-like to thermally activated charge transport in organic transistors due to strain-induced traps,” *Proc. Natl. Acad. Sci.*, vol. 114, p. E6739, 2017.

[171] W. Schottky, “Zur Halbleitertheorie der Sperrschicht- und Spitzengleichrichter.,” *Z. Phys.*, vol. 113, p. 367, 1938.

[172] N. F. MOTT, “The theory of crystal rectifiers,” *Proc. R. Soc. Lond. A*, vol. 171, p. 27, 1939.

[173] F. Amy, C. Chan, and A. Kahn, “Polarization at the gold/pentacene interface,” *Org. Electron. physics, Mater. Appl.*, vol. 6, no. 2, pp. 85–91, 2005.

[174] M. Oehzelt, N. Koch, and G. Heimel, “the energy level alignment at electrode interfaces,” *Nat. Commun.*, vol. 5, no. May, pp. 1–8, 2014.

[175] G. Paasch and S. Susanne, “Charge carrier density of organics with Gaussian density of states : Analytical approximation for the Gauss – Fermi integral,” *J. Appl. Phys.*, vol. 107, p. 104501, 2010.

[176] C. Liu, Y. Xu, and Y. Y. Noh, “Contact engineering in organic field-effect transistors,” *Mater. Today*, vol. 18, no. 2, pp. 79–96, 2015.

[177] Y. Xu, H. Sun, and Y. Noh, “Schottky Barrier in Organic Transistors,” vol. XX, no. Xx, pp. 1–12, 2017.

[178] Y. Preezant, Y. Roichman, and N. Tessler, “Amorphous organic devices - Degenerate semiconductors,” *J. Phys. Condens. Matter*, vol. 14, no. 42, pp. 9913–9924, 2002.

[179] J. Hwang, A. Wan, and A. Kahn, “Energetics of metal-organic interfaces: New experiments and assessment of the field,” *Mater. Sci. Eng. R Reports*, vol. 64, no. 1–2, pp. 1–31, 2009.

[180] S. D. Baranovskii, O. Rubel, and P. Thomas, “Theoretical description of hopping transport in disordered materials,” *Thin Solid Films*, vol. 487, no. 1–2, pp. 2–7, 2005.

[181] C. H. Kim, Y. Bonnassieux, and G. Horowitz, “Fundamental Benefits of the Staggered Geometry for Organic Field-Effect Transistors,” vol. 32, no. 9, pp. 1302–1304, 2013.

[182] J. P. Yang, F. Bussolotti, S. Kera, and N. Ueno, “Origin and role of gap states in organic semiconductor studied by UPS: As the nature of organic molecular crystals,” *J. Phys. D. Appl. Phys.*, vol. 50, no. 42, 2017.

[183] N. Ueno *et al.*, “Angle-resolved ultraviolet photoelectron spectroscopy of thin films of bis(1,2,5- thiadiazolo)- -quinobis (1,3-dithiole) on the MoS2 surface,” *J. Chem. Phys.*, vol. 107, p. 2079, 1997.

[184] A. Wan, J. Hwang, F. Amy, and A. Kahn, “Impact of electrode contamination on the α-NPD/Au hole injection barrier,” *Org. Electron.*, vol. 6, no. 1, pp. 47–54, 2005.

ECOLE DOCTORALE

Titre : Modélisation numérique des transistors à effet de champ organiques basé sur la densité d'états Gaussienne

Mots clés : Electronique organique, Transistors à effet de champ organiques, Modélisation de physique, Modélisation numérique, Densité d'état gaussienne

Résumé : Bien que la physique des transistors organiques ait été largement étudiée, l'analyse avec la densité d'états Gaussianne fait toujours défaut malgré la nature désordonnée des semi-conducteurs organiques. Étant donné que le transport et l'injection de charges ont lieu à la densité d'états Gaussienne, cette structure énergétique distinctive des semi-conducteurs organiques pourrait rendre le processus d'accumulation de charges, et donc le fonctionnement du dispositif, différent. Cette thèse est consacrée à la compréhension de l'effet de la densité d'états Gaussienne sur les paramètres des transistors organiques, la tension de seuil, la mobilité du porteur de charge et la barrière d'injection via des simulations 2D basées sur des éléments finis numériques et la validation expérimentale. La tension de seuil est comprise par le piégeage de charge dans la secondaire densité d'états Gaussianne ainsi que dans la densité d'états intrinsèque. Nous montrons que le chevauchement des deux densité d'états en raison du désordre induit des comportements de seuil spécifiques des transistors organiques. Deuxièmement, le transport est étudié via le modèle gaussien désordonné sur des sites spatiaux aléatoires de semi-conducteurs organiques. Ce modèle peut offrir un résultat précis par rapport au modèle avec un réseau cubique. De plus, nous proposons une paramétrisation correcte du modèle pour des polymères aux petites molécules. Enfin, la barrière d'injection basée sur la charge et le transport est étudiée et comparée. Les avantages et les limites de chaque modèle sont évalués.

Title : Gaussian density-of-states driven numerical modeling of organic field-effect transistors

Keywords : Organic electronics, Organic field-effect transistors, Device physics, Numerical modeling, Gaussian density-of-states

Abstract : Although the device physics of organic field-effect transistors (OFETs) has been widely studied, the analysis with energetic distribution of the density-of-states (DOS) is still lacking in spite of the disordered nature of organic semiconductors. Because charge transport and injection take place at the Gaussian DOS, this distinctive energetic structure of organic semiconductors could make the charge-accumulation process, and hence the device operation, different. This thesis is dedicated to understanding the effect of Gaussian DOS on device parameters of OFETs, the threshold voltage, charge-carrier mobility and injection barrier via numerical finite-element based 2D simulations and experimental validation. The threshold voltage is comprehended by the charge trapping into the secondary Gaussian trap DOS as well as the intrinsic Gaussian DOS. We show that the overlap of two Gaussian DOSs due to the disorder induces specific threshold behaviors of OFETs. Second, the hopping transport is studied via Gaussian disordered model (GDM) on random spatial sites of organic semiconductors. This model can offer a precise result over GDM with cubic lattice. Also, we propose a correct parametrization of the model for wide range of materials from polymers to small molecules. Lastly, charge-based and transport-based injection barrier are studied and compared with Gaussian DOS. The advantages and limits of each model are evaluated.

Institut Polytechnique de Paris
91120 Palaiseau, France